INSTITUTE OF PAPER SCIENCE AND TECHNOLOGY

INFLUENCE OF RANDOM FORMATION ON PAPER MECHANICS: EXPERIMENTS AND THEORY

By

Jaime Castro

A Dissertation

Submitted to the Faculty of IPST
in partial fulfillment of the requirements for
the degree of Ph.D

Atlanta, Georgia
August 30, 2001

This work is dedicated to my wife, Maria Teresa, and my daughters, Jenny Paola and Daniela Sophia, for their love, patience, and support.

Contents

List of Figures iii

List of Tables vii

Abstract viii

Acknowledgments ix

1 Introduction 1

1.1 Literature Review . . . 1

1.1.1 Local variability of paper properties . . . 1

1.1.2 Constitutive models for paper . . . 2

1.1.3 Micromechanics and fiber network models . . . 2

1.1.4 Continuum models . . . 4

1.1.5 Effect of formation on mechanical properties . . . 5

1.1.6 Explicit FE model and FLAC . . . 9

1.1.7 Size effect and scaling in solid mechanics . . . 12

1.1.8 Effective material response . . . 16

1.2 Conclusions . . . 17

1.3 Objectives . . . 18

2 Plasticity of Huber-Mises Materials with Random Structure 20

2.1 Background . . . 20

2.2 Rigid-plastic microstructures . . . 22

2.3 Mechanics of rigid-plastic microstructures on mesoscales . . . 26

2.3.1 Extension of Hill condition to rigid-plastic materials . . . 26

2.3.2 Bounding on mesoscales via kinematic and traction boundary conditions . . . 27

2.4 Plane deformation rate and plane stress responses of random Huber-Mises material . . . 28

2.4.1 Plane deformation rate . . . 28

2.4.2 Plane stress . . . 33

2.5 Conclusions . . . 40

3 Inelastic and Nonlinear Model for Paper **45**
3.1 Background 45
3.2 Thermomechanics with internal variables T.I.V. 46
3.2.1 Basic concepts 46
3.2.2 Inelastic and nonlinear behavior beyond the elastic range . . . 48
3.2.3 Yield condition and flow rule 49
3.2.4 Viscous (strain rate-dependence) effects 50
3.2.5 Isotropy (handsheets) versus orthotropy (machine-made paper) of response 51
3.2.6 Random formation effects 51

4 Computer Modeling of Paper **54**
4.1 Finite element model 54
4.2 Paper as a linear elastic-plastic isotropic material 57
4.3 Paper as an elastic-plastic orthotropic material 61
4.3.1 Experimental 61
4.3.2 Elastic orthotropic model 69
4.3.3 Nonlinear hyperelastic orthotropic model 71

5 Strain and Temperature Fields in Paper **79**
5.1 Cross-correlation between formation and strain patterns 79
5.2 Temperature fields during dynamic fracture of paper 83

6 Closure **89**
6.1 Conclusions and Significance 89

List of symbols **92**

References **94**

List of Figures

1.1 Constitutive models for paper. 3
1.2 Finite element model with properties' variation through thickness of elements. 7
1.3 The deformation modes a, b, and c of the model cells considered by Korteoja et al. (1996). 8
1.4 Deformation of an element cell subjected to biaxial loading 8
1.5 Idealized material laws used by Korteoja et al. (1998). (a) Random elastic modulus with constant yield strain and breaking strain. (b) Constant modulus with random yield strain and breaking strain. . . . 9
1.6 Motion and equilibrium. Application of a time-varying force to a mass, resulting in acceleration (FLAC, 1998). 10
1.7 Explicit calculation cycle of FLAC (adapted from FLAC, 1998). . . . 11
1.8 Numbering scheme for elements and gridpoints in FLAC. 13
1.9 (a) Overlaid quadrilateral elements used in FLAC. (b) Typical triangular element with velocity vectors. (c) Nodal force vector (from FLAC, 1998). 13
1.10 Comparison of explicit and implicit solution methods (From FLAC, 1988). 14
1.11 Distribution of weak spots in measuring areas of different sizes. 15
1.12 Finite element model with individual assignment of nonlinear constitutive law to each cell. 18

2.1 Yield surface of soft (inner ellipse) and hard phases (outer ellipse) in plane stress. Where is the resulting yield surface of a two-phase composite? 23
2.2 The yield surface of a Huber-Mises material in plane stress ($\sigma_{33} = 0$) is an ellipse. The deformation rate vectors $\mathbf{d}$ are normal to this yield surface for an associated flow rule. 24
2.3 Huber-Mises yield surface is a cylinder in stress space. 25
2.4 Two realizations of a random, two-phase chessboard material, of nominal volume fractions 50%, in finite-size windows (a) 10×10 and (b) 50×50. (c) The corresponding apparent rigid-plastic responses at contrast 5 under uniform kinematic and uniform traction boundary conditions. 29

2.5 Yield locus for plane deformation rate (plane strain). The yield surface is described by: $\sigma_2 = \sigma_1 \pm \sqrt{\frac{2}{3}}\sigma_{yield}$. 30
2.6 Apparent plastic responses (shown in terms of the von Mises strain) of the two-phase 10×10 chessboard in plane deformation rate (called 'plane strain' for short) under kinematic and traction boundary conditions. 32
2.7 Apparent plastic responses (shown in terms of the von Mises strain) of the two-phase 50 × 50 chessboard in plane deformation rate (called 'plane strain' for short) under kinematic and traction boundary conditions. 34
2.8 An ensemble view of apparent yield surfaces of random Huber-Mises two-phase chessboards in plane deformation rate on mesoscales $\delta = 10$ and 50. Hard and soft phase yield loci are shown, too. 35
2.9 Huber-Mises yield locus for planes stress. Yield surface is described by: $\sigma_1^2 - \sigma_1\sigma_2 + \sigma_2^2 = \sigma_{yield}^2$ ($\sigma_{yield} = 1$ in this example). 36
2.10 Apparent plastic responses (von Mises strain) of the two-phase 10×10 chessboard in plane stress under kinematic and traction boundary conditions. 37
2.11 Apparent plastic responses (von Mises strain) of the two-phase 50 × 50 chessboard in plane stress under kinematic and traction boundary conditions. 38
2.12 An ensemble view of apparent yield surfaces under kinematic conditions in plane stress on mesoscales $\delta = 10$ and 50. Hard and soft phase yield loci, as well as an average kinematic-controlled locus and two most extreme ones on $\delta = 50$, are also shown. 39
2.13 A close-up from Fig. 2.11 of the ensemble view of apparent yield surfaces in plane stress, focusing on the first quarter in the space of principal stresses, on mesoscales $\delta = 10$ and 50. The vectors, shown for ensemble average yield surfaces at $\delta = 10$ and 50 under kinematic and traction conditions, display the departure from normality. 41
2.14 The departure from normality displayed in the previous figure is now shown in terms of the difference $\pi/2 - \alpha_{\overline{\mathbf{d}}}$, where $\alpha_{\overline{\mathbf{d}}}$ is the actual angle the $\overline{\mathbf{d}}$ vector makes to the yield surface. 42
2.15 A realization on mesoscale $\delta = 10$ can be resolved using a grid of 50×50 (bottom) instead of 10 × 10 (top) elements. 44

3.1 Spring and dashpot to illustrate the concept of internal variables. . . 47
3.2 (a) Stress-strain curve of the elastic-plastic model.; (b) energies involved in the inelastic response of paper; (c) a rheological model of elastic plastic response; (d) a rheological model of visco-elastic plastic response. 49
3.3 Surface of body B, which is made up of the part controlled by displacements, ∂B_δ^u, and another one controlled by tractions, ∂B_δ^t 52

4.1 Assigning material properties and constitutive law to each element. . 55

4.2 Selecting the scale for the simulation model. 55
4.3 Generation of the Boolean model of paper formation. 56
4.4 Paperboard's basis weight mapping from β-radiography (provided by Miranda Bliss of IPST). 56
4.5 Illustration of mesoscale window 58
4.6 Stepwise-elastic-plastic isotropic model in plane stress. 59
4.7 Material's response under pure shear loading. Mesoscale $\delta = 10$. . . . 59
4.8 Comparison of responses according to boundary conditions and mesoscale. 60
4.9 Comparison of effective responses according to mesoscale and applied boundary conditions 62
4.10 Shear stress-strain curves of effective response 62
4.11 Biaxial testing setup with a squared paper specimen clamped at its edges. 63
4.12 Stress-strain curves. Uniaxial loading in MD and CD. 64
4.13 Example of applied boundary conditions for cases (1, 0), (0,1), (1,-1) and (1,1). 65
4.14 Biaxial stress-strain diagrams for kraft paper corresponding to three loading regimes I, II, III (machine direction parallel to y) from Uesaka, Murakami, and Imamura (1979). 65
4.15 Stress-strain curves - Case (1.0, 0.0). 66
4.16 Stress-strain curves - Case (0.0, 1.0). 66
4.17 CD vs. MD-stress response of several loading cases. Solid lines are experimental curves and dashed lines are the curves predicted by linear-elastic orthotropy up to the yield point. 67
4.18 Yield and failure surfaces of paper. 68
4.19 Stress-strain curve fitting - Loading cases (1.0, 1.0) and (0.0, 1.0). . . 73
4.20 Stress-strain curve of loading case (1.0, 0.2). Solid lines are experimental curves and dashed lines are predicted curves. 74
4.21 Stress-strain curve of loading case (1.0, 0.6). Solid lines are experimental curves and dashed lines are predicted curves. 75
4.22 Stress-strain curve of loading case (1.0, 1.0). Solid lines are experimental curves and dashed lines are predicted curves. 75
4.23 Stress-strain curve of loading case (0.6, 1.0). Solid lines are experimental curves and dashed lines are predicted curves. 76
4.24 Stress-strain curve of loading case (0.2, 1.0). Solid lines are experimental curves and dashed lines are predicted curves. 76
4.25 CD vs. MD-stress response of several loading cases. Solid lines are experimental curves and dashed lines are predicted curves. 77
4.26 Stress-strain curve for case (0.0, 1.0) after biaxial cyclic loading and unloading. 77

5.1 Simulated areal dilatation against local grammage of paperboard. Theorethical regression sugested by Dodson (1970) as a dashed line. . . 80
5.2 Formation of a paper sample of 70 × 80 mm from reflective scanning (left) and from β-ray radiography (right). 81

5.3 Mapping formation of a low basis weight white paper with a scanner. 81
5.4 Scanned image of paper. The central portion is a square of 48 × 48 mm that was subjected to strain up to fracture. 82
5.5 Effective von Mises strain in a homogeneous (top) and a nonhomogeneous (bottom) material. In the greyscale, clearest zones correspond to 0.8% and darkest zones to 2.2% strain. Applied strain is 1.05% in x (MD). 84
5.6 Cross-correlation between formation and strain patterns (48 × 48 mm). On the right image, clearest zones correspond to 0.8% and darkest zones to 2.2% von Mises strain. 85
5.7 Simulated effective strain change against grammage 85
5.8 Cross-correlation between negative image of formation (left) and strain patterns (right). Sample size is 160 × 160 mm. On the right image, clearest zones correspond to 0.8% and darkest zones to 2.2% von Mises strain. 86
5.9 Simulated fracture of uniaxial strain tests in MD and CD. Failure criteria is based on von Mises strain. 86
5.10 Infrared picture of dynamic fracture of paper. Sample is 25 mm wide. 87
5.11 Infrared picture of dynamic crack propagation in paper. Sample is 25 mm wide. 88

6.1 Obtaining mechanical properties from a fiber network model. 91

List of Tables

4.1 Loading cases under uniform displacement b.c. 64
4.2 Tensile, compressive, and shear strength values. 68
4.3 Mechanical properties from ultrasound measurements. 70

5.1 Experimentally measured material constants. 82

ABSTRACT

The effect of formation on mechanical properties of paper has been studied through computer simulation and measurement of local properties, but a better understanding of the paper micromechanics is still needed to develop more realistic simulation models. A computer model based on a Finite Difference Element Method is being used here to enhance this understanding. With this method, which is an explicit scheme, it is possible to analyze the effect of the local properties' variability on the overall properties of paper without the need of extraordinary computer resources.

In the present computer model, a paper sheet is represented by rectangular elements in a grid. The element's response may follow a prescribed linear or nonlinear stress-strain constitutive law. Furthermore, each element can be assigned with a different constitutive law through variation of material parameters. In other words, it is possible to model the nonhomogeneous character of paper.

Uniaxial and biaxial strain or traction tests on nonhomogeneous material samples are simulated by applying uniform boundary conditions. This allows obtaining the stress fields, which can be compared to evaluate the influence of local property variability.

A scale dependent hierarchy of bounds on the apparent macroscopic response of materials with random microstructure, such as an ideal random chessboard composite and paper, is found. A constitutive model equation of paper for biaxial tensile loading is developed and used to simulate the effective von Mises strain field of a paper sample under uniaxial loading. This strain field is then correlated with a formation image. The resulting effective strain field seems to be a mix of the formation image with shear bands. This type of theoretical work is applicable to optimize fiber use with respect to the desired mechanical properties, i.e., it can be used to determine up to what point it is advantageous to enhance paper's formation and increase nominal basis weight.

ACKNOWLEDGMENTS

I wish to thank the members companies of the Institute of Paper Science and Technology for their support to the academic program. I am grateful to my Advisory Committee members, Dr. Iwona Jasiuk, Mr. John Waterhouse, and Dr. Martin Ostoja-Starzewski, for their guidance. I am personally very thankful to Dr. Ostoja-Starzewski for his invaluable advice and many suggestions and ideas.

I acknowledge Dr. Douglas Coffin and Ph. D. Candidate Dana Ingalsbe for offering the new biaxial tester, as well as Ted Jackson for setting it up for my experimental work. Also, I would like to thank Miranda Bliss and Kennisha Collins for their help with paper testing.

Chapter 1

Introduction

1.1 Literature Review

The multiscale structure of cellulose fiber network, particularly the degree of its bonding and density, has a significant effect on paper's mechanical properties below and beyond the plastic limit, as well as for crack propagation. These aspects have been studied through some computer simulations and measurement of local properties, but a better, more systematic, understanding of the paper micromechanics from the standpoint of mechanics of random media is still needed to develop adequate constitutive laws and more realistic simulation models.

1.1.1 Local variability of paper properties

The fibrous nature of paper implies the existence of local variability of its properties at the microscopic level. This variability has its origins mainly in the following factors:

- Nonuniformity of basis weight (formation)
- Spatial variation of fiber orientation
- Spatial variation of bonding degree
- Spatial variation of drying shrinkage
- Furnish or fiber properties

  It is important to note that spatial variability is unavailable in a random fiber network of paper, lacking any periodicity (e. g., Castro and Ostoja-Starzewski, 2000).

Variations in local grammage, fiber orientation, drying strains, and bonding degree, among other factors, might cause local variability of measured elastic constants besides the normal experimental variability (Kärenlampi et al. (1996), Ferahi et al. (1996), and Niskanen (1998)). Local variability affects the strain distribution and

concomitantly the local rupture process through a paper specimen. The repeatability and reproducibility of the standardized fracture toughness test of Wellmar, Fellers, and Delhage (1997a), for example, are of the same order of magnitude as for tensile energy absorption (TEA) and higher than for tensile strength as they are compared in Wellmar et al. (1997b). On the other hand, DiMillo and Ostoja-Starzewski (1998) examined the degree of variability in four parameters of the stress-strain response of 34 g/m^2 paper. In particular, TEA coefficient of variation was typically 14%. This value resulted from dividing a complete paper web into 7 $\times$ 1 inch specimens (in an array of 8 $\times$ 25) and testing each specimen. Korteoja et al. (1998) measured, among several mechanical properties, TEA coefficient of variations around 15% in copy paper (MD) and 23% in newsprint (CD). Therefore, these works point to the importance of considering the effect of mechanical properties variability on the global mechanical behavior of paper. Perhaps the most studied source of paper's mechanical property variability has been formation (see Norman (1966), Norman and Wahren (1976), Göttsching (1979), Korteoja et al. (1995, 1996, 1997, 1998), and Wong et al. (1996)).

1.1.2 Constitutive models for paper

Ramasubramanian and Wang (1999) classified the constitutive models for paper as either network or continuum models. Network models can be further divided into other subcategories, such as semiempirical models and micromechanics models. On the other hand, continuum models can be further divided into hydrogen bond, hyperelasticity, mosaic, and composite laminate models. Figure 1.1 shows schematically all these subcategories of the network and continuum models.

Regarding continuum models, Suhling (1990) previously presented a limited review of existing methods for modeling the mechanical response of paper and paper composites used in applications where they are subjected to multiaxial stress states and changing environmental conditions. After this review, he emphasizes the need to incorporate nonlinear viscoelastic or inelastic constitutive relations into paper modeling. Baum (1993) also reviewed the main aspects of paper modeling, including micromechanics, laminate, and continuum models. Jayaraman and Kortschot (1998) reviewed and compared most fiber-network models related to the tensile strength of paper.

1.1.3 Micromechanics and fiber network models

The structure of the fiber network has a great effect on the threshold of spontaneous crack propagation (Niskanen, 1993), particularly the degree of bonding and density. The understanding of what happens at the crack tip at the microscopic level can help explain the difficulties of characterizing fracture toughness. Some authors have considered this aspect in different manners. The same observation techniques from fracture mechanics have been adapted to observe crack propagation in paper. A complementary approach is to simulate the cracking process with computer models.

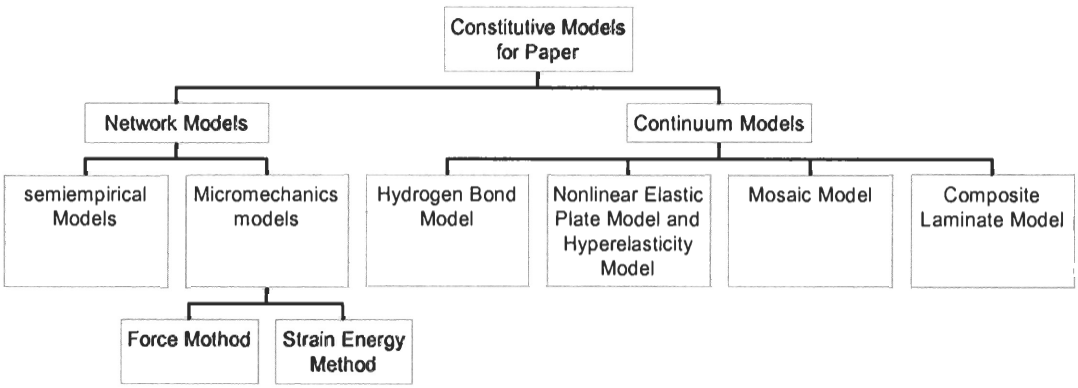


Figure 1.1: Constitutive models for paper.

In these models, the objective is to find the connection between paper fiber-network on the microscopic level and the respective global mechanical performance.

Network modeling has become a matter of computer simulation as computer capacity has increased. The finite element method is frequently used to evaluate the properties of the random fiber network. Some conditions and assumptions that can be made to simulate paper microstructure have been reviewed by Perkins et al. (1990) and Niskanen (1993) in several publications. However, the first use of fiber network models to understand paper mechanical behavior was presented by Cox (1952). He considered a network of infinitely long fibers capable of carrying axial forces only and having the (spatially homogeneous) geometry of a planar Poisson line field; effective moduli were then derived under conditions of uniform strain. The Cox model has been subjected to many refinements to obtain a more realistic modeling of the paper-fiber network, e.g., Gates and Westcott (1996). The most sophisticated models use numerical simulations and have been extended to study paper fracture mechanics, as well as elasticity (Aström and Niskanen, 1991). It must be noted, however, that the Cox model lacks generic rigidity which is required of any solid material. This pathological behavior can be removed by the introduction of (i) rigid fiber-fiber bonds (justified, in fact, by the presence of hydrogen bonding between cellulose fibers) and (ii) fiber flexural stiffness (Ostoja-Starzewski et al., 1999).

Micromechanics modeling requires many assumptions regarding the fiber structure, fiber-to-fiber bond, and network structure. The models are normally constituted by linear elastic beams of statistical distribution in length, constitutive properties, and orientation. Most models use straight beams, but curl or arched shapes have also been used as in Heyden and Gustafsson (1998). A failure criterion for the beam elements or the interfiber bonds is required in each model. Aström and Niskanen (1991) and Räisänen et al. (1997) included the effect of stress localization in the fracture of a two-dimensional random-fiber network. The fiber network models are usually limited by the number of fibers that can be simulated within practical computer-resources limitations, typically 1,000 fibers.

Feldman et al. (1996) proposed a different approach to paper fracture modeling

by using a Monte Carlo simulation. They designed a computer program to generate up to 10,000 fibers across the fracture line. The problem with this simulation is that the rupture line is predetermined. Wentao and Carlsson (1996) also used the Monte Carlo method to simulate the formation and microstructure of paper and to statistically analyze its structure in relation to its density.

Heyden and Gustafsson (1998) presented a simulation fracture model of a paper fiber network with most of the characteristics of previous models. Fibers are arranged in a random structure according to an arbitrary network density and orientation distribution. Fibers can be assigned arbitrary distribution in length, curl, cross section geometry and moment of inertia, material stiffness, and strength parameters. The novel feature in this model is the assumption concerning the fiber-to-fiber bonding. The compliance and softening of each of these bondings was modeled by a connection element composed of springs which are assigned nonlinear properties, representing stick slip performance.

1.1.4 Continuum models

The most basic constitutive relation to model machine-made paper is the elastic orthotropic model. In a state of plane stress, this material law is expressed as:

$$\begin{bmatrix} \sigma_{11} \\ \sigma_{22} \\ \tau_{12} \end{bmatrix} = \begin{bmatrix} \frac{E_1}{(1-\nu_{12}\nu_{21})} & \frac{E_2\nu_{12}}{(1-\nu_{12}\nu_{21})} & 0 \\ \frac{E_1\nu_{21}}{(1-\nu_{12}\nu_{21})} & \frac{E_2}{(1-\nu_{12}\nu_{21})} & 0 \\ 0 & 0 & 2G \end{bmatrix} \begin{bmatrix} \varepsilon_{11} \\ \varepsilon_{22} \\ \gamma_{12} \end{bmatrix} \tag{1.1}$$

The engineering constants for an orthotropic material in (1.1) are:

E_1 = Young's modulus in 1-direction (MD).

E_2 = Young's modulus in 2-direction (CD).

$\nu_{12} = \frac{-\varepsilon_{22}}{\varepsilon_{11}}$ is the Poisson's ratio for strain in 2-direction (CD) when paper is stressed in the 1-direction (MD) only.

$\nu_{21} = \frac{-\varepsilon_{11}}{\varepsilon_{22}}$ is the Poisson's ratio for strain in 1-direction (MD) when paper is stressed in the 2-direction (CD) only.

G = shear modulus in 1-2-plane.

There are several experimental forms to determine the values of these constants (see Bronkhorst and Bennett, 2001). Also, Baum et al. (1983) presented a method to estimate the value of specific elastic modulus from ultrasonic measurements.

The nonlinear elastic plate and hyperelasticity models are of particular interest in this research. Johnson and Urbanik (1984) treated paper as a homogeneous material. They formulated a nonlinear elastic plate model using basic equations of nonlinear elasticity and arrived at a set of constitutive relations which links the plate behavior to its strain energy density $w(e)$. It is given by:

$$\sigma_{ij} = \frac{\partial w(e)}{\partial \varepsilon_{ij}}, \tag{1.2}$$

where w is a function of the effective strain e defined as:

$$e = \frac{\varepsilon_1^2}{v_{21}} + \frac{\varepsilon_2^2}{v_{12}} + 2\varepsilon_1\varepsilon_2 + (1 - \nu_{12}\nu_{21})\frac{G}{v_{12}E_1}\gamma_{12}. \tag{1.3}$$

However, the functional form of $w(e)$ was not known for paper. Therefore, it had to be found empirically by fitting an assumed function. Suhling et al. (1989) used an empirical approach to determine this strain energy density function. The MD and CD uniaxial stress-strain curves of paperboard were modeled by the expressions:

$$\sigma_{11}(\varepsilon_1) = C_1^{MD}\tanh(C_2^{MD}\varepsilon_{11}) + C_3^{MD}\varepsilon_{11} = \frac{dw(\varepsilon_{11})}{d\varepsilon_{11}}, \tag{1.4}$$

$$\sigma_{22}(\varepsilon_2) = C_1^{CD}\tanh(C_2^{CD}\varepsilon_{22}) + C_3^{CD}\varepsilon_{22} = \frac{dw(\varepsilon_{22})}{d\varepsilon_{22}}. \tag{1.5}$$

These equations could be integrated directly to obtain $w(\varepsilon_{11})$ or $w(\varepsilon_{22})$. Then, by substituting $\varepsilon_{11}(e)$ or $\varepsilon_{12}(e)$, they obtained two expressions for $w(e)$ that, in turn, could be substituted in the following stress-strain relation for a hyperelastic material subjected to plane stress:

$$\begin{bmatrix} \sigma_{11} \\ \sigma_{22} \\ \tau_{12} \end{bmatrix} = 2\frac{dw(e)}{de}\begin{bmatrix} \frac{1}{\nu_{21}} & 1 & 0 \\ 1 & \frac{1}{\nu_{12}} & 0 \\ 0 & 0 & (1 - \nu_{12}\nu_{21})\frac{G}{v_{12}E_1} \end{bmatrix}\begin{bmatrix} \varepsilon_{11} \\ \varepsilon_{22} \\ \gamma_{12} \end{bmatrix}. \tag{1.6}$$

However, the derivatives of each $w(e)$, obtained from CD or MD, led them to inconsonant results, so these functions could not be used to predict their experimental data in any direction. Their alternative was to fit a compromising curve between both strain energy density functions. This hyperelastic model cannot be used for the present computer simulation model because it does not describe the mechanical behavior of paper in MD and CD as well as in a biaxial test.

1.1.5 Effect of formation on mechanical properties

The methods to simulate paper's mechanical properties traditionally assume that paper is a homogeneous material and presume the existence of a uniform constitutive equation for such a material. However, variations in local grammage, fiber orientation, drying strains, and bonding degree among other factors might cause local variability of elastic constants (see Norman (1966), Norman and Wahren (1976), Göttsching (1979), and Niskanen, (1998)). This variability affects the strain distribution and concomitantly the local rupture process through a paper specimen. The coefficient of variation of local grammage is the common way to measure formation. However, it does not represent the spatial (e. g., correlation structure) variability of the paper fiber network. Therefore, experimental measurements of the macroscopic mechanical properties of paper sheets of different formation indexes, for example, give very

limited information of the microscopic or local properties. To study the effect of the elastic-constants' spatial variation on the mechanical properties of paper, computer simulations have been used. The problem in this case is the assignment of values to small-scale local regions employed as finite elements in the computer simulation.

Wong et al. (1995, 1996) viewed paper as a homogeneous membrane with varying local thickness. They divided the specimen model in square plates of 1 mm^2 and assigned each one a thickness proportional to the grammage of a real paper specimen at the equivalent position with respect to the model. They used handsheets made of kraft pulp. Local grammage distributions were obtained by β-radiography. The mechanical behavior of each square element was modeled with a single nonlinear stress-strain curve coming from an actual uniaxial specimen test. Figure 1.2 illustrates this approach. Each element has a thickness proportional to its grammage, but has the same constitutive law. The finite element method was used to model the evolution of stress and strain distributions in fracture mode I. The simulation model was loaded incrementally up to the actual breaking stress of the corresponding paper specimen. At the same time, a video image correlation technique was used to measure the strain field in a real specimen. The resolution of the strain field measured in handsheets was 1 mm. According to the authors, the comparison of the outcomes from these two exercises resulted in a reasonable correlation: "*The experimental and finite element results confirm that local grammage and local tensile strain are inversely proportional.*" Fracture was found to initiate from regions of low grammage and propagate along a path perpendicular to the load, regardless of local grammage variation. The authors pointed out that a better correlation could probably be found if other factors, such as local orientation distribution, were considered. Independently of this issue, a major problem of the model is the assumption that all the squared elements have the same constitutive behavior.

The existing computer simulation models are able to represent the mechanical and fracture behavior of very small pieces of low-density papers with a certain degree of realism. However, no matter how sophisticated the model, there is still a need to gather experimental information at the microscopic level to compare the prediction of simulations with real paper specimen characteristics.

Besides the study by Wong and coworkers just reviewed, there are only two additional studies with this approach. Using a linear image strain analysis (LISA) technique, Choi and Thorpe (1991) experimentally detected changes in strain distribution around a crack with progressive loading (mode I) for the first time in paper. They found that the size of the zone of influence relative to the size of the crack was larger than expected. Their analysis indicated that irreversible deformation was taking place at the crack tip. This also indicated that the linear elastic fracture mechanics (LEFM) assumptions were not clearly satisfied. From this work, it is clear that the strain field varies locally in paper.

Korteoja et al. (1998) conducted a study to compare local damage and strain to one another and to grammage. They used a silicone impregnation technique to detect local strain and damage simultaneously in paper (in mode I). The optical transmittance of impregnated specimens correlated very well with the local grammage, which was obtained from β-radiographs. The analysis showed that high grammage points,

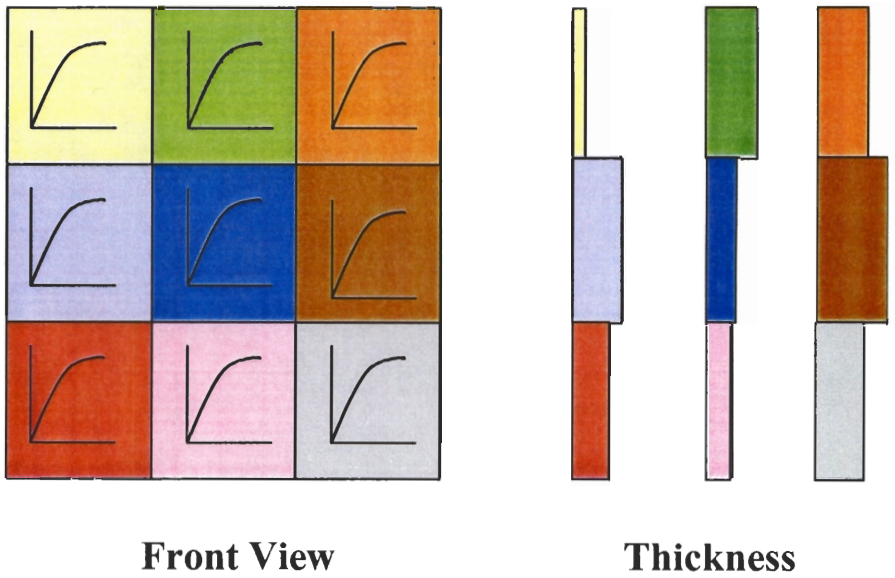


Figure 1.2: Finite element model with properties' variation through thickness of elements.

for example, had always-smaller strain and damage values than low grammage points. In a specimen with good formation, damage diffusely spread throughout the specimen. In a sample with poor formation, damage concentrated in a narrow band in the center of the specimen. The authors recognized that silicone impregnation causes a small increase in the tensile strength and breaking strain. However, this was not a concern because they were not trying to measure the exact values of the mechanical properties.

In a previous work (Korteoja et al., 1996), these authors used the same silicone impregnation technique to show that the plastic deformations or strains are nonuniform on the microscopic (fiber network) and macroscopic (flocs) scale. In addition, computer simulations were used to evaluate the macroscopic strain variations and the changes in paper properties that are induced by formation-type disorder. They concluded that increasing disorder reduces the number of plastic yield sites. In the computer simulations, a specimen was divided into imaginary cells that form a square lattice. The choice of the cell size was arbitrary. Each cell was given an elastic modulus, which represented the combined effects of randomness in local basis weight, fiber orientation, drying strains, and bonding degree. The elastic modulus was the only source of nonuniformity in the model. The modulus values were taken proportional to measured local basis weight of real paper specimens (optionally, they could be randomly assigned).

There are many ways in which the elementary cells can be put together to simulate a disordered continuum material. The method applied by the authors just cited (Korteoja et al., 1996) to model the elongation of the cells is very illustrative and is summarized as follows: The cell corners (nodes of the square lattice) are allowed

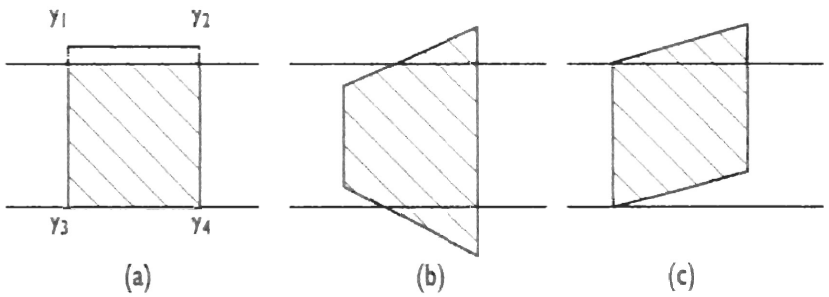


Figure 1.3: The deformation modes a, b, and c of the model cells considered by Korteoja et al. (1996).

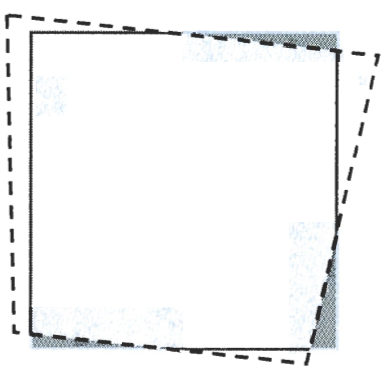


Figure 1.4: Deformation of an element cell subjected to biaxial loading

to move only parallel to the direction of external strain. The uniaxial translation of cell corners leads to three basic deformations (see Figure 1.3 a, b, and c); all other deformations are linear combinations of these three. The deformation of each cell, in response to a given external elongation, is determined by minimizing the total elastic energy of the system. If a deformation component exceeds a set limit, then the cell either fails or becomes plastic, depending on the choice of parameters.

The method to model the deformation mode just described (Korteoja et al., 1996, 1998) assumes cell elongation in the same direction of the applied load. It is not clear that paper necessarily behaves in that fashion. A more realistic strain behavior should consider deformation in two directions, as shown in Figure 1.4. This point is recognized by the authors: "The one-dimensional model fails to explain the experimental observations. A two-dimensional model would be a more appropriate way to simulate paper behavior, as spatial correlations of local grammage (i.e., flocculation) can be included." With this in mind, Korteoja et al. (1998) considered a two-dimensional model sheet. It consisted of a squared array of adjoined cells, each one following the elastic-perfectly-plastic material law shown in Figure 1.5. They used an isotropic

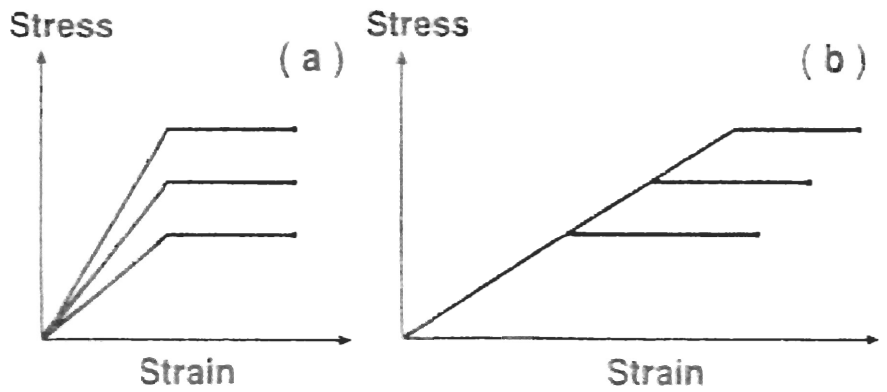


Figure 1.5: Idealized material laws used by Korteoja et al. (1998). (a) Random elastic modulus with constant yield strain and breaking strain. (b) Constant modulus with random yield strain and breaking strain.

model system of 30×30 cell elements corresponding to a 5×5-mm area of real paper.

1.1.6 Explicit FE model and FLAC

A computer simulation model based on a Finite Difference Element Method will be used in this project. This method has already been extensively used in geomechanics (see Cundall (1976)) and goes under the acronym FLAC (Fast Lagrangian Analysis of Continua). The major advantage of this explicit method over the conventional implicit finite element method is that the inversion of a large global stiffness matrix is not needed. Another benefit of the FLAC is that it can model quasistatic or dynamic phenomena. Also, FLAC, just like other finite element methods, allows spatially nonuniform assignment of constitutive properties. Summarizing, the effect of the local properties' variability on the overall properties of paper can be analyzed.

In the present thesis, a paper sheet is represented in FLAC (1998) by rectangular elements within a grid, which is adjusted to fit the shape of the sample to be modeled. The element's response may follow a prescribed linear or nonlinear stress-strain constitutive law. Furthermore, each element can be assigned a different constitutive law via material parameters (Young's modulus, Poisson ratio, etc.). In other words, it is possible to model the nonhomogeneous character of paper. Uniaxial or biaxial strain tests on homogeneous and nonhomogeneous material samples are simulated by applying a constant displacement. This allows obtaining of the stress fields, which can be compared to evaluate the influence of local property variability.

Some details of the Finite Difference Element Method and its theoretical background are reviewed now. In its simplest form (one-degree-of-freedom system), the equation of motion relates the acceleration du/dt, of a mass m, to the applied force F, which may vary with time. Figure 1.6 illustrates a force acting on a mass, causing motion described in terms of acceleration $\ddot{u}$, velocity $\dot{u}$, and displacement u.

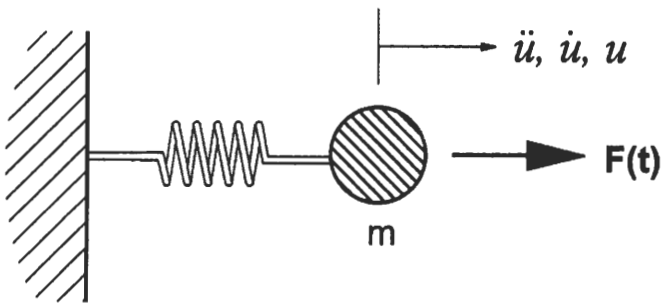


Figure 1.6: Motion and equilibrium. Application of a time-varying force to a mass, resulting in acceleration (FLAC, 1998).

Newton's second law for the mass-spring system is:

$$m\frac{d\,\dot{u}}{dt} = F \tag{1.7}$$

For a continuous solid body, this is generalized as follows:

$$\rho\frac{\partial\,\dot{u}_i}{\partial t} = \frac{\partial\sigma_{ij}}{\partial x_j} + \rho g_i \tag{1.8}$$

where ρ is the mass density, t is the time, x_j are the components of coordinate vector, g_i are the components of gravitational acceleration (body forces), and σ_{ij} are the components of stress tensor.

The other set of equations that apply to a solid, deformable body is known as the constitutive relation, or stress/strain law. First, strain rate is derived from velocity gradient as follows:

$$\dot{e}_{ij} = \frac{1}{2}\left[\frac{\partial\,\dot{u}_i}{\partial x_j} + \frac{\partial\,\dot{u}_j}{\partial x_i}\right] \tag{1.9}$$

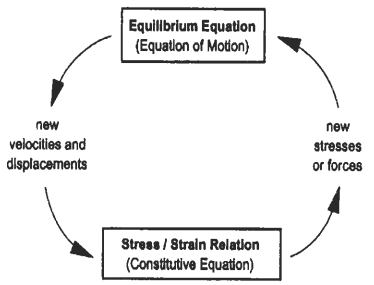
where $\dot{e}_{ij}$ are the strain-rate components and $\dot{u}_i$are the velocity components.

Mechanical constitutive laws are of the form:

$$\sigma_{ij} := f(\sigma_{ij}, e_{ij}, \kappa) \tag{1.10}$$

where f is the functional form of the constitutive law and κ is a history parameter which may or may not be present, depending on the particular law. In general, nonlinear constitutive laws are written in incremental form because there is no unique relation between stress and strain. This equation provides a new estimate for the stress tensor given the old stress tensor and the strain rate (or strain increment). The simplest example of a constitutive law is that of isotropic elasticity:

$$\frac{\partial \dot{u}_i}{\partial x_j} \cong \frac{1}{2A}\left(\dot{u}_i^{(a)} + \dot{u}_i^{(b)}\right) n_j \Delta s \qquad \rho \frac{\partial \dot{u}_i}{\partial t} = \frac{\partial \sigma_{ij}}{\partial x_j} + \rho g_i$$



$$\dot{e}_{ij} = \frac{1}{2}\left[\frac{\partial \dot{u}_i}{\partial x_j} + \frac{\partial \dot{u}_j}{\partial x_i}\right] \qquad \sigma_{ij} = f(\dot{e}_{ij})$$

Figure 1.7: Explicit calculation cycle of FLAC (adapted from FLAC, 1998).

$$\begin{bmatrix} \sigma_{11} \\ \sigma_{22} \\ \tau_{12} \end{bmatrix} = \begin{bmatrix} \frac{E}{(1-\nu^2)} & \frac{\nu E}{(1-\nu^2)} & 0 \\ \frac{\nu E}{(1-\nu^2)} & \frac{E}{(1-\nu^2)} & 0 \\ 0 & 0 & 2G \end{bmatrix} \begin{bmatrix} \varepsilon_{11} \\ \varepsilon_{22} \\ \varepsilon_{12} \end{bmatrix} \tag{1.11}$$

where E is the modulus of elasticity or Young's modulus, G is the shear modulus, and ν is the Poisson's ratio. Another engineering constant, used in the computer program (FLAC) frequently, is the bulk modulus K, defined as:

$$K = \frac{E}{3(1-2\nu)} \tag{1.12}$$

The general calculation sequence embodied in FLAC is illustrated in Figure 1.7. This procedure first invokes the equations of motion to derive new velocities and displacements from stresses and forces. Then, strain rates are derived from velocities, and new stresses from strain rates. One timestep is taken for every cycle around the loop. Each box in Figure 1.7 updates all of its grid variables from known values that remain fixed while control is within the box. For example, the lower box takes the set of velocities already calculated and, for each element, computes new stresses. The velocities are assumed to be frozen for the operation of the box; i.e., the newly calculated stresses do not affect the velocities. Since one loop of the cycle occupies one timestep, the assumption of "frozen velocities" used in FLAC is justified. This means that neighboring elements cannot affect one another during the period of calculation. Of course, after several cycles of the loop, disturbances can propagate across several elements, just as they would propagate physically.

The central concept in FLAC is that the computational wave speed always keeps ahead of the physical wave speed, so that the equations always operate on known values that are fixed for the duration of the calculation. There are several distinct advantages to this approach, but, most importantly, no iteration process is necessary when computing stresses from strains in an element, even if the constitutive law is wildly nonlinear. In an implicit method (which is commonly used in finite element programs), every element communicates with every other element during one solution step (see Figure 1.8): several cycles of iteration are necessary before compatibility and equilibrium are obtained. In FLAC, the solid body is divided by the user into a finite element mesh composed of quadrilateral elements. FLAC subdivides each element into two overlaid sets of constant-strain triangular elements as shown in Figure 1.9.

The four triangular subelements are termed a, b, c, and d. The deviatoric stress components of each triangle are maintained independently, requiring sixteen stress components to be stored for each quadrilateral (4 xx; yy; zz; xy). The force vector exerted on each node is taken to be the mean of the two force vectors exerted by the two overlaid quadrilaterals. In this way, the response of the composite element is symmetric, for symmetric loading. If one pair of triangles becomes badly distorted (e.g., if the area of one triangle becomes much smaller than the area of its companion), then the corresponding quadrilateral is not used; only nodal forces from the other (more reasonably shaped) quadrilateral are used. If both overlayed sets of triangles are badly distorted, FLAC complains with an error message.

The disadvantage of the explicit method is seen to be the small timestep, which means that large numbers of steps must be taken to arrive at a desired point in time, and that the numerical error tends to accumulate with the number of steps growing. Overall, explicit methods are best for ill-behaved systems, e.g., nonlinear, large-strain, physical instability; they are not efficient for modeling linear, small-strain problems. A more detailed comparison can be found in Figure 1.10.

1.1.7 Size effect and scaling in solid mechanics

The size effect is understood as the dependence of the structure's mechanical properties, typically strength, on the structure size. There are three basic theories of scaling in strength/fracture of mechanics of solids (Bažant and Planas, 1998):

1. Weibull's statistical theory of random strength.

2. Theory of stress redistribution and fracture energy release caused by large cracks or Bazant's size effect law.

3. Theory of crack fractality, which is divided into *invasive* and *lacunar* fractality.

The size effect in Weibull's theory comes from the fact that, in a larger structure, the probability of encountering a small material element of a certain small strength increases with the structure size. The theory is based on the model of a chain. The failure load of a chain is determined by the minimum value of the strength of the links in the chain, and the statistical size effect is due to fact that the longer the chain, the smaller is the strength value that is likely to be found in the chain. This probability is expressed as:

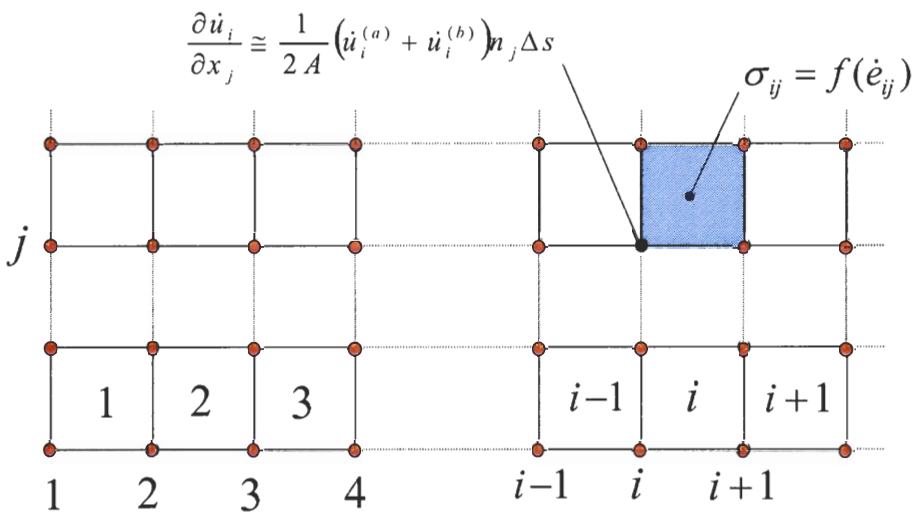


Figure 1.8: Numbering scheme for elements and gridpoints in FLAC.

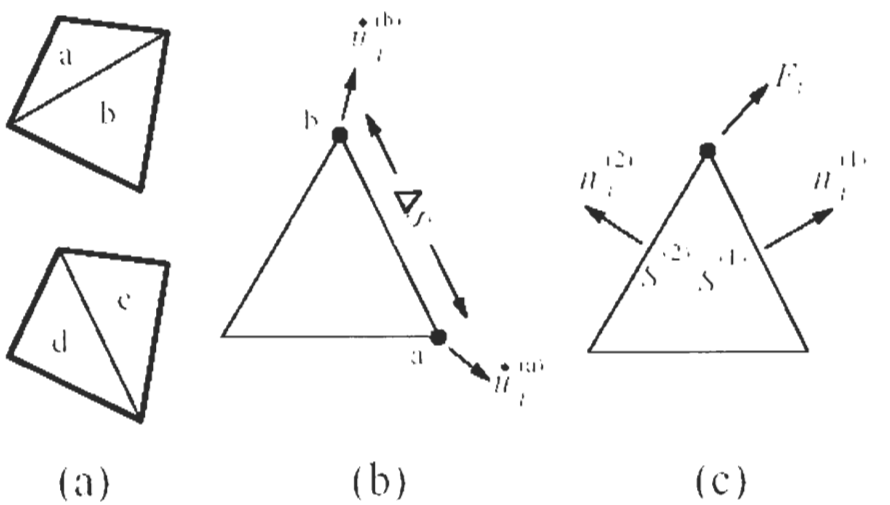


Figure 1.9: (a) Overlaid quadrilateral elements used in FLAC. (b) Typical triangular element with velocity vectors. (c) Nodal force vector (from FLAC, 1998).

Explicit	Implicit
Timestep must be smaller than a critical value for stability	Timestep can be arbitrarily large, with unconditionally stable schemes
Small amount of computational effort per timestep	Large amount of computational effort per timestep
No significant numerical damping introduced for dynamic solution	Numerical damping dependent on timestep present with unconditionally stable schemes
No iterations necessary to follow nonlinear constitutive law	Iterative procedure necessary to follow nonlinear constitutive law
Provided that the timestep criterion is always satisfied, nonlinear laws are always followed in a valid physical way	Always necessary to demonstrate that the above-mentioned procedure is unconditionally stable, and also follows the physically correct path (for path-sensitive problems)
Matrices are never formed. Memory requirements are always at a minimum. No bandwidth limitations	Stiffness matrices must be stored. Ways must be found to overcome associated problems such as bandwidth. Memory requirements tend to be large
Since matrices are never formed, large displacements and strains are accommodated without additional computing effort	Additional computing effort needed to follow large displacements and strains

Figure 1.10: Comparison of explicit and implicit solution methods (From FLAC, 1988).

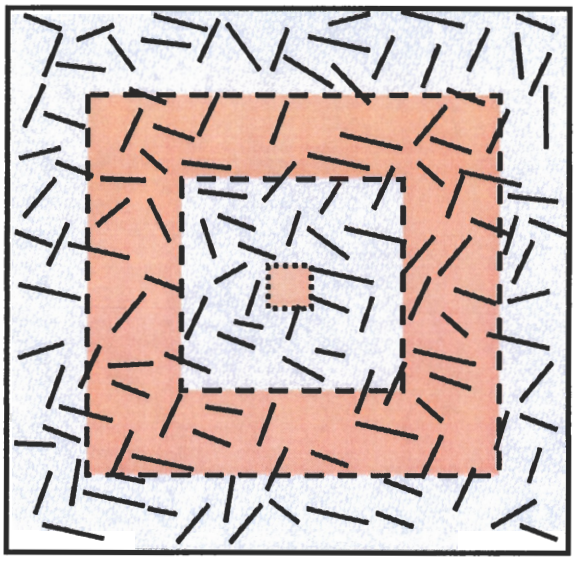


Figure 1.11: Distribution of weak spots in measuring areas of different sizes.

$$\ln(1 - P_f) = \frac{\int_V f(\sigma(x))dV}{V_0} \tag{1.13}$$

where P_f is the failure probability of the structure, V is its volume, V_0 is a representative volume of the material whose strength distribution is given by a cumulative Weibull's distribution $f(\sigma(x))$, and x is the spatial coordinate vector. After integration, for a continuous and homogeneously stressed body, this probability yields a size effect power law of the form:

$$\overline{\sigma_N} = \overline{\sigma_N}\left[\frac{V_0}{V}\right] = k_0 V^{-\frac{1}{m}} = k_0 D^{-\frac{n}{m}} \tag{1.14}$$

where k_0 is a constant that characterizes the structure shape, D is a characteristic dimension (size) of the structure, and n is the number of dimensions. For two-dimensional similarity, $n = 2$. Parameter m is called the Weibull's modulus, an empirical material parameter.

Norman and Wahren (1973) offered an explanation of the scale effect on paper strength within the context of Weibull's statistical theory. Using experimental data by Calvin, they illustrate how paper's strength increases markedly as the test area is decreased. This effect is attributed to the distribution of weak spots (see Figure 1.11) within the sampling area; such a distribution is determined to a large extent by the mass distribution (paper's formation). More recently, Gregersen et al. (1998) have used Weibull's statistics as a tool to evaluate newsprint strength and runnability.

In the classical theories based on plasticity or limit analysis, the strength of geometrically similar structures is independent of the structure size; i.e., there is no size effect on the nominal strength. However, it has been observed that quasi-brittle ma-

terials such as concrete or fiber composites do not follow this trend. The problem of size effect and scaling in the failure of nonhomogeneous materials is a newly emerged subject, which has now been widely recognized by the leading specialists to be a problem of major importance (Bažant and Planas, 1998). It is important both practically, because of its role in design and in testing of material properties, and theoretically, because if the scaling aspects of a physical theory are not correctly understood the theory itself is not correctly understood. As an example, according to Bažant and Chen (1997), only about a decade ago it was generally thought that the size effects in the failure of concrete structures were only statistical or were adequately explained by Weibull's probabilistic theory. Therefore, they were regarded as a matter of study by probability, to be relegated to the safety factors. As recent researches have established, this is true only for brittle structures. It is now generally recognized that this view is in fact incorrect for quasi-brittle structures, for which the maximum load is much larger than the load that initiates the macroscopic crack growth. In quasi-brittle structures, in which large cracks grow in a stable manner before the maximum load, there is a strong nonstatistical size effect due to the release of stored energy caused by fracture growth. It has become clear that such a size effect is often very important and needs to be introduced into the practice and the theory. Further supplementary or competing sources of size effect have also been recently discussed. For example, there exists a formal analogy between the power law governing the fractal nature of the crack surfaces in concrete and the power law describing some types of size effect or scaling (see Carpintieri et al., 1993). The size effects and scaling have been discussed concerning the testing methods for fracture energy and other fracture properties of concrete and fiber reinforced composite. Regarding paper, Östlund and Kärenlampi (1999) presented a modification of Bažant's size effect law for strength. However, they concluded that these scaling laws are sensitive to structural geometry, and thus they would have to be fitted separately for any given geometry

According to Donner (1997), testing the mechanical properties and fracture behavior of paper at cryogenic temperatures isolates the influence of the fiber structure. Cryogenic temperatures suppress the time-dependent viscoelastic behavior of paper, and its behavior is close to that predicted by linear elastic fracture mechanics (LEFM). This also implies that, at sufficiently large scales, paper fracture resistance is independent of paper structure, which in turn can be interpreted as independent of formation (grammage variability) or the local variability of mechanical properties.

In this research the approach to the scaling problem does not fit within any of these categories. The strategy is rather to find the scale-dependent bounds on the elastoplastic constitutive response as illustrated in the following.

1.1.8 Effective material response

Determination of the effective material response from the microstructure usually follows one of four now standard methods (Willis, 1981): (i) rigorous energy bounds (e.g., Hashin-Shtrikman), (ii) perturbation methods, (iii) effective medium models, and (iv) computational methods. They mostly work on the tacit assumption that the scale of the Representative Volume Element (RVE) has been reached. Beginning with

Huet (1990), the last decade has seen the introduction of a fifth approach: bounds that explicitly involve the size of a mesoscale domain relative to the microscale and the type of boundary conditions. An approach with increasing size of such a mesoscale domain, also called a Statistical Volume Element (SVE), to the RVE is of great interest. Random microstructures thus studied progressed from linear elastic (see Ostoja-Starzewski, 2001, for a review) to other types: physically nonlinear elastic (Hazanov, 1998), viscoelastic (Huet, 1995, 1999a), damage phenomena (Huet, 1999b), and, most recently, elastic-plastic (Jiang et al, 2001).

To prepare the basis for elasto-plasticity of paper with random formation, Chapter 2 extends this methodology to rigid-perfectly plastic materials, with a goal of establishing mesoscale yield surfaces and the character of plastic flow for Huber-Mises (HM) materials. The materials are subjected to two kinds of loading: plane deformation rate and plane stress, each under uniform kinematic or traction boundary conditions.

Homogenization of rigid-perfectly plastic materials in a more classical sense, that is, assuming existence of the RVE, has already been studied in the eighties and nineties. Key references here, in the vein of method (i) listed above, are de Buhan (1983), Bouchitte and Suquet (1991), and Suquet (1986, 1993, 1997). Most recent reviews of results in this area in the more general context of nonlinear composites are Ponte Castañeda and Suquet (1998) and Ponte Castañeda (2000).

Wentao et al. (1995, 1996) found bounds on elastic properties of paper by using a mosaic-type model. This model considers paper as a composite material made of fiber segments, bonds, and voids. The fiber bonds are assumed to have uniform strain while the fiber segments have uniform stress. Taking this composite material to be linearly and orthotropically elastic, they found the upper and lower bounds on effective Young's moduli E_x and E_y, shear modulus G_{xy}, and Poisson's ratio ν_{xy} as a function of a cell-wall fibril orientation parameter. Lower bounds were achieved through cell-wall elements assembled in series, having uniform stress (traction boundary conditions). On the other hand, upper bounds were obtained from cell-wall elements assembled in parallel, having uniform strain. The lower and upper bounds on E_x and E_y were found to be "quite far apart."

1.2 Conclusions

Even though variations in formation, fiber orientation, drying strains, furnish, and bonding degree are the origin of paper's macroscopic variation of mechanical properties, the effect of formation seems to be the main factor.

Fiber network micromechanical models are limited by the number of fibers that can be simulated within practical computer-resources. A network of 2,000 fibers, for example, would only represent 1 mm^2 of very low grammage paper. To address the problem of property scaling, it is convenient and necessary to model larger areas of paper. Thus, the appropriate choice for this purpose is a continuum model.

It is clear that the finite element models used to simulate paper have some limitations and can be improved. It is desirable to develop a new model with the characteristics of the models of Wong *et al.* (1996) and Korteoja *et al.* (1998) combined, that is,

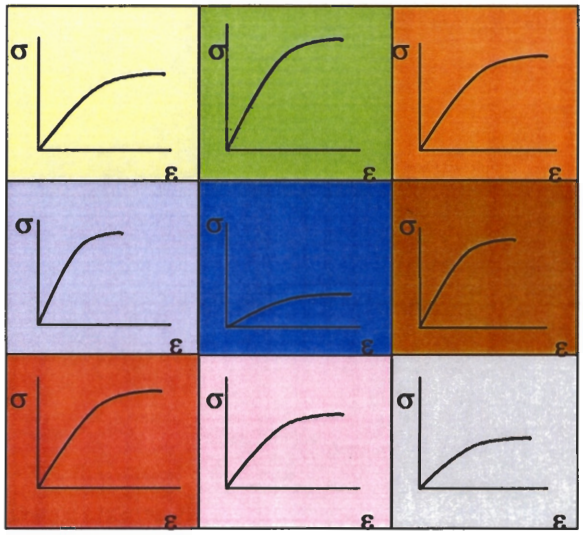


Figure 1.12: Finite element model with individual assignment of nonlinear constitutive law to each cell.

a two-dimensional model permitting individual assignment of mechanical properties to each element, as in the latter model, and the use of a nonlinear constitutive law, as in the first model. Figure 1.12 illustrates this concept schematically. The explicit Finite Difference Element Method allows the combination of these characteristics to model paper efficiently and relatively easily. Furthermore, in contradistinction to the implicit FE methods, FLAC does not require extraordinary computational resources, and large meshes can be run on a regular microcomputer.

1.3 Objectives

Motivated by the foregoing review, the objectives of this dissertation are the following:

1. Develop an FE method appropriate to model paper, in other words, a model that takes into account local variability of paper properties.

2. Search for a nonlinear elastoplastic constitutive law of paper.

3. Provide bounds on effective elastoplastic behavior of paper by using finite sized domains instead of a Representative Volume Element (RVE), which is infinite-sized, or effective medium models, which are not rigorous.

4. Illustrate relationships of the apparent elastoplastic behavior of paper under various uniform boundary conditions, with nonuniform stress or strain fields due to formation.

5. Correlate formation and strain, and, if possible, formation and fracture pattern.

Chapter 2

Plasticity of Huber-Mises Materials with Random Structure

2.1 Background

The present section extends the methodology of bounding effective properties summarized in Section 1.1.8 to rigid-perfectly-plastic materials, with a goal of establishing mesoscale yield surfaces and the character of plastic flow for Huber-Mises (HM) materials. There is a two fold motivation for this: (i) to make a contribution to plasticity of random media (e.g., mild steel); (ii) to provide a stepping-stone to elastoplasticity of paper, a material even more challenging than those modeled by (i). The HM materials are subjected to two kinds of loading: plane deformation rate and plane stress.

Adopting the notation of Suquet (1993), the effective potential of a composite consisting of power law material constituents can be written as:

$$\sigma_{ij} = \sigma_m \delta_{ij} + \sigma_0 \left(\frac{\varepsilon_{eq}}{\varepsilon_0}\right)^{m-1} \frac{2\varepsilon_{ij}}{3\varepsilon_0} = \frac{\partial \varphi(\varepsilon, \mathbf{x})}{\partial \varepsilon_{ij}}. \tag{2.1}$$

Therefore,

$$\varphi(\varepsilon) = \frac{\sigma_0 \varepsilon_0}{m+1} \left(\frac{\varepsilon_{eq}}{\varepsilon_0}\right)^{m+1} \quad \text{if } \mathrm{Tr}\,(\varepsilon) = 0, \quad +\infty \text{ otherwise, with } \varepsilon_{eq} = \left(\frac{2}{3}\varepsilon_{ij}\varepsilon_{ij}\right)^{\frac{1}{2}}, \tag{2.2}$$

where the value $+\infty$ of the potential enforces the constrain of plastic incompressibility. This relation can be given in an equivalent form

$$\varepsilon_{ij} = \varepsilon_0 \left(\frac{\sigma_{eq}}{\sigma_0}\right)^{n-1} \frac{3S_{ij}}{2\sigma_0} = \frac{\partial \psi(\boldsymbol{\sigma})}{\partial \sigma_{ij}}, \tag{2.3}$$

$$\psi(\boldsymbol{\sigma}) = \frac{\sigma_0 \varepsilon_0}{n+1} \left(\frac{\sigma_{eq}}{\sigma_0}\right)^{n+1}, \quad n = \frac{1}{m}$$

where s is the deviatoric part of $\boldsymbol{\sigma}$ and $\boldsymbol{\sigma}_{eq} = \left(\frac{3}{2} s_{ij} s_{ij}\right)^{\frac{1}{2}}$. Rigid ideally plastic materials

are obtained when $m = 0$, $n = +\infty$, while $m = n = 1$ yields linear elastic (Newtonian) materials.

In general, we begin by considering an inhomogeneous medium described pointwise by constitutive relations:

$$\sigma_{ij} = \frac{\partial \phi(\mathbf{d}, \mathbf{x})}{\partial d_{ij}} \quad \text{or equivalently} \quad d_{ij} = \frac{\partial \psi(\boldsymbol{\sigma}, \mathbf{x})}{\partial \sigma_{ij}} \quad \forall \mathbf{x} \in B, \tag{2.4}$$

where ϕ and ψ are conjugate potentials (at $m = 0$ and $n = \infty$) defined over the body domain B in $\mathbb{R}^n$; $\mathbf{d}$ ($\equiv d_{ij}$) and $\boldsymbol{\sigma}$ ($\equiv \sigma_{ij}$) denote deformation rate and Cauchy stress, respectively. The first of these potentials, enforcing the constraint of incompressibility, is

$$\phi(\mathbf{d}) = \begin{cases} k \left(2 d_{(2)}\right)^{1/2} & \text{if} \quad tr(\mathbf{d}) = 0 \ , \\ +\infty & \text{otherwise} \ ; \end{cases} \tag{2.5}$$

and the second one approaches the indicator function of the set delimited by the Huber-Mises (HM) criterion

$$\psi(\boldsymbol{\sigma}) = \begin{cases} 0 \text{ if } & \sigma_{eq} \leq \sigma_0 \ , \\ +\infty & \text{otherwise} \ , \end{cases} \tag{2.6}$$

The macroscopic properties denoted in the spirit of homogenization theory by capital letters of the composite B are governed by conjugate overall potentials Φ and Ψ, which are appropriate infima of the local potentials ϕ and ψ

$$\Sigma_{ij} = \frac{\partial \Phi(\boldsymbol{D})}{\partial D_{ij}} \text{ or equivalently } \quad D_{ij} = \frac{\partial \Psi(\boldsymbol{\Sigma})}{\partial \Sigma_{ij}}, \tag{2.7}$$

They are obtained from the local potentials ϕ and ψ as:

$$\begin{array}{ll} \Phi(\boldsymbol{D}) = \inf_{\mathbf{v} \in \mathcal{E}} \{\phi(\mathbf{d}(\mathbf{v}), \mathbf{x})\} & \mathcal{E} = \{\mathbf{v} \mid \mathbf{v} = \boldsymbol{D} \cdot \mathbf{x} \quad \forall \mathbf{x} \in \partial B \ \}, \\ \Psi(\boldsymbol{\Sigma}) = \inf_{\boldsymbol{\sigma} \in \mathcal{S}} \{\psi(\boldsymbol{\sigma}, \mathbf{x})\} & \mathcal{S} = \{\boldsymbol{\sigma} \mid div \boldsymbol{\sigma} = 0, \ \boldsymbol{\sigma} \cdot \mathbf{n} = \boldsymbol{\Sigma} \cdot \mathbf{n} \quad \forall \mathbf{x} \in \partial B \ \}. \end{array} \tag{2.8}$$

The yield (or extremal) surface of the homogenized composite is defined as:

$$P^{\text{hom}} = \{\boldsymbol{\Sigma} \in \mathbb{R}^{3\times 3} \mid \exists \boldsymbol{\sigma}(\mathbf{x}) \text{ with } \overline{\boldsymbol{\sigma}} = \boldsymbol{\Sigma}, \ div \boldsymbol{\sigma} = 0, \ \sigma_{eq}(\mathbf{x}) \leq \sigma_0(\mathbf{x}), \ \forall \mathbf{x} \in \partial B\} \tag{2.9}$$

The elementary Voigt and Reuss bounds on P^{hom} are expressed via a hierarchy of inclusions

$$\{\boldsymbol{\Sigma} \text{ s.t. } \Sigma_{eq} \leq \inf_{\mathbf{x} \in \mathbf{V}_\delta} \sigma_0(\mathbf{x})\}^{\text{Reuss}} \subset P^{\text{hom}} \subset \{\boldsymbol{\Sigma} \text{ s.t. } \Sigma_{eq} \leq \overline{\sigma_0}\}^{\text{Voigt}} \tag{2.10}$$

On mesoscale (scale smaller than the RVE) there holds some form of apparent yield surface involving an apparent yield condition and some form of an appar-

ent dissipation function. Here the stress and deformation rate need an appropriate interpretation, and we use the term 'some' because the loading conditions on the boundary of a body smaller than the RVE need yet to be specified. Previous studies in micromechanics (Hazanov and Huet, 1995) inform us that only three types of loading are admissible on finite mesoscales–uniform kinematic, uniform traction, and uniform orthogonal-mixed–and that they should result in three disparate, generally anisotropic, responses; anisotropy is present per configuration although it might reduce to isotropy upon ensemble averaging. It is intuitively expected, and has been shown for linear and nonlinear elastic as well as viscoelastic materials, that, on macroscales, all three responses should coincide.

The following sections focus on the responses under uniform kinematic and traction boundary conditions only. The latter one, however, has been noted by several French researchers (Bouchitte and Suquet, 1991; Suquet, 1993, 1997 and references therein) as not appropriate for rigid-perfectly plastic materials. Nevertheless, it is interesting to determine whether this boundary condition would result in any useful lower bound on the macroscopic response, just as in the recently studied case of elastic-hardening plastic materials (Jiang et al., 2001). All these considerations lead to the following questions (see Figure 2.1):

Q1: What is the mesoscale yield condition of finite domains (i.e., below RVE) relative to the response of RVE, in function of the type of boundary condition?

Q2: Is the mesoscale flow rule of finite domains (i.e., below RVE) normal, given that the response of constituent phases are normal (see Figure 2.2)?

Q3: What is the effect of ensemble averaging (i.e., over Ω) with respect to the issues raised in Q1 and Q2?

Q4: While the yield surface of either phase in plane strain (respectively, plane stress) consists, in the principal directions system, of two parallel lines (respectively, of an ellipse), what shape does it have for a random composite?

Q5: What is the scatter in yield surfaces as we change the mesoscale?

The next section gives basic definitions and the problem formulation. Section 2.3 then gives an extension of the Hill condition (Hill, 1963) to rigid-plastic materials and key results of qualitative nature on scale-dependent bounding of the macroscopic yield condition and the macroscopic dissipation function under kinematic and traction boundary conditions, respectively from above and from below. Section 2.4 presents computational mechanics studies for plane deformation rate and plane stress responses of a transversely isotropic composite with a random chessboard microgeometry. From this emerges a variety of features of mesoscale response (shape of apparent yield surfaces and apparent flow properties) under both types of boundary conditions. Finally, Section 2.5 recapitulates the answers to the five questions above.

2.2 Rigid-plastic microstructures

Consider random, multiphase, everywhere perfectly bonded microstructures in two or three dimensions that have statistically homogeneous and ergodic geometries with a single characteristic microscale δ. Each phase r $(= 1, ...r_{tot})$ is incompressible,

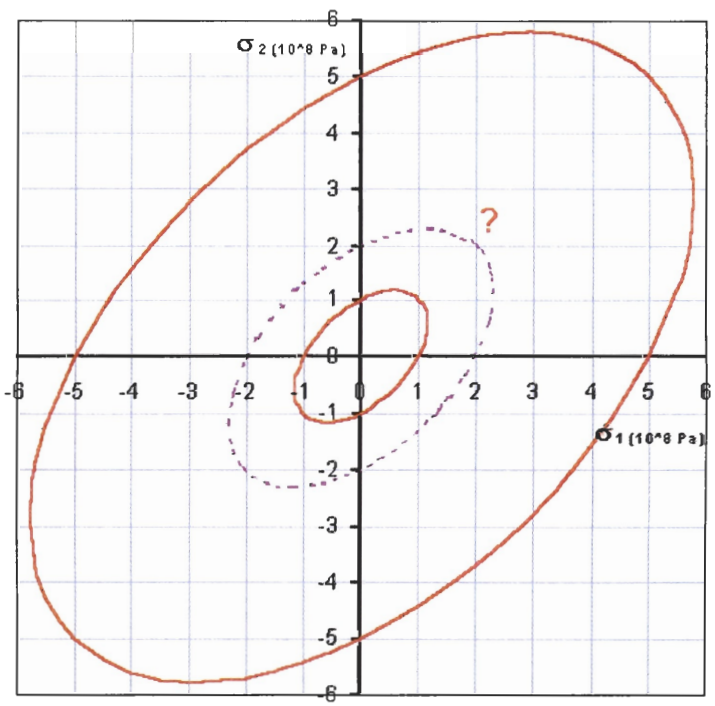


Figure 2.1: Yield surface of soft (inner ellipse) and hard phases (outer ellipse) in plane stress. Where is the resulting yield surface of a two-phase composite?

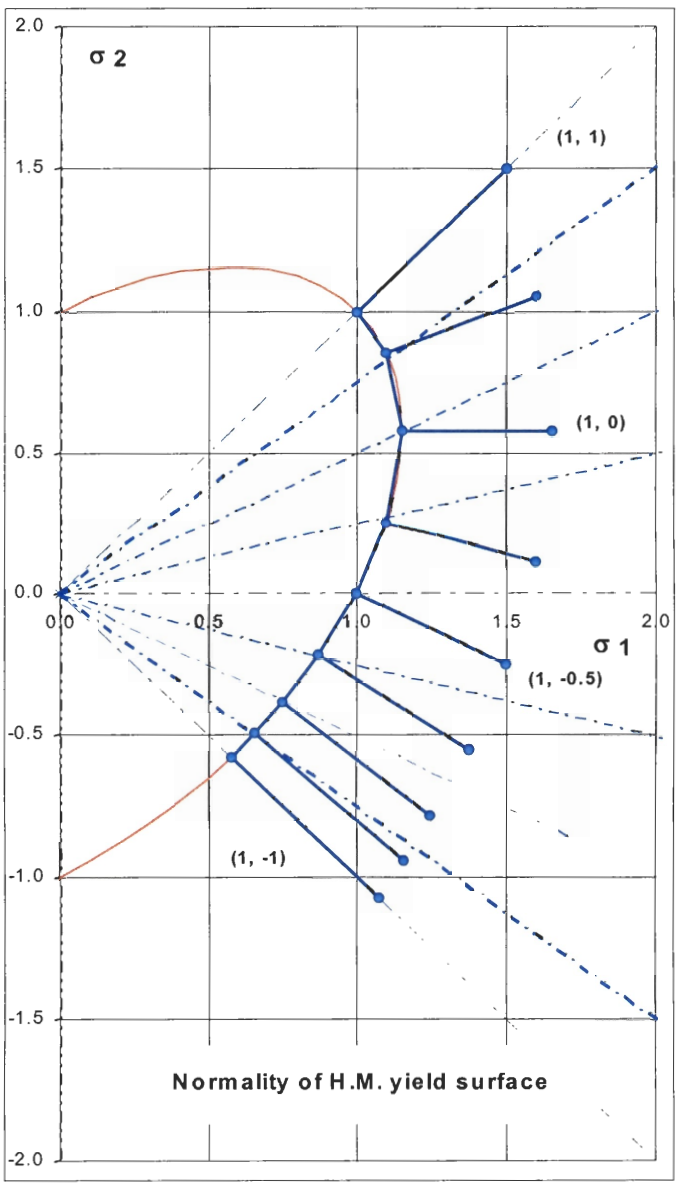


Figure 2.2: The yield surface of a Huber-Mises material in plane stress ($\sigma_{33} = 0$) is an ellipse. The deformation rate vectors $\mathbf{d}$ are normal to this yield surface for an associated flow rule.

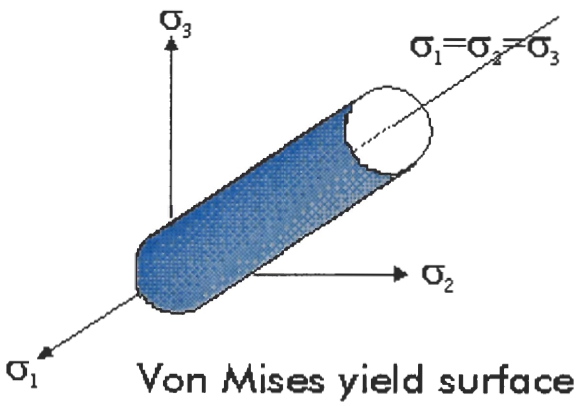


Figure 2.3: Huber-Mises yield surface is a cylinder in stress space.

rigid-plastic, isotropic of the Huber-Mises type (HM), that is, having a yield condition

$$F_r(\sigma_{ij}) = \sigma'_{(2)} - k_r^2 = 0, \tag{2.11}$$

and a plastic response following the associated flow rule

$$d_{ij} = \lambda \sigma'_{ij} \quad \text{whenever} \quad F_r(\sigma_{ij}) = 0 \quad \text{and} \quad dF_r \geq 0 \ . \tag{2.12}$$

In a three-dimensional stress space, this yield condition is represented by a cylinder as shown in Figure 2.3. Equivalently, the HM material of phase r can be defined in terms of the dissipation function (Ziegler, 1983)

$$\Phi_r(d_{ij}) = k_r \left[d_{(2)}\right]^{1/2}, \tag{2.13}$$

with (dissipative) stresses derivable from Φ_r, on account of incompressibility ($d_{ii} = 0$), as

$$\sigma_{ij} = \frac{\partial \Phi_r}{\partial d_{ij}} - \gamma \delta_{ij}, \tag{2.14}$$

where γ is a Lagrangian multiplier. This leads to

$$\sigma_{ij} = k_r \left[d_{(2)}\right]^{-1/2} d_{ij}, \tag{2.15}$$

which is equivalent to the flow rule (2.12).

Effectively, the random HM material is thus described by three coefficients: volume fractions of all the phases, grain size d, and spatial random variability of all the phases. In the special case of a two-phase material (Section 2.4 below), we deal with the mismatch of phases (contrast) $\alpha = k_2/k_1$. The random material is denoted $\mathcal{B}_\delta = \{B_\delta(\omega); \omega \in \Omega\}$ with $B_\delta(\omega)$ being one realization.

If we introduce a finite-sized, arbitrarily placed domain, we arrive at a fourth

parameter $\delta = L/d$, a so-called *mesoscale*. Properties on mesoscale are also described by an adjective *apparent* (Huet, 1995), as opposed to *effective*. The latter term pertains to the limit $\delta \to \infty$ as it connotes the passage to the RVE, while any finite mesoscale involves scatter and, therefore, describes some SVE.

For a mesoscale body $B_\delta(\omega)$ of volume V_δ, volume average stress and deformation rate are defined as

$$\overline{\overline{\boldsymbol{\sigma}}}_\delta(\omega) = \frac{1}{V_\delta}\int \boldsymbol{\sigma}(\boldsymbol{\omega}, \mathbf{x})dV \quad \overline{\mathbf{d}}_\delta(\omega) = \frac{1}{V_\delta}\int \mathbf{d}(\boldsymbol{\omega}, \mathbf{x})dV \ , \tag{2.16}$$

so that, for the macroscopic body $B_{\delta\to\infty}(\omega)$, in the notation of homogenization theory, we have

$$\boldsymbol{\Sigma}(\omega) = \overline{\boldsymbol{\sigma}}_{\delta\to\infty}(\omega) \quad \boldsymbol{D}(\omega) = \overline{\mathbf{d}}_{\delta\to\infty}(\omega) \ . \tag{2.17}$$

Consistent with the ergodic postulate in our model, $\boldsymbol{\Sigma}(\omega)$ and $\boldsymbol{D}(\omega)$ on the left-hand sides in the above are almost surely identical for each and every $\omega \in \Omega$. The limit $\delta \to \infty$ should be taken in such a way that L is kept finite to keep the energy dissipation finite (see Figure 2.4(a) and (b)). The particular microstructures shown here are realizations of a planar random chessboard, playing in Section 2.4 the role of a model of polycrystal. On mesoscale there holds some form of apparent yield surface involving an apparent yield condition and some form of an apparent dissipation function

$$P_\delta = \{\overline{\boldsymbol{\sigma}}_\delta | F_\delta(\overline{\boldsymbol{\sigma}}_\delta) \leq 0\}, \qquad \Phi_\delta(\overline{\mathbf{d}_\delta}), \tag{2.18}$$

the actual forms of which depend on the types of boundary conditions applied to ∂B_δ.

2.3 Mechanics of rigid-plastic microstructures on mesoscales

2.3.1 Extension of Hill condition to rigid-plastic materials

Consider stress ($\boldsymbol{\sigma}(\mathbf{x})$) and deformation rate ($\mathbf{d}(\mathbf{x})$) fields in a specimen $B_\delta(\omega)$ of the random material $\mathcal{B}_\delta = \{B_\delta(\omega); \omega \in \Omega\}$. They can be written as volume averages $\overline{\boldsymbol{\sigma}}$ and $\overline{\boldsymbol{d}}$ (indicated by an overbar) superposed with zero-mean spatial fluctuations ($\overline{\boldsymbol{\sigma}'} = \mathbf{0}$ and $\overline{\boldsymbol{d}'} = \mathbf{0}$)

$$\boldsymbol{\sigma}(\mathbf{x}) = \overline{\boldsymbol{\sigma}} + \boldsymbol{\sigma}'(\mathbf{x}) \quad \mathbf{d}(\mathbf{x}) = \overline{\mathbf{d}} + \mathbf{d}'(\mathbf{x}) \tag{2.19}$$

Now, recalling that the dissipation function Φ is a scalar product of the (dissipative) stresses and deformation rates, its volume average over $B_\delta(\omega)$ is

$$\overline{\Phi} = \overline{\boldsymbol{\sigma} \cdot \mathbf{d}} = \overline{\boldsymbol{\sigma}} \cdot \overline{\mathbf{d}} + \overline{\boldsymbol{\sigma}' \cdot \mathbf{d}'} \tag{2.20}$$

Clearly, for the product of volume averages to equal the volume average of the product

$$\overline{\boldsymbol{\sigma} \cdot \mathbf{d}} = \overline{\boldsymbol{\sigma}} \cdot \overline{\mathbf{d}} \tag{2.21}$$

we must have $\overline{\boldsymbol{\sigma}' \cdot \mathbf{d}'} = 0$. Equation (2.21) may be called the *Hill condition for dissipative processes* (see also Huet, 1982).

For an unbounded space domain ($\delta \to \infty$), as is the case in deterministic thermomechanics of homogeneous media, (2.21) is trivially satisfied. However, for a finite body $B_\delta(\omega)$ this requires that the body be loaded in a specific way on its boundary ∂B_δ. Generalizing (Hazanov and Amieur, 1995), from (2.21), by employing the Green-Gauss theorem, we find a necessary and sufficient condition for it to hold

$$\overline{\boldsymbol{\sigma} \cdot \mathbf{d}} = \overline{\boldsymbol{\sigma}} \cdot \overline{\mathbf{d}} \Longleftrightarrow \int_{\partial B_\delta} (\mathbf{t} - \overline{\boldsymbol{\sigma}} \cdot \mathbf{n}) \cdot (\mathbf{v} - \overline{\mathbf{d}} \cdot \mathbf{x}) dS = 0. \tag{2.22}$$

Now, relation (2.22, right side) distinguishes three types of boundary conditions on the mesoscale:

uniform kinematic

$$\mathbf{v}(\mathbf{x}) = \mathbf{d}^0 \cdot \mathbf{x} \quad \forall \mathbf{x} \in \partial B_\delta; \tag{2.23}$$

uniform traction

$$\mathbf{t}(\mathbf{n}) = \boldsymbol{\sigma}^0 \cdot \mathbf{n} \quad \forall \mathbf{n} \in \partial B_\delta; \tag{2.24}$$

uniform kinematic-traction

$$(\mathbf{t}(\mathbf{n}) - \boldsymbol{\sigma}^0 \cdot \mathbf{n}) \cdot (\mathbf{v}(\mathbf{x}) - \mathbf{d}^0 \cdot \mathbf{x}) = 0 \quad \forall \mathbf{x} \in \partial B_\delta. \tag{2.25}$$

Here $\mathbf{t}$ and $\mathbf{v}$ denote surface traction and velocity fields, respectively. Henceforth, the examples focus on the first two conditions and do not consider the third one.

2.3.2 Bounding on mesoscales via kinematic and traction boundary conditions

Let $P^d_{F(\overline{\boldsymbol{\sigma}}_\delta(\omega))}$ denote the yield locus of a body $B_\delta(\omega)$ under uniform kinematic boundary condition (2.23); superscript d indicates it is displacement controlled. In the ensemble sense we have a random locus $\left\{P^d_{F(\overline{\boldsymbol{\sigma}}_\delta(\omega))}; \omega \in \Omega\right\}$ given the fact that there is a set $\{B_\delta(\omega); \omega \in \Omega\}$. Upon averaging, we have $P^d_{F(\langle\overline{\boldsymbol{\sigma}}_\delta\rangle)}$.

Similarly, let $P^t_{F(\overline{\boldsymbol{\sigma}}_\delta(\omega))}$ denote the yield locus of a body $B_\delta(\omega)$ under condition (2.24); superscript t indicates it is traction controlled. In the ensemble sense we have a random locus $\left\{P^t_{F(\overline{\boldsymbol{\sigma}}_\delta(\omega))}; \omega \in \Omega\right\}$ given the fact that there is a set $\{B_\delta(\omega); \omega \in \Omega\}$. Upon averaging, we have $P^t_{F(\langle\overline{\boldsymbol{\sigma}}_\delta\rangle)}$.

It has been shown (see Jiang et al., 2001), on the basis of (i) extremum principles of plasticity and (ii) the property of spatial homogeneity and ergodicity of the microstructure, that the uniform kinematic and uniform traction boundary conditions applied to $\{B_\delta(\omega); \omega \in \Omega\}$ bound in terms of ensemble averages, respectively from above and below, the yield surface $P^{\text{hom}} = P_{F(\langle\overline{\boldsymbol{\sigma}}_\infty\rangle)}$ of the infinite sized body B_∞. Thus, for (2.23), we have

$$P_{F(\langle\overline{\boldsymbol{\sigma}}_\infty\rangle)} \subseteq ... \subseteq P^d_{F(\langle\overline{\boldsymbol{\sigma}}_\delta\rangle)} \subseteq P^d_{F(\langle\langle\overline{\boldsymbol{\sigma}}_{\delta/2}\rangle\rangle)} \subseteq ... \subseteq P^d_{F(\langle\overline{\boldsymbol{\sigma}}_1\rangle)}. \tag{2.26}$$

where $P^d_{F(\langle\overline{\boldsymbol{\sigma}}_1\rangle)}$ may be interpreted as a uniform deformation rate bound (in the sense of Taylor, 1938) on the macroscopic yield locus $P_{F(\langle\overline{\boldsymbol{\sigma}}_\infty\rangle)}$. On the other hand, for (2.24), we have

$$P^t_{F(\langle\overline{\boldsymbol{\sigma}}_1\rangle)} \subseteq ... \subseteq P^t_{F(\langle\langle\overline{\boldsymbol{\sigma}}_{\delta/2}\rangle\rangle)} \subseteq P^t_{F(\langle\overline{\boldsymbol{\sigma}}_\delta\rangle)} \subseteq ... \subseteq P_{F(\langle\overline{\boldsymbol{\sigma}}_\infty\rangle)} \tag{2.27}$$

where $P^t_{F(\langle\overline{\boldsymbol{\sigma}}_1\rangle)}$ may be interpreted as a uniform stress bound (in the sense of Sachs, 1928) on $P_{F(\langle\overline{\boldsymbol{\sigma}}_\infty\rangle)}$. The following sections consider two particular cases of these bounds for HM materials of special type.

2.4 Plane deformation rate and plane stress responses of random Huber-Mises material

Consider a two-phase material with microgeometry of a random chessboard in two dimensions (x_1 and x_2) (see Figure 2.4(a) and (b)). This is a system of phase 1 (white) and phase 0 (black) square grains $d \times d$, all aligned with the x_3 direction. More precisely, the microgeometry of phase $r = 1$ is taken as a Bernoulli lattice process $\Pi_{p,d}$ (p is a site probability) on a Cartesian lattice of spacing d in $\mathbb{R}^2$ (Stoyan et al., 1987)

$$\mathcal{L}_d = \{\mathbf{x} = (m_1 d, m_2 d)\} \quad m_1, m_2 \in \mathbb{N} \tag{2.28}$$

Any configuration $B(\omega)$ of this piecewise-constant material is described by an indicator function $\chi(\omega, \mathbf{x})$ taking values 1 and 0 according as $\mathbf{x}$ falls in phase 1 and 0, respectively.

The mismatch of phases is set to $\alpha = k_2/k_1$ and the nominal volume fraction of white and black phases to 50%; on finite scales ($\delta < \infty$) there are, of course, local fluctuations from one $B_\delta(\omega)$ to another; this is reflected in our pictures. More specifically, two domain sizes, $\delta = 10$ and 50, are considered. Response of any given specimen $B_\delta(\omega)$, generated according to this Bernoulli lattice process, is obtained by a finite element method "fast Lagrangian analysis of continua" (FLAC, 1998). We shall next study 50 specimens at mesoscale $\delta = 10$ and 20 specimens at $\delta = 50$. These numbers reflect the fact that the larger the scale the smaller is the scatter, and hence, the number of realizations required.

2.4.1 Plane deformation rate

General Equation (2.11) can be written as:

$$F_r(\boldsymbol{\sigma}) = (\sigma_{11} - \sigma_{22})^2 + (\sigma_{22} - \sigma_{33})^2 + (\sigma_{33} - \sigma_{11})^2 - 4\sigma_{12} - 4k_r^2 \tag{2.29}$$

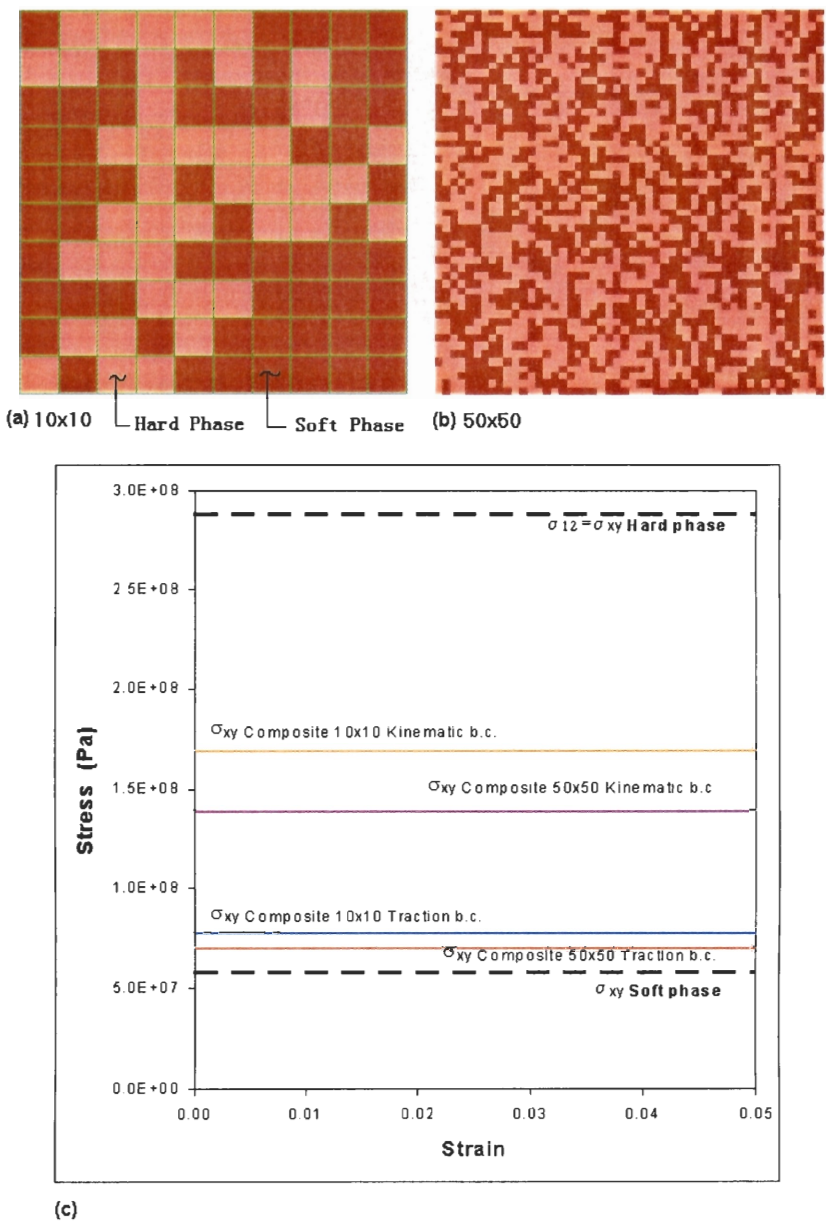


Figure 2.4: Two realizations of a random, two-phase chessboard material, of nominal volume fractions 50%, in finite-size windows (a) 10×10 and (b) 50×50. (c) The corresponding apparent rigid-plastic responses at contrast 5 under uniform kinematic and uniform traction boundary conditions.

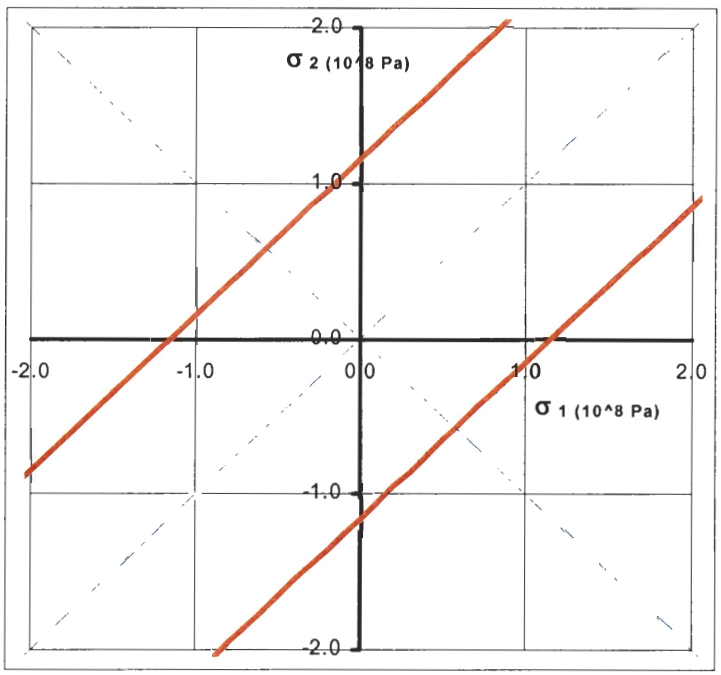


Figure 2.5: Yield locus for plane deformation rate (plane strain). The yield surface is described by: $\sigma_2 = \sigma_1 \pm \sqrt{\frac{2}{3}}\sigma_{yield}$.

For a plane deformation rate (plane strain), we have

$$\sigma_{33} = \frac{(\sigma_{11} + \sigma_{22})}{2}.$$

Therefore, the yield condition (2.11) now simplifies to

$$F_r(\boldsymbol{\sigma}) = (\sigma_{11} - \sigma_{22})^2 - 4\sigma_{12} - 4k_r^2 \tag{2.30}$$

and the flow rule (2.12) leads to

$$\frac{d_{11}}{\sigma_{11} - \sigma_m} = \frac{d_{22}}{\sigma_{22} - \sigma_m} = \frac{d_{12}}{\sigma_{12}} \tag{2.31}$$

where $\sigma_m = (\sigma_{11} + \sigma_{22})/2$ is the mean stress.

When $F_r(\boldsymbol{\sigma}) = 0$, the yield locus can be represented by two parallel lines because, in the plane of principal stresses, Equation (2.30) becomes:

$$\sigma_{22} = \sigma_{11} \pm \sqrt{\frac{2}{3}}\sigma_{yield}. \tag{2.32}$$

These lines, shown in Figure 2.5, are like the projection of the cylinder that represents the Huber-Mises condition shown in Figure 2.3.

On mesoscale the actual form of the dissipation function has to account for anisotropy, so that we may postulate the simplest generalization of (2.13), namely

$$\Phi_\delta(\mathbf{d},\omega) = [d_{ij} M_{ijkl_\delta}(\omega) d_{kl}]^{1/2} \tag{2.33}$$

whereby, writing $M_{ijkl} \equiv M_{jikl_\delta}$ for simplicity of notation, we note the symmetries

$$M_{ijkl} = M_{jikl} = M_{ijlk} = M_{klij} \tag{2.34}$$

This reduces to the isotropic form upon setting

$$\begin{array}{c} M_{1111} = ... = 2M_{1212} = ... = 2k^2 \\ M_{1122} = ... = M_{1222} = ... = 0 \end{array} \tag{2.35}$$

and this definitely occurs in the pointwise limit $\delta \to 0$ with k becoming k_r according to the local phase r. As pointed out by Questions 1-4 in Section 2.1, when $\delta \to \infty$, an effective HM material may perhaps be recovered, whereby k would become k^{eff}; the latter quantity needs to be determined by either a variational method for the RVE, or an effective medium theory, or a computational micromechanics as done below.

On mesoscale, by thermodynamic orthogonality, we have for any given $B_\delta(\omega)$

$$\begin{array}{l} \sigma'_{11} = [d_{ij} M_{ijkl}(\omega) d_{kl}]^{-1/2} [2d_{11} M_{1111} + 2d_{22} M_{2211} + 4d_{12} M_{1211}] \\ \sigma'_{22} = [d_{ij} M_{ijkl}(\omega) d_{kl}]^{-1/2} [2d_{11} M_{1122} + 2d_{22} M_{2222} + 4d_{12} M_{1222}] \\ \sigma'_{12} = [d_{ij} M_{ijkl}(\omega) d_{kl}]^{-1/2} [4d_{11} M_{1112} + 4d_{22} M_{2212} + 8d_{12} M_{1212}] \end{array} \tag{2.36}$$

While the M_{ijkl} coefficients may be determined from appropriate loading cases, it cannot be guaranteed that there is normality of the $\overline{\boldsymbol{d}}_\delta$ vector in the stress space; this is discussed below.

Numerical Results Figures 2.6 and 2.7 show the apparent plastic responses, in terms of the von Mises strain, of the Huber-Mises two-phase chessboards at contrast 5, of respective Figures 2.4(a) and (b) on mesoscales $\delta = 10$ (a) and 50 (b). The loading is of shear type: $d^0_{11} = -d^0_{22}$, $d^0_{12} = 0$ for the kinematic boundary conditions (left column), and $\sigma_{11} = -\sigma_{22}$, $\sigma_{12} = 0$ for the traction boundary conditions (right column). The inhomogeneity of strain fields, especially under the traction conditions, is evident. As the scale δ increases, there is a clear tendency for responses under both types of loading to attain spatial uniformity and similarity.

While this tendency to homogenization was noted in a similar study in Jiang et al. (2001), the key difference of the present model from the matrix-inclusion composite studied there is that the random two-phase chessboard at 50% volume fraction is *below the percolation of either phase*, because the critical probability in a site-percolation problem is about 59% (Ziman, 1979). Thus, there are no shear bands spanning the entire material domain through zones of soft material only because the soft phase does not percolate (or interconnect the entire material domain). To enable a global plastic flow, portions of hard material need to yield in the most critical spots separating the soft phases. Strictly speaking, the shear bands probably involve infinitesimally thin

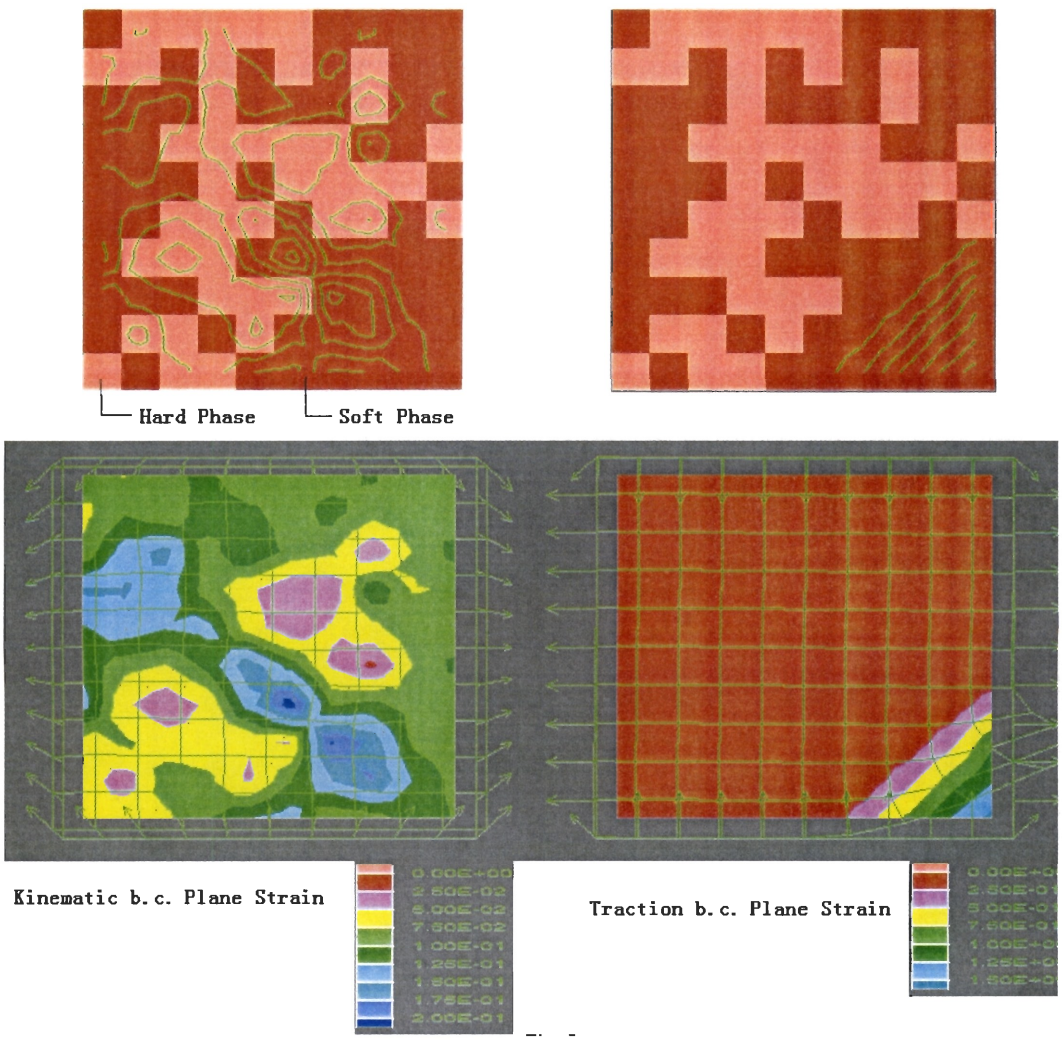


Figure 2.6: Apparent plastic responses (shown in terms of the von Mises strain) of the two-phase 10×10 chessboard in plane deformation rate (called 'plane strain' for short) under kinematic and traction boundary conditions.

slip-lines, which, however, cannot be well resolved given the selected mesh with one finite element per one chessboard square.

The trend of theoretically derived bounding yield surfaces to converge with increasing mesoscale is displayed in Figure 2.8. In particular, for two mesoscales, $\delta = 10$ and 50, it shows apparent yield surfaces under kinematic and traction loadings. Interestingly, the ensemble averaged yield loci under the latter loading do show the scale effect: larger scale leads to a higher yield limit. The corresponding scatter, only shown for kinematic loading at $\delta = 10$, decreases with δ going up. The vectors of deformation rate $\overline{\boldsymbol{d}}$ (not drawn here) satisfying the normality of flow rule holds in the ensemble average sense, but not per single realization $\omega \in \Omega$.

2.4.2 Plane stress

General For plane stress $\sigma_{33} = 0$. Therefore, the yield condition (2.11 or 2.29) readily simplifies to

$$F_r(\boldsymbol{\sigma}) = \sigma_{11}^2 - \sigma_{11}\sigma_{22} + \sigma_{11}^2 + 3\sigma_{12}^2 - 3k_r^2 \tag{2.37}$$

and the flow rule (2.13) leads to

$$\frac{d_{11}}{2\sigma_{11} - \sigma_{22}} = \frac{d_{22}}{2\sigma_{22} - \sigma_{11}} = \frac{d_{12}}{6\sigma_{12}} \tag{2.38}$$

It will turn out below that an anisotropic form of apparent yield surfaces $F_\delta(\boldsymbol{\sigma})$ will be relevant. Its convenient form in the space of principal stresses σ_1 and σ_2, actually employed for homogenous transversely isotropic materials (e.g., Mellor, 1982), is:

$$F_\delta(\boldsymbol{\sigma}) = (\sigma_1 + \sigma_2)^2 + (1 + 2R_\delta)(\sigma_1 - \sigma_2)^2 - 2(1 + R_\delta)\sigma_{u\delta}^2 \tag{2.39}$$

Here $\sigma_{u\delta}$ is the yield stress in uniaxial tension, with δ denoting its scale dependence. Similarly, in general, R_δ is scale-dependent. This yield locus is an ellipse, as shown in Figure 2.9, and it corresponds to the intersection of the HM yield surface cylinders shown in Figure 2.3 with the σ_1-σ_2-plane. The equation of this ellipse is (2.37), which can also be written as:

$$\sigma_1^2 - \sigma_1\sigma_2 + \sigma_2^2 = \sigma_{yield}^2 \tag{2.40}$$

Numerical Results Figures 2.10 and 2.11 display apparent plastic responses, in terms of the von Mises strain, of the Huber-Mises two-phase chessboards at contrast 5, of respective Figure 2.4 on mesoscales $\delta = 10$ (a) and 50 (b). The loading is again of shear type: $d_{11}^0 = -d_{22}^0$, $d_{12}^0 = 0$ for the kinematic boundary conditions (left column), and $\sigma_{11}^0 = -\sigma_{22}^0$, $\sigma_{12}^0 = 0$ for the traction boundary conditions (right column). The inhomogeneity of strain fields, especially under the traction conditions, is evident. As the scale δ increases, there is a clear tendency for responses under both types of loading to attain spatial uniformity and similarity.

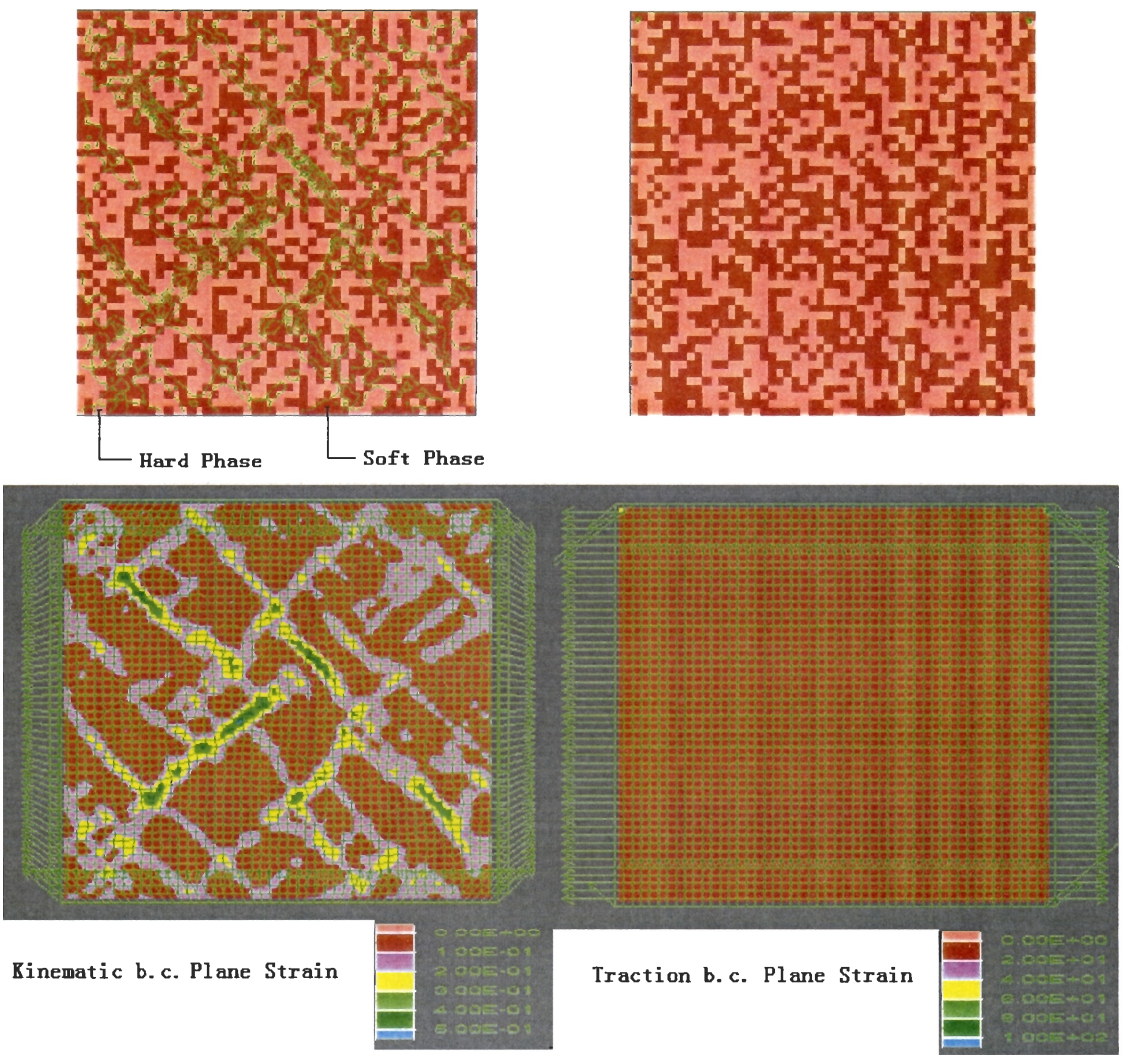


Figure 2.7: Apparent plastic responses (shown in terms of the von Mises strain) of the two-phase 50×50 chessboard in plane deformation rate (called 'plane strain' for short) under kinematic and traction boundary conditions.

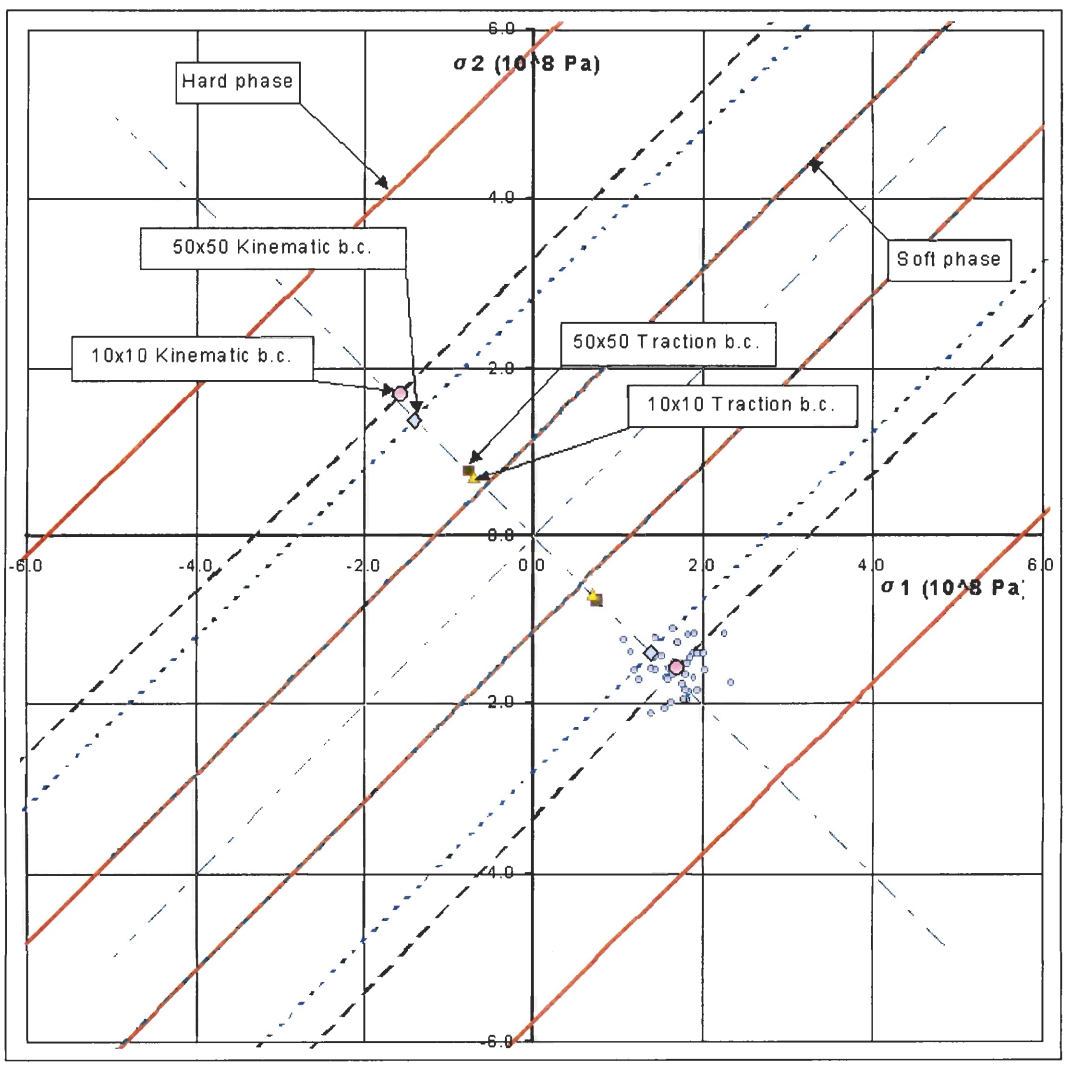


Figure 2.8: An ensemble view of apparent yield surfaces of random Huber-Mises two-phase chessboards in plane deformation rate on mesoscales $\delta = 10$ and 50. Hard and soft phase yield loci are shown, too.

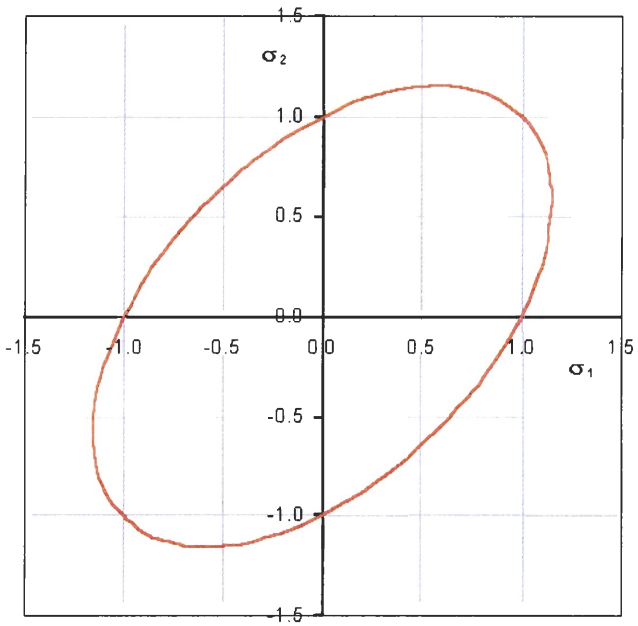


Figure 2.9: Huber-Mises yield locus for planes stress. Yield surface is described by: $\sigma_1^2 - \sigma_1\sigma_2 + \sigma_2^2 = \sigma_{yield}^2$ ($\sigma_{yield} = 1$ in this example).

Figure 2.10 gives apparent plastic responses (shown in terms of the von Mises strain) of the two-phase 10 × 10 chessboard of Figure 2.4(a), in plane stress under kinematic (left column) and traction (right column) boundary conditions. Note the strong difference of kinematic-controlled, *but not* traction-controlled, responses (left columns) between the plane stress and the plane strain response of Figure 2.6.

In Figure 2.11, the same study continues by giving apparent plastic responses (shown in terms of the von Mises strain) of the two-phase 50 × 50 chessboard of Figure 2.4(b) in plane stress under kinematic (left column) and traction (right column) boundary conditions. Note here the formation of shear band features under traction condition, which was brought out at 0.01 level of the maximum von Mises strain.

Figure 2.12 gives an ensemble view of apparent yield surfaces in the (σ_1, σ_2)-plane on mesoscales $\delta = 10$ and 50; in other words, fifty and twenty realizations of chessboards were employed. Hard and soft phase yield loci at contrast 5, having the classical HM elliptical shape, are shown for reference. Also drawn is the ensemble average kinematic-controlled yield locus and two most extreme ones for scale $\delta = 50$; their symmetry with respect to the origin of (σ_1, σ_2)-plane is noted. Two Huber-Mises ellipses are drawn in broken lines for reference so as to display the departure of these apparent (mesoscale) responses from the HM response.

This departure is made more visible in Figure 2.13 representing a close-up view of a part of Figure 2.12, focusing on the quarter of apparent yield surfaces from shear up to uniaxial (ex)tension, on mesoscales $\delta = 10$ and 50. It is evident that the form (2.39)

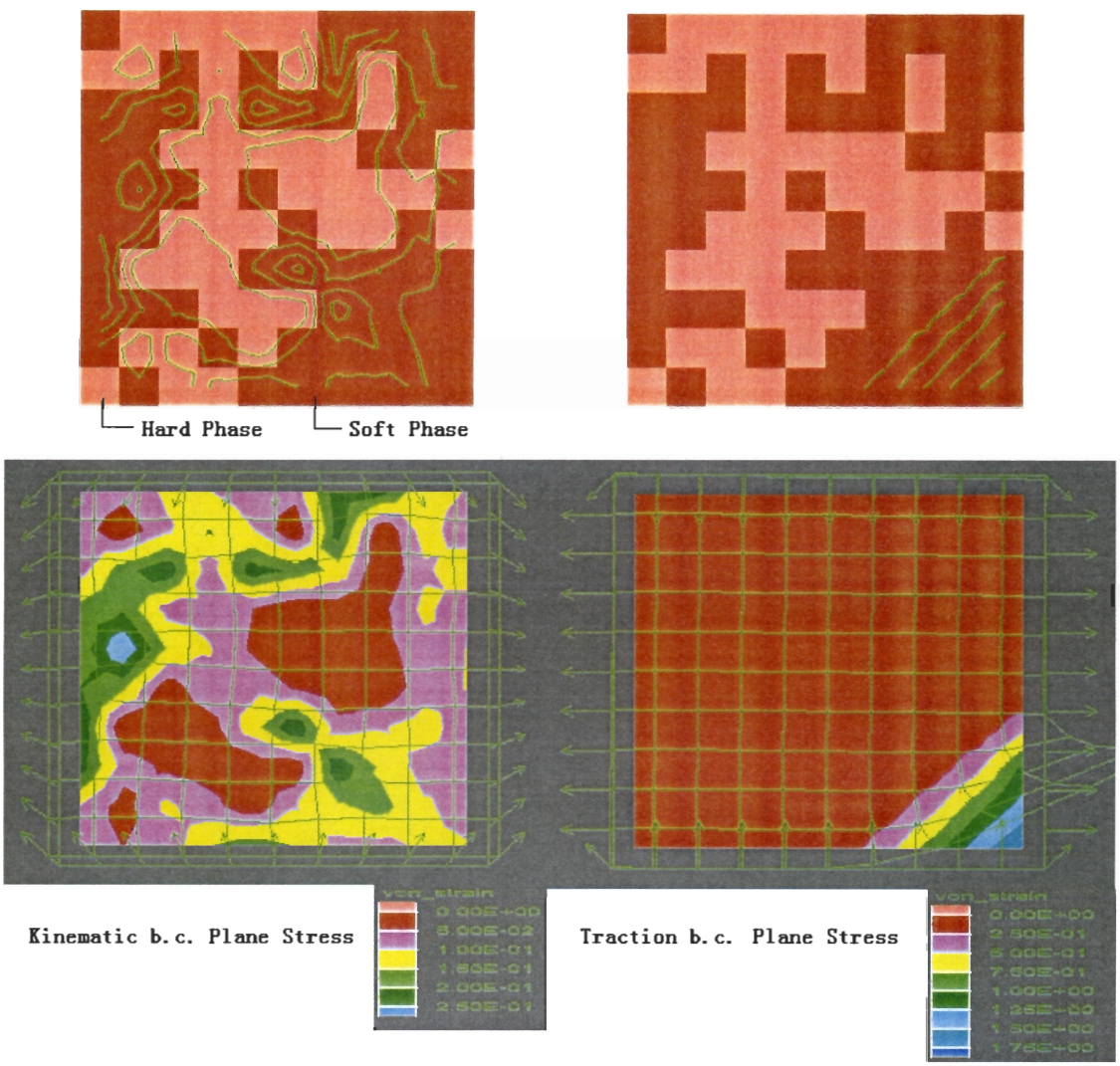


Figure 2.10: Apparent plastic responses (von Mises strain) of the two-phase 10×10 chessboard in plane stress under kinematic and traction boundary conditions.

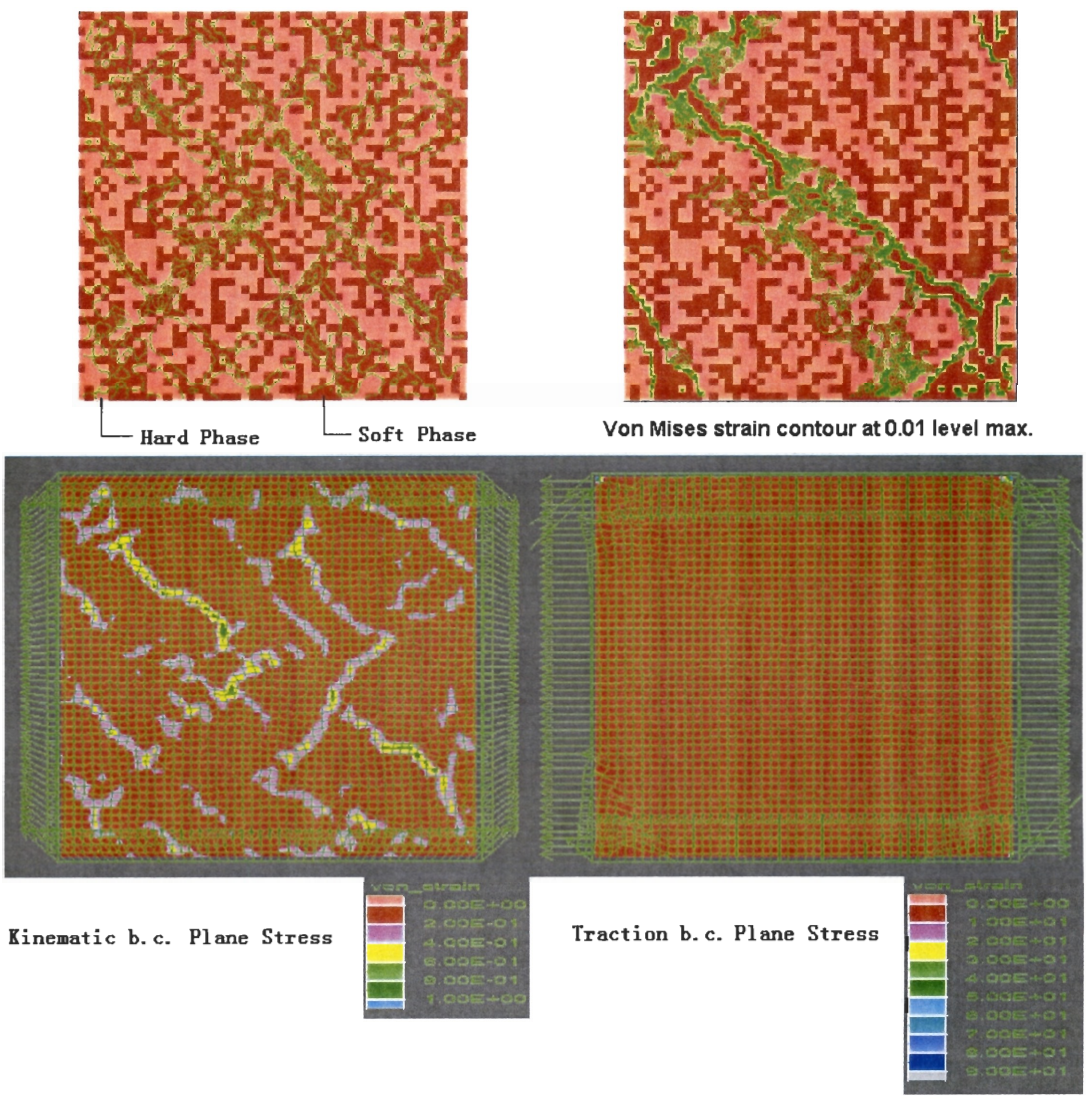


Figure 2.11: Apparent plastic responses (von Mises strain) of the two-phase 50×50 chessboard in plane stress under kinematic and traction boundary conditions.

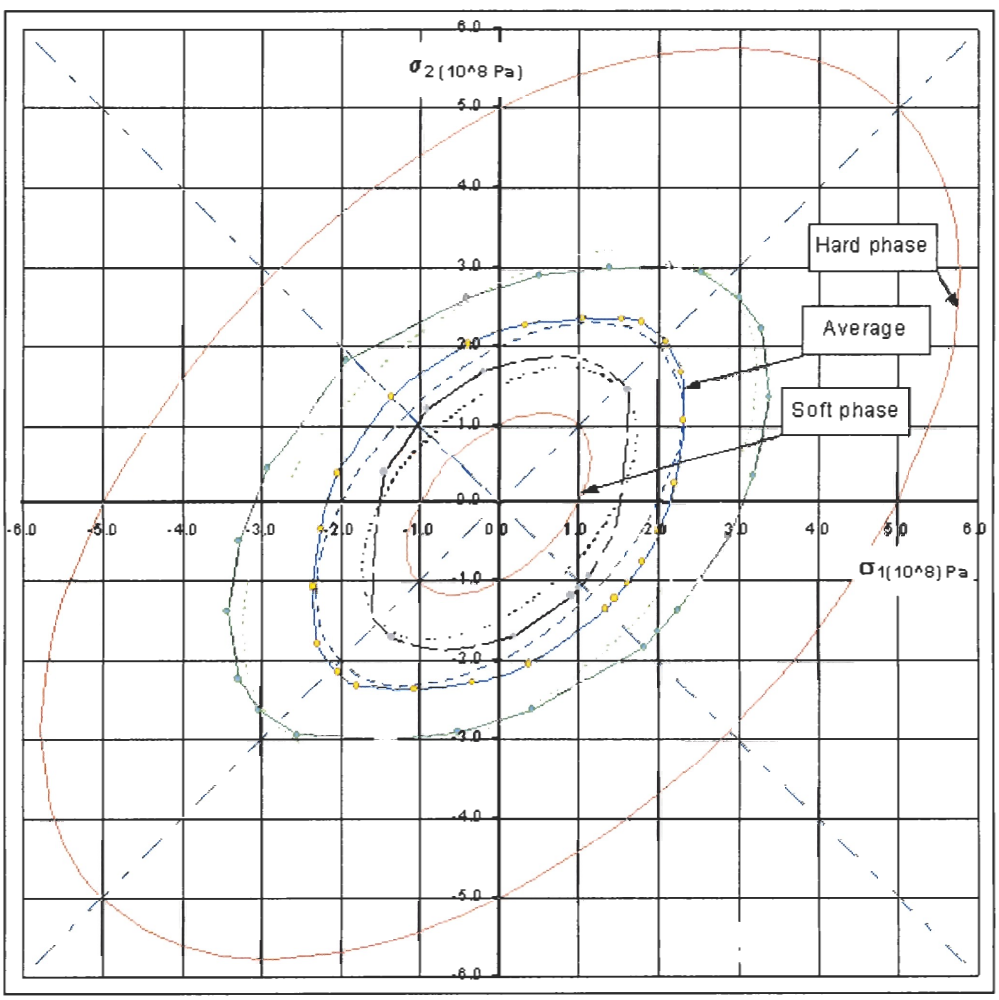


Figure 2.12: An ensemble view of apparent yield surfaces under kinematic conditions in plane stress on mesoscales $\delta = 10$ and 50. Hard and soft phase yield loci, as well as an average kinematic-controlled locus and two most extreme ones on $\delta = 50$, are also shown.

provides a convenient model, whereby the R_δ value is about 0.7 without betraying any clear trend with δ. Larger mesoscale domains will need to be studied in the future to uncover such a trend. It follows that one can take $R_\delta = 0$ and deal only with scale dependence in $\sigma_{u\delta}$ in (2.39), plus the scatter about this mean value, when setting up a stochastic model of yield surfaces. The model would describe the ensemble of yield surfaces $\mathcal{P}_\delta = \{P_\delta(\omega); \omega \in \Omega\}$, where $\mathcal{P}_\delta$ is of an elliptical shell shape. The shell converges to an infinitesimal thickness in the $\delta \to \infty$ limit, but bifurcates into two distinct HM ellipses in the $\delta \to 0$ limit.

Figure 2.13 also displays the $\langle \overline{\mathbf{d}} \rangle$ vectors, ensemble averaged for each one of four yield surfaces here (at $\delta = 10$ and 50 under both kinematic and traction conditions). Noteworthy is the departure of apparent (mesoscale) flow rule, for each case, from the normality (compare with Figure 2.2). Figure 2.14 presents this departure more clearly in terms of the difference $\pi/2 - \alpha_{\overline{\mathbf{d}}}$, where $\alpha_{\overline{\mathbf{d}}}$ is the actual angle the $\overline{\mathbf{d}}$ vector makes to the yield surface. It is interesting that the behaviors of four curves are qualitatively similar although the curve corresponding to $\delta = 50$ under traction condition making a dip below $\pi/2 - \alpha_{\overline{\mathbf{d}}} = 0$ level must likely indicate that the ensemble of 20 specimens sampled here (by the Monte Carlo method) has been too small to get a very reliable result.

2.5 Conclusions

Answers to five key questions

Let us now summarize all the results as answers to the five questions stated at the beginning of the paper:

Answer to Q1: The mesoscale yield condition is shown, from extremum principles combined with material ergodicity and stationarity, to bound from above (and below) the macroscopic homogenized response when kinematic (respectively, traction) boundary condition is applied. Furthermore, the larger the mesoscale, the tighter are the bounds, albeit the kinematic condition displays a much stronger scale-dependence than the traction one.

Answer to Q2: Neither in plane deformation rate nor in plane stress is the flow rule normal for any given realization of the random medium.

Answer to Q3: In the case of plane deformation rate, the flow rule is normal upon ensemble averaging. This property is not recovered in the plane stress case.

Answer to Q4: In the case of plane deformation rate the yield surface, for any given mesoscale and realization of the random medium, consists of two parallel lines. In the plane stress case, the yield surface is ellipse-shaped, albeit, for both boundary conditions (kinematic and traction), of a different aspect ratio than that of the HM material. It is not yet clear what scale is necessary to approximately attain the classical HM material for the RVE. This will likely require much larger domains studied by computational models.

Answer to Q5: The scatter of yield loci is decreasing with mesoscale increasing under either type of boundary conditions.

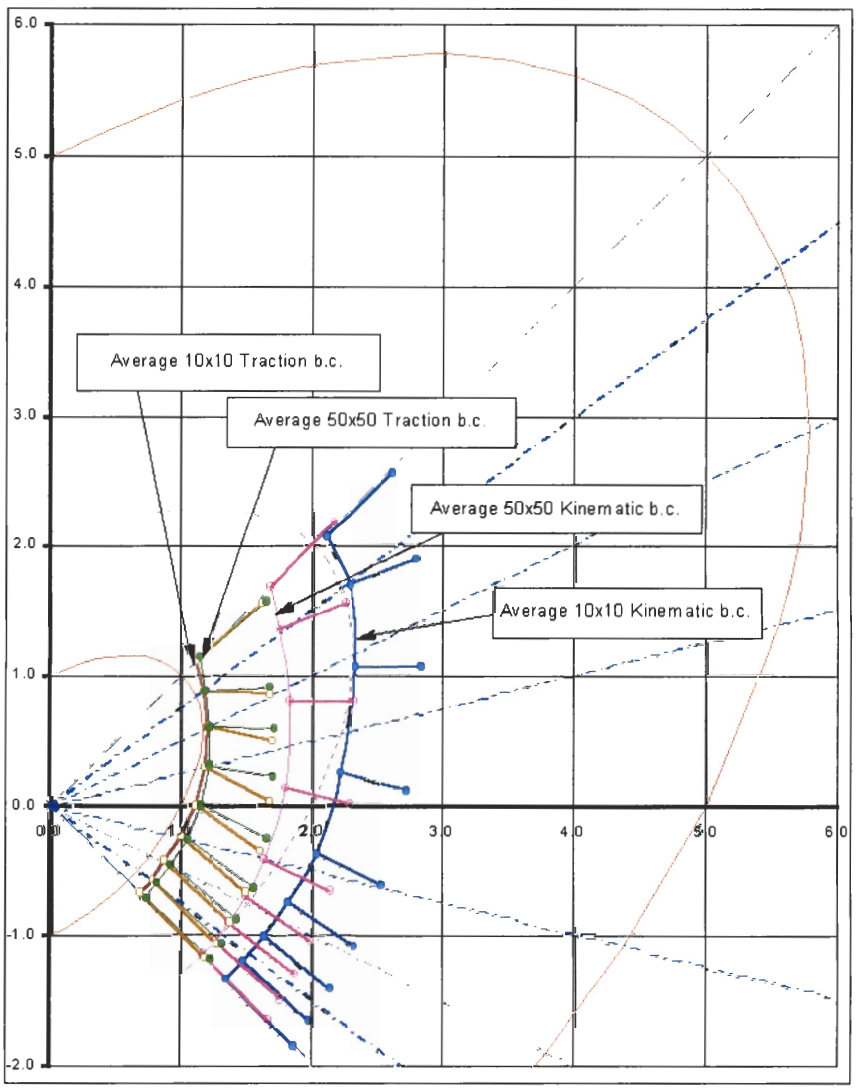


Figure 2.13: A close-up from Fig. 2.11 of the ensemble view of apparent yield surfaces in plane stress, focusing on the first quarter in the space of principal stresses, on mesoscales $\delta = 10$ and 50. The vectors, shown for ensemble average yield surfaces at $\delta = 10$ and 50 under kinematic and traction conditions, display the departure from normality.

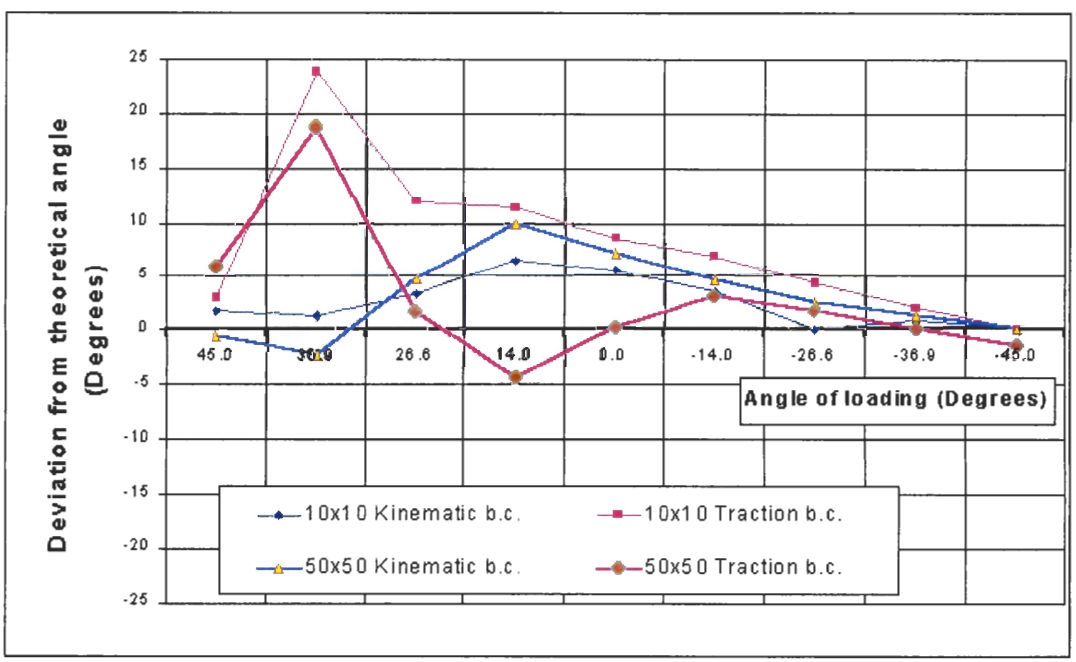


Figure 2.14: The departure from normality displayed in the previous figure is now shown in terms of the difference $\pi/2 - \alpha_{\overline{\mathbf{d}}}$, where $\alpha_{\overline{\mathbf{d}}}$ is the actual angle the $\overline{\mathbf{d}}$ vector makes to the yield surface.

All the numerical results of Section 2.4 have, strictly speaking, been obtained for one particular case of volume fraction of a specific random material – a planar, two-phase chessboard at 50% – and it still remains an open issue to see to what extent the particular behaviors found here carry over to other models. On the other hand, given the fact that the qualitative hierarchies of bounds of Section 2.3 should carry over to general rigid-perfectly plastic and rigid-hardening plastic heterogeneous materials.

Aspects of mesh refinement

To study the effect of increased mesh resolution, some of the realizations on mesoscale $\delta = 10$ were solved for their yield surface apparent response using a grid of 50×50 instead of 10×10 elements. In practice, this can be thought as particular or special realizations of mesoscale $\delta = 50$, where the hard phase appears as in squared clusters. This is illustrated in Figure 2.15. The trend of the resulting yield surface with respect to mesh resolution is as follows:

Plane Stress As the mesh resolution increases under traction boundary conditions, the apparent yield surface of each realization, as well as the ensemble average, moves in the space of principal stresses towards the soft phase's yield surface and normality tends to be recovered. However, as the mesh resolution increases under kinematic boundary conditions, the apparent yield surface of each realization moves towards the corresponding mesoscale's yield surface ($\delta = 50$ in this example) and the departure from normality is kept. The same effect can be observed for the ensemble average.

Plane Deformation Rate As the mesh resolution increases under traction boundary conditions, the yield limit of each realization, as well as the ensemble average, moves in the space of principal stresses towards the soft phase's yield limit. For each single realization, there is almost no scatter of the apparent yield limit and the normality of the flow rule tends to be recovered. On the other hand, as the mesh resolution increases under kinematic boundary conditions, the apparent yield surface of each realization moves towards the equivalent mesoscale's yield surface ($\delta = 50$ in this case). The same effect is obtained for the ensemble average. As in the case of a coarse mesh, the vectors of deformation rate satisfying normality of flow rule hold in the ensemble average, but not per single realization. Also, scatter of yield points around the ensemble average is the same as with the coarse mesh.

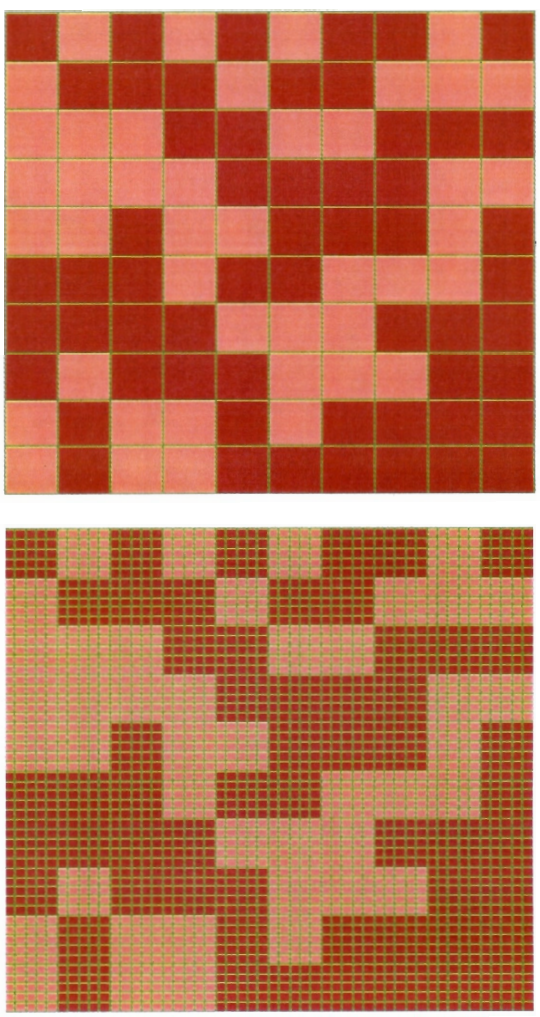


Figure 2.15: A realization on mesoscale $\delta = 10$ can be resolved using a grid of 50×50 (bottom) instead of 10×10 (top) elements.

Chapter 3

Inelastic and Nonlinear Model for Paper

3.1 Background

The objective of this chapter is to develop a continuum mechanics model of paper's biaxial tensile response accounting for:

- inelastic and nonlinear behavior beyond the elastic range, in particular:

- plastic limit (yield condition) and flow rule;
- hardening beyond the plastic limit;

- viscous (strain rate-dependence) effects: the faster is the loading, the stiffer is the response;

- isotropy (handsheets) and orthotropy (machine-made paper);

- random formation effects.

Let us first note that the latter of these objectives, random effects, is treated in a much simpler (but far from trivial) setting of Huber-Mises plasticity (see Chapter 2). That chapter presented a formulation of basic concepts and a homogenization method for 'coupled scale and boundary conditions effects' involved in mechanics of paper with due account of formation. Therefore, the present chapter focuses on the first three objectives to develop the functional forms of the constitutive behaviors without explicitly considering the spatially random nature of stress, strain, and displacements fields, as well as associated energy fields.

As the framework for constitutive behaviors of paper *thermomechanics with internal variables* (T.I.V.) is taken, this choice allowing us to make a systematic development of elastic/inelastic/nonlinear responses of paper consistent with the laws of continuum mechanics *and* thermodynamics of irreversible processes (Maugin, 1992; 1999). Note that, in contradistinction to T.I.V., *rational thermodynamics* and its so-called *extended* version do not appear to be well suited to plastic phenomena. Finally,

T.I.V. can be generalized to randomly heterogeneous media as already partly shown in Ostoja-Starzewski (2002) and thus holds promise for handling random formation effects in paper.

3.2 Thermomechanics with internal variables T.I.V.

3.2.1 Basic concepts

This section follows the version of T.I.V. due to Ziegler (1983), restricting it to infinitesimal strains in the plane of paper where $x_1(x_2)$ denotes MD (CD) as usual. Material response is now described by the *free energy* Ψ and the *dissipation function* Φ per unit volume

$$\Psi = \frac{1}{2}\boldsymbol{\sigma} \cdot \boldsymbol{\varepsilon}^e \qquad \Phi = \Phi_{th} + \Phi_{intr} \geq 0 \tag{3.1}$$

Here $\boldsymbol{\sigma}$ is Cauchy stress and $\boldsymbol{\varepsilon}^e$ is elastic strain (or a vector thereof). Also, the Clausius-Duhem inequality $(3.1)_2$ expresses the second law of thermodynamics with Φ_{th} being the *thermal dissipation* and Φ_{intr} the *intrinsic dissipation*

$$\Phi_{th} \equiv -\mathbf{q} \cdot \boldsymbol{\nabla} T/T \qquad \Phi_{intr} \equiv \mathbf{Y} \cdot \mathbf{v} \tag{3.2}$$

Here, $\mathbf{q}$ is heat flux and T is temperature. Evidently, Φ_{intr} is a scalar product of the *dissipative force* $\mathbf{Y}$ (possibly including a dissipative Cauchy stress) with the velocity $\mathbf{v}$ (vector of strain rate $\dot{\boldsymbol{\varepsilon}}$ and of rate $\dot{\boldsymbol{\alpha}}$ of the *internal variable* $\boldsymbol{\alpha}$). Given the absence of large strains in paper mechanics, we work with $\dot{\boldsymbol{\varepsilon}} = \mathbf{d}$, the latter being the deformation rate. To better illustrate the concept of internal variables, let us consider a very simple one-dimensional model (Ziegler, 1983): In Figure 3.1, the force acting in the spring is a function of its elongation $\overline{\boldsymbol{\alpha}}$, and the force in the dashpot depends on its rate of elongation $\dot{\boldsymbol{\alpha}}$. Neglecting inertial forces, the forces in either element, spring and dashpot, are then equal to $\boldsymbol{\sigma}$. The only external kinematical parameter is the elongation $\boldsymbol{\varepsilon}$ of the entire system, and it is clear that the force $\boldsymbol{\sigma}$ is not determined by $\boldsymbol{\varepsilon}$ alone. In deed, if $\boldsymbol{\varepsilon}$ is kept constant, $\boldsymbol{\sigma}$ tends to zero while the dashpot allows the spring to return to its natural length. It is intuitively obvious that the force $\boldsymbol{\sigma}$ at time t is determined by the history of the elongation $\boldsymbol{\varepsilon}$, i.e., if the function $\boldsymbol{\varepsilon}(\tau)$ is known for all times between $\tau = -\infty$ and $\tau = t$. Thus, $\boldsymbol{\sigma}(t)$ may be considered a functional, i.e., as a function of the function $\varepsilon(\tau)$. On the other hand, the value $\boldsymbol{\sigma}$ at time t is also known if, beside $\boldsymbol{\varepsilon}$, either $\boldsymbol{\alpha}$ or $\overline{\boldsymbol{\alpha}}$ are given at time t. Since $\boldsymbol{\varepsilon} = \boldsymbol{\alpha} + \overline{\boldsymbol{\alpha}}$, we need only one of the two quantities, and it is referred to as an internal variable.

With Φ being the total rate of entropy production, we make a very common assumption of separation of its two contributions

$$\Phi_{th} \geq 0 \qquad \Phi_{intr} \geq 0 \tag{3.3}$$

Henceforth Φ_{th} shall be dropped as being of negligible influence for problems at hand, and $\Phi = \Phi_{intr}$ will be used. Indeed, constitutive laws are formulated according to

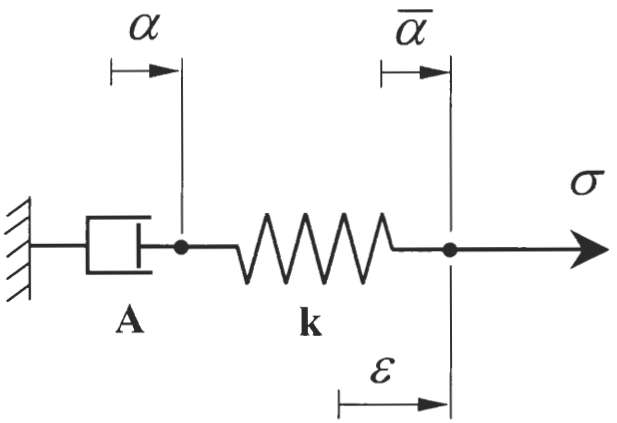


Figure 3.1: Spring and dashpot to illustrate the concept of internal variables.

the ideas of thermodynamic orthogonality (Ziegler, 1983; Ziegler and Wehrli, 1987; Collins and Houlsby, 1997): thus, the *quasi-conservative* ($\boldsymbol{\sigma}^{(q)}$) and *dissipative* ($\boldsymbol{\sigma}^{(d)}$) *stresses* are

$$\boldsymbol{\sigma}^{(q)} = \frac{\partial \Psi}{\partial \boldsymbol{\varepsilon}} \qquad \boldsymbol{\sigma}^{(d)} = \nu \frac{\partial \Phi}{\partial \dot{\boldsymbol{\varepsilon}}} \tag{3.4}$$

whereas the *internal quasi-conservative* ($\boldsymbol{\beta}^{(q)}$) and *internal dissipative* ($\boldsymbol{\beta}^{(d)}$) *stresses* are

$$\boldsymbol{\beta}^{(q)} = \frac{\partial \Psi}{\partial \boldsymbol{\alpha}} \qquad \boldsymbol{\beta}^{(d)} = \nu \frac{\partial \Phi}{\partial \dot{\boldsymbol{\alpha}}} \tag{3.5}$$

in which the coefficient ν is determined from

$$\nu = \Phi \left(\frac{\partial \Phi}{\partial \mathbf{v}} \cdot \mathbf{v} \right)^{-1} \tag{3.6}$$

Note here that the total stress $\boldsymbol{\sigma}$ is

$$\boldsymbol{\sigma} = \boldsymbol{\sigma}^{(q)} + \boldsymbol{\sigma}^{(d)} \tag{3.7}$$

while the internal stresses must satisfy

$$\boldsymbol{\beta}^{(q)} = -\boldsymbol{\beta}^{(d)} \tag{3.8}$$

In the following, a sequence of thermomechanics models are developed, all of them in systematic correspondence to the four goals listed above. It is tacitly understood that, while unloading is permitted, no negative principal stresses are allowed as they would in reality involve an out-of-plane buckling behavior. A separate study is needed to construct a continuum model involving buckling.

3.2.2 Inelastic and nonlinear behavior beyond the elastic range

The presence of plastic limit and plastic hardening of linear type can be obtained by taking Ψ quadratic in strains and Φ homogeneous of degree one in velocities ($p = 1$)

$$\Psi = \frac{1}{2}(\boldsymbol{\varepsilon} - \boldsymbol{\alpha}) \cdot \mathbf{C} \cdot (\boldsymbol{\varepsilon} - \boldsymbol{\alpha}) + \frac{1}{2}\boldsymbol{\alpha} \cdot \mathbf{H} \cdot \boldsymbol{\alpha} \qquad \Phi(p\,\dot{\boldsymbol{\alpha}}) = p\Phi(\dot{\boldsymbol{\alpha}}). \tag{3.9}$$

Here, a linear character of the initial elastic response ($\mathbf{C}$) is assumed as well as that of the hardening response ($\mathbf{H}$). Evidently, $\boldsymbol{\alpha}$ is the plastic strain in the model. An example of Φ is given by the Huber-Mises material: $k(2\,\dot{\boldsymbol{\alpha}}_{(2)})^{1/2}$, where $\dot{\boldsymbol{\alpha}}_{(2)}$ denotes the second basic invariant of $\dot{\boldsymbol{\alpha}}$ and k is the plastic limit in shear. For the two-dimensional paper we need a form more in the vein of Tresca

$$\Phi = k_{11}\,\dot{\alpha}_{11} + k_{22}\,\dot{\alpha}_{22} + k_{12}\,\dot{\alpha}_{12} \tag{3.10}$$

The first and second terms on the right-hand side are motivated by uniaxial and biaxial tension tests (k_{11} and k_{22} being respective yield limits), while the third term (k_{12} being yield limit in shear) is suggested by an analogy thereto. Of course an experimental test of plastic response of paper under shear and thus, a precise determination of the k_{12} value, is very unwieldy. At this stage we can postulate $k_{12} = k_{11}/2$, i.e., shear response is assessed via uniaxial test in MD.

According to the basic formulas of thermomechanics given above, we find

$$\boldsymbol{\sigma} = \mathbf{C} \cdot (\boldsymbol{\varepsilon} - \boldsymbol{\alpha}) \qquad \text{with} \qquad \boldsymbol{\alpha} = (\mathbf{H} + \mathbf{C})^{-1} \cdot (\mathbf{C} \cdot \boldsymbol{\varepsilon} - \mathbf{k}) \tag{3.11}$$

with $\mathbf{k}$ being written as though it were a tensor, although it is only a matrix, with $k_{12} = k_{21}$. The behavior of this model is represented graphically in Figure 3.2(a) and (c). The special case of elastic-perfectly plastic response obtains when $\mathbf{H} \to \mathbf{0}$; this, however, is hardly relevant for paper. Also note that, in general, the incremental response beyond the plastic limit is

$$d\boldsymbol{\sigma} = \left[\mathbf{I} - \mathbf{C}\cdot(\mathbf{H} + \mathbf{C})^{-1}\right] \cdot \mathbf{C} \cdot d\boldsymbol{\varepsilon} \equiv \mathbf{C}^T \cdot d\boldsymbol{\varepsilon} \tag{3.12}$$

Figure 3.2(b) presents the split of total energy into the recoverable energy W^e, the plastically dissipated energy W^p, and the energy stored by modification of the internal structure W^m. While the latter requires some sort of a spatial, microstructural model (i.e., micromechanics), we may readily introduce nonlinearity by replacing in $(3.9)_1$ the contribution $\frac{1}{2}\boldsymbol{\alpha} \cdot \mathbf{H} \cdot \boldsymbol{\alpha}$ of the phenomenological, linear spring $\mathbf{H}$ by either one of the following models:

(a) Series expansion (Brugger, 1964)

$$\Psi_H = \frac{1}{2!}\mathbf{H}_2 \cdot \boldsymbol{\alpha}^2 + \frac{1}{3!}\mathbf{H}_3 \cdot \boldsymbol{\alpha}^3 + \ldots \qquad \text{with} \qquad \boldsymbol{\sigma} = \mathbf{H}_2 \cdot \boldsymbol{\alpha} + \frac{1}{2!}\mathbf{H}_3 \cdot \boldsymbol{\alpha}^2 + \ldots, \tag{3.13}$$

(b) Single effective strain variable model

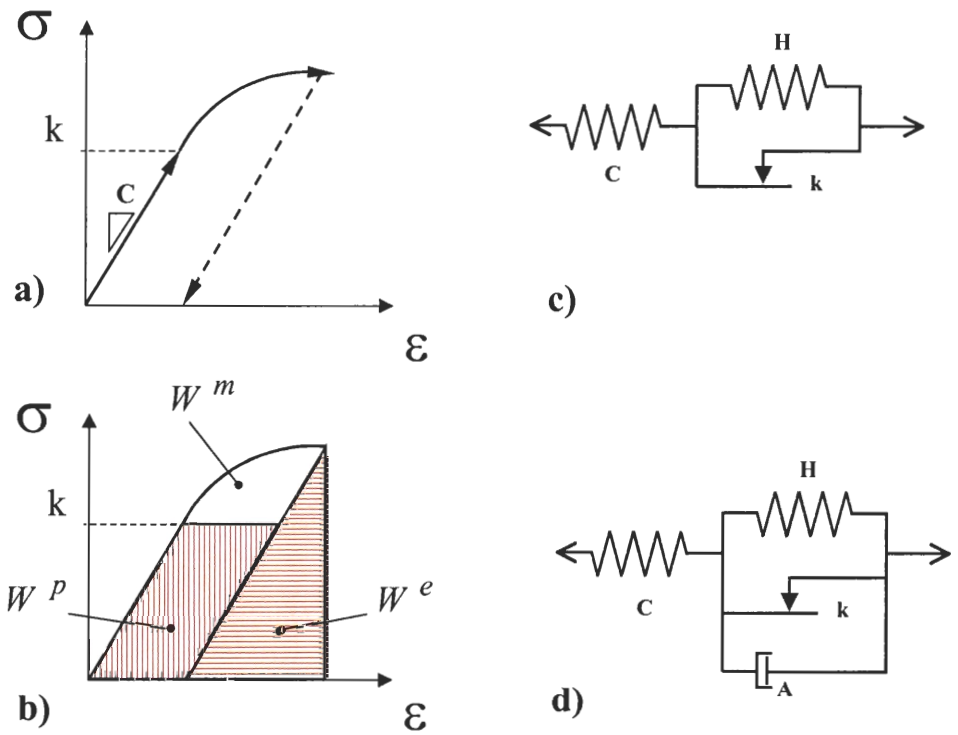


Figure 3.2: (a) Stress-strain curve of the elastic-plastic model.; (b) energies involved in the inelastic response of paper; (c) a rheological model of elastic plastic response; (d) a rheological model of visco-elastic plastic response.

$$\Psi_H = \frac{\nu_{21} E_1}{2(1 - \nu_{12}\nu_{21})} e, \tag{3.14}$$

where

$$e = \frac{\varepsilon_{11}^2}{\nu_{21}} + \frac{\varepsilon_{22}^2}{\nu_{12}} + 2\varepsilon_{11}\varepsilon_{22} + C\varepsilon_{12}^2 \qquad \text{with} \qquad C = \frac{4(1 - \nu_{12}\nu_{21})}{\nu_{12} E_1} G_{12} \tag{3.15}$$

is a positive definite effective strain measure. Note that Johnson and Urbanik (1984) and Suhling et al. (1989) adopted this model in the entire strain range of paper, thus denying possibility of any plastic (permanent) strains (see Section 1.1.4). By contrast, our composition of Ψ_C with Ψ_H admits plasticity. This topic is continued in Section 4.3.

3.2.3 Yield condition and flow rule

We are dealing here with the dissipation function $\Phi(\dot{\boldsymbol{\alpha}})$. By virtue of $\boldsymbol{\beta}^{(d)} = \nu \partial \Phi / \partial \dot{\boldsymbol{\alpha}}$ we can define a dual function in which $\dot{\boldsymbol{\alpha}}$ is replaced by $\boldsymbol{\beta}^{(d)}$. Since Φ is

homogeneous of degree one in $\dot{\boldsymbol{\alpha}}$, $Z = \boldsymbol{\Phi}(\dot{\boldsymbol{\alpha}})$ represents a cone in a (3+1) dimensional $(\dot{\boldsymbol{\alpha}}, Z)$-space and the Legendre transformation is singular, e.g., Collins and Houlsby (1997). Since $\Phi = \dot{\boldsymbol{\alpha}} \cdot \partial\Phi/\partial\, \dot{\boldsymbol{\alpha}}$ by the Euler's theorem, the dual function is hence identically zero

$$f(\boldsymbol{\beta}^{(d)}) = 0 \tag{3.16}$$

and the nonunique inverse relation is

$$\dot{\boldsymbol{\alpha}} = \lambda \frac{\partial f}{\partial \boldsymbol{\beta}^{(d)}} \tag{3.17}$$

where λ is an undetermined multiplier. Clearly, these are the familiar yield condition and flow rule for rate-independent plastic materials, respectively, albeit formulated in the space of internal stresses and not true stresses. Given (3.10), the yield function $f(\boldsymbol{\beta}^{(d)})$ may be written in terms of three conditions

$$\beta^{(d)}_{11,\max} = k_{11} \qquad \beta^{(d)}_{22,\max} = k_{22} \qquad \beta^{(d)}_{12,\max} = k_{12} \tag{3.18}$$

It is seen from (3.18) that plastic normality holds in the space of internal dissipative stresses, but not necessarily true stresses. Note: $\boldsymbol{\beta}^{(d)}$ is sometimes called a *generalized stress.*

3.2.4 Viscous (strain rate-dependence) effects

There are now two basic ways to introduce viscosity: (i) by either placing a dashpot (of property) **A** in parallel with the **H**-spring and **k**-plasticity, or (ii) by placing it in parallel with the entire system (see Figure 3.2(d)). For simplicity, we assume a linear dashpot. In the first case, we have

$$\Psi = \frac{1}{2}(\boldsymbol{\varepsilon} - \boldsymbol{\alpha}) \cdot \mathbf{C} \cdot (\boldsymbol{\varepsilon} - \boldsymbol{\alpha}) + \frac{1}{2}\boldsymbol{\alpha} \cdot \mathbf{H} \cdot \boldsymbol{\alpha} \qquad \Phi = \Phi_k\left(\dot{\boldsymbol{\alpha}}\right) + \dot{\boldsymbol{\alpha}} \cdot \mathbf{A} \cdot \dot{\boldsymbol{\alpha}}, \tag{3.19}$$

with Φ_k being given by (3.10), so that

$$\boldsymbol{\sigma} = \mathbf{C} \cdot (\boldsymbol{\varepsilon} - \boldsymbol{\alpha}) \qquad \text{with} \qquad (\mathbf{H} + \mathbf{C}) \cdot \boldsymbol{\alpha} + \dot{\boldsymbol{\alpha}} \cdot \mathbf{A} = \mathbf{C} \cdot \boldsymbol{\varepsilon} - k \tag{3.20}$$

Note that by removing the **H**-spring element, we obtain the Bingham viscoplasticity model. One could also contemplate placing the dashpot in series with the **H**-spring, so as to arrive at the Schwedoff viscoplasticity model. The latter would lead to nonrecoverable strains because of the Maxwell-type element.

In the case (ii) we have

$$\Psi = \frac{1}{2}(\boldsymbol{\varepsilon} - \boldsymbol{\alpha}) \cdot \mathbf{C} \cdot (\boldsymbol{\varepsilon} - \boldsymbol{\alpha}) + \frac{1}{2}\boldsymbol{\alpha} \cdot \mathbf{H} \cdot \boldsymbol{\alpha} \qquad \Phi = \Phi_k + \mathbf{A} \cdot \dot{\boldsymbol{\varepsilon}}^2 \tag{3.21}$$

with Φ_k being given again by (3.10), so that

$$\boldsymbol{\sigma} = \mathbf{C} \cdot \boldsymbol{\varepsilon} - (\mathbf{H} + \mathbf{C})^{-1} \cdot \mathbf{C} \cdot (\mathbf{C} \cdot \boldsymbol{\varepsilon} - \mathbf{k}) + \mathbf{A} \cdot \dot{\boldsymbol{\varepsilon}} \tag{3.22}$$

To sum up, both models result in a stiffening of response with increasing strain rate, an effect that is characteristic of paper. However, model (i) is more difficult to solve analytically because of the implicit nature of $(3.9)_2$. On the other hand, model (ii) is simpler to deal with, but lacks the impact response.

3.2.5 Isotropy (handsheets) versus orthotropy (machine-made paper) of response

Isotropy is obtained by:
- taking elasticities $\mathbf{C}$ and $\mathbf{H}$ to be isotropic,
- reducing plastic dissipation to the form $\Phi = k\,\dot{\alpha}_{11} + k\,\dot{\alpha}_{22} + k_{12}\,\dot{\alpha}_{12}$,
- taking viscosity $\mathbf{A}$ to be isotropic.

Clearly, orthotropy can be set up via appropriate modifications.

3.2.6 Random formation effects

When $\mathbf{v}$ in the given problem does not involve internal variables, we have field variational principles of mechanics such as in the (thermo)elasticity, viscoelasticity, or rigid plasticity to ensure the true extremum character of solution fields and their volume averages under given boundary conditions; see the review of Ostoja-Starzewski (2001) and references therein. A extension of these methods to damage mechanics of randomly heterogeneous elastic-brittle solids is given in Ostoja-Starzewski (2002). However, when the rates of internal variables, denoted by a vector $\dot{\boldsymbol{\alpha}}$, are present within $\mathbf{v}$ (with appropriate conjugate forces showing up in the $\mathbf{Y}$ vector) in a mesoscale thermomechanics model, a generalization of variational principles is more complex.

Below, following Jiang et al. (2001) and Ostoja-Starzewski (2000), we outline a methodology for scale-dependent homogenization of physically nonlinear elastic (equivalent in loading to elastic-hardening plastic) random material in terms of the tangent moduli $\mathbf{C}^T$, and we have seen above that the tangent moduli, stiffness $\mathbf{C}^T$ or, equivalently, compliance $\mathbf{S}^T$, describe the incremental response of paper. This is the relation of the body $B_\delta(\omega)$ on any finite scale $\delta = L/d$ (L being specimen size and d being floc size) that connect stress increments with strain increments applied to it

$$d\boldsymbol{\sigma} = \mathbf{C}_\delta^T(\omega) \cdot d\boldsymbol{\varepsilon} \quad d\boldsymbol{\varepsilon} = \mathbf{S}_\delta^T(\omega) \cdot d\boldsymbol{\sigma}. \tag{3.23}$$

Clearly, the tensor $\mathbf{C}_\delta^T(\omega)$ is random, with $\omega \in \Omega$ indicating statistical scatter; a probability distribution $P_{\mathbf{C}_\delta^T}(\omega)$ describes this scatter. Now, the larger the body domain the weaker the associated random scatter in $\mathbf{C}_\delta^T(\omega)$, and it goes down to zero as $\delta \to \infty$ in the mascroscopic RVE limit.

The Hill condition and its implication for the type of admissible boundary conditions for incremental response is

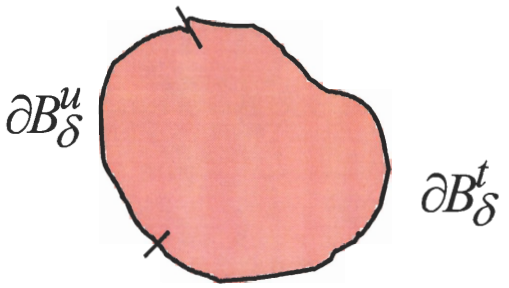


Figure 3.3: Surface of body B, which is made up of the part controlled by displacements, ∂B^u_δ, and another one controlled by tractions, ∂B^t_δ

$$\overline{d\boldsymbol{\sigma}\cdot d\boldsymbol{\varepsilon}} = d\overline{\boldsymbol{\sigma}}\cdot d\overline{\boldsymbol{\varepsilon}} \Longleftrightarrow \int_{\partial B_\delta} (d\mathbf{t} - d\overline{\boldsymbol{\sigma}}\cdot\mathbf{n})\cdot(d\mathbf{u} - d\overline{\boldsymbol{\varepsilon}}\cdot\mathbf{x})dS = 0, \tag{3.24}$$

where $d\overline{\boldsymbol{\sigma}} = d\boldsymbol{\sigma}^0$ and $d\overline{\boldsymbol{\varepsilon}} = d\boldsymbol{\varepsilon}^0$.

Next, we recall (e.g., Hill, 1950) two extremum principles: one for kinematically admissible fields

$$\int_{\partial B^t_\delta} d\mathbf{t}\cdot d\widetilde{\mathbf{u}}dS - \frac{1}{2}\int_{B_\delta} d\widetilde{\boldsymbol{\sigma}}\cdot d\widetilde{\boldsymbol{\varepsilon}}dV \leq \int_{\partial B^t_\delta} d\mathbf{t}\cdot d\mathbf{u}dS - \frac{1}{2}\int_{B_\delta} d\boldsymbol{\sigma}\cdot d\boldsymbol{\varepsilon}dV, \tag{3.25}$$

and another for statically admissible fields

$$\frac{1}{2}\int_{B_\delta} d\boldsymbol{\sigma}\cdot d\boldsymbol{\varepsilon}dV - \int_{\partial B^u_\delta} d\mathbf{t}\cdot d\mathbf{u}dS \leq \frac{1}{2}\int_{B_\delta} d\widetilde{\boldsymbol{\sigma}}\cdot d\widetilde{\boldsymbol{\varepsilon}}dV - \int_{\partial B^u_\delta} d\widetilde{\mathbf{t}}\cdot d\mathbf{u}dS, \tag{3.26}$$

where ∂B_δ is made up of the part controlled by displacements, ∂B^u_δ, and another one controlled by tractions, ∂B^t_δ (see Figure 3.3).

From this, we find

$$\mathbf{C}^{Td}_\delta \leq \mathbf{C}^{Td}_{\delta'}, \quad \mathbf{S}^{Tt}_\delta \leq \mathbf{S}^{Tt}_{\delta'}, \quad \forall\delta' = \delta/2. \tag{3.27}$$

Upon ensemble averaging, involving ergodicity and statistical homogeneity of microstructure, and applying this to ever-larger windows ad infinitum we get a hierarchy of bounds on the macroscopically effective tangent modulus $\mathbf{C}^T_\infty = (\mathbf{S}^T_\infty)^{-1}$

$$\left\langle \mathbf{S}^{Tt}_1 \right\rangle^{-1} \leq \ldots \leq \left\langle \mathbf{S}^{Tt}_{\delta'} \right\rangle^{-1} \leq \left\langle \mathbf{S}^{Tt}_\delta \right\rangle^{-1} \leq \ldots \leq \mathbf{C}^T_\infty \leq \ldots \leq \left\langle \mathbf{C}^{Td}_\delta \right\rangle \leq \left\langle \mathbf{C}^{Td}_{\delta'} \right\rangle \leq \ldots \leq \left\langle \mathbf{C}^{Td}_1 \right\rangle$$
$$\forall\delta' = \delta/2 \tag{3.28}$$

where $\left\langle \mathbf{S}^{Tt}_1 \right\rangle^{-1}$ and $\left\langle \mathbf{C}^{Td}_1 \right\rangle$ are recognized as the so-called Sachs (1928) and Taylor

(1938) bounds, respectively. A reference is made here to Suquet (1997) and Ponte Castañeda and Suquet (1998) for comprehensive reviews of effective properties (on infinite scales, RVE limit) of nonlinear composites. An application of this hierarchy of bounds is illustrated with an example in Chapter 4.

Chapter 4

Computer Modeling of Paper

4.1 Finite element model

As mentioned earlier, in the present model a paper sheet is represented in FLAC by rectangular elements within a grid. This grid can be adjusted to fit the shape of the paper specimen to be modeled. The element's response may follow a prescribed linear or nonlinear, elastic or inelastic, stress-strain constitutive law. In addition, each element can be assigned a different constitutive law via material parameters (Young's modulus, Poisson's ratio, etc.). In other words, it is possible to model the nonhomogeneous character of paper. Figure 4.1 illustrates schematically the application of this concept. Uniaxial or biaxial stress-strain tests on homogeneous and nonhomogeneous material samples are simulated with the finite element model. This allows obtaining stress fields under different boundary conditions, which can be compared among them to evaluate the influence of local property variability. Recall from Section 2.3 that there are three types of boundary conditions on the mesoscale: uniform kinematic, uniform traction, and uniform kinematic-traction.

To set-up the simulation model, it is necessary to start by choosing a window scale and mesoscale (Ostoja-Starzewski, 2001), δ, defined as:

$$\delta = \frac{L}{d} \tag{4.1}$$

In the case of paper, several window scales can be considered from the roll size down to the fiber network as illustrated in Figure 4.2. Since the interest of this exercise is to address the effect of paper's formation on its mechanical properties, it is appropriate to choose the value of window size L in (4.1) in the order of a few centimeters. On the other hand, d can represent paper's fiber floc size (see Figure 4.3), which varies typically between 3 and 6 mm depending on grade and furnish.

In the present simulation model, material properties are assigned to each element proportionally to local basis weight (paper's grammage). A grammage map resembling flocculated paper can either be simulated through a stochastic process or built from β-radiography measurements as can be seen in Figures 4.3 and 4.4, respectively.

One way of simulating flocculated paper through a stochastic process is with a Boolean model. This type of model has been explored and used by Deng and Dodson

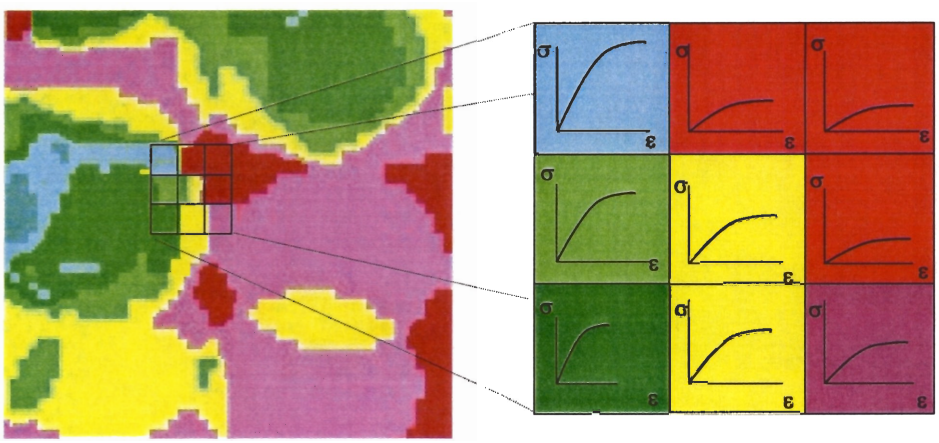


Figure 4.1: Assigning material properties and constitutive law to each element.

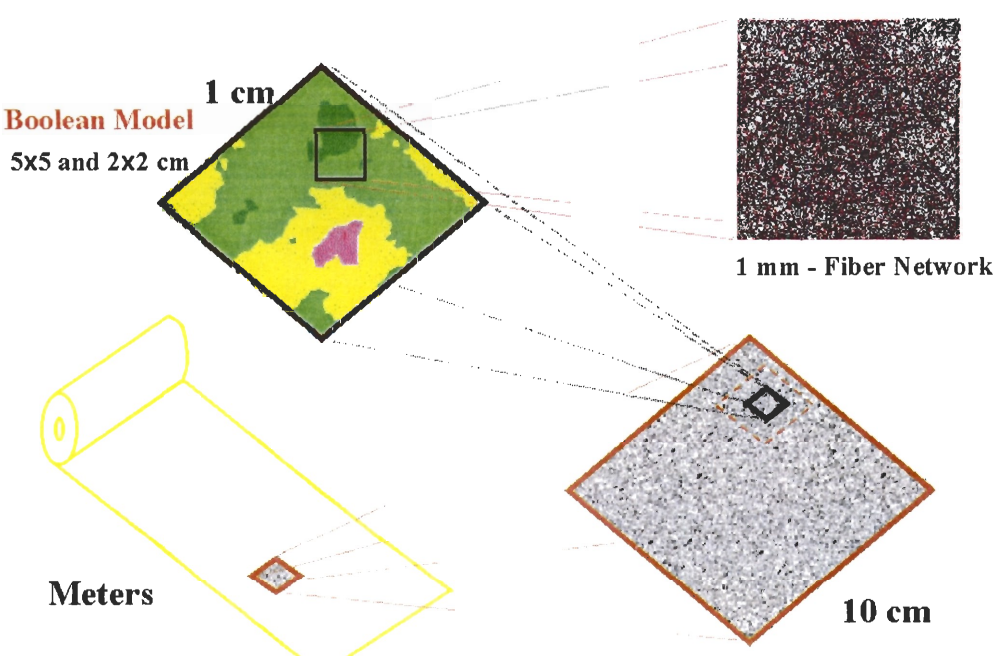


Figure 4.2: Selecting the scale for the simulation model.

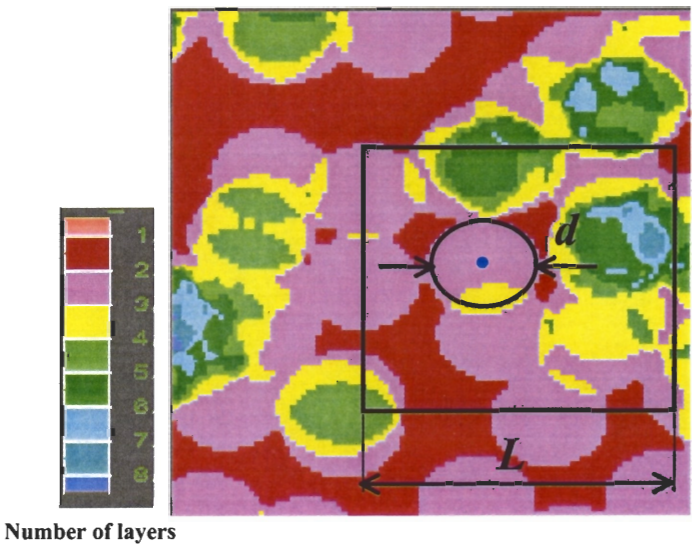


Figure 4.3: Generation of the Boolean model of paper formation.

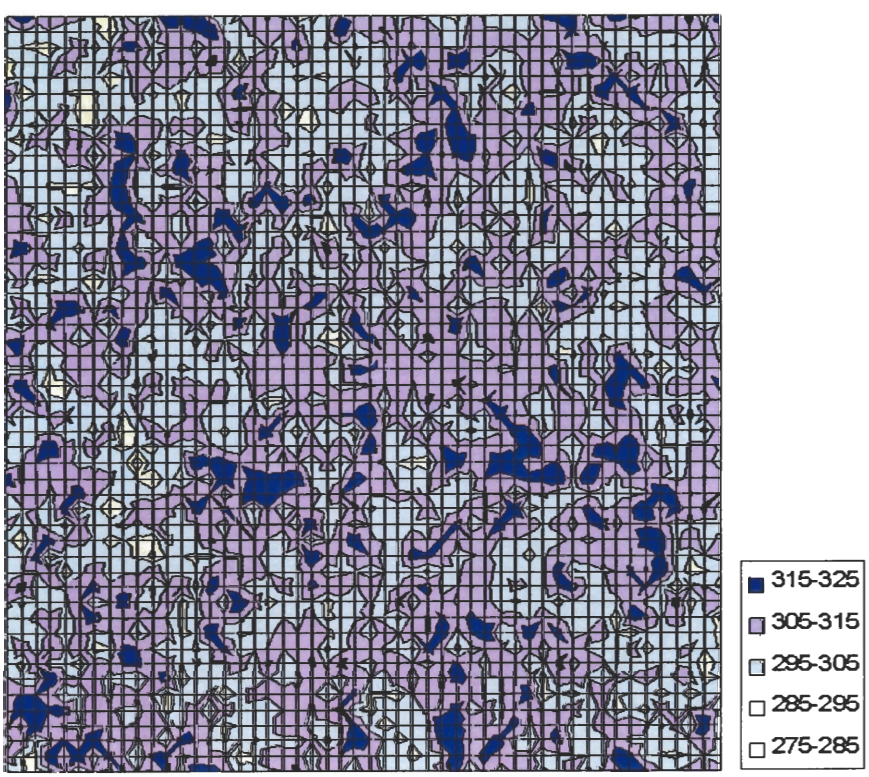


Figure 4.4: Paperboard's basis weight mapping from β-radiography (provided by Miranda Bliss of IPST).

(1994), and Farnood et al. (1997) to simulate paper, although the term "Boolean" has not been used; see Stoyan et al. (1987) and Jeulin (2001) for comprehensive presentations of Boolean and more general models. The algorithm adopted for the present illustration to simulate paper has the following two steps:

1. A random Poisson point field is generated in the x-y plane within a simulated window.

2. An ellipse of z-thickness t is "dropped" at each Poisson point.

After repeating these steps n-times, n ellipses are stacked at each location of the plane. Therefore, we obtain a sheet of variable thickness, $n \times t$, per unit area, which is equivalent to paper grammage. Figure 4.3 illustrates this simulation process where the dot represents the Poisson point of one ellipse. The ellipses' major axes coincide with the x-axis in this example, which means that there is a biased orientation, as in a machine-made paper with plane orthotropy. If, instead of ellipses, circles (disks) are dropped, the simulation represents a hand-made paper with plane isotropy.

4.2 Paper as a linear elastic-plastic isotropic material

Consider now a partition of window $B_\delta(\omega)$ into n^2 subwindows $B^s_{\delta'}$, then :

$$\delta' = \delta/n, \quad B_\delta(\omega) = \cup_{s=1}^{n^2} B_{\delta'}(\omega), \quad s = 1, 2, ..., n^2 \tag{4.2}$$

where δ is a nondimensional parameter representing the mesoscale window size. Figures 4.3 and 4.5 illustrate the meaning of the mesoscale δ, as it was defined in (4.1). Each $B_\delta(\omega)$ is called a realization of the random field (see Section 2.2). Figure 4.5 shows on the left a single realization of the Boolean model with $\delta = 10$. Physically, it represents a paper handsheet of 50×50 mm ($L = 50$ mm) with flocs of size $d = 5$ mm. On the right of Figure 4.5, there is a subset $B_4(\omega)$ of $B_{10}(\omega)$ with $\delta' = 4$, which resembles a 20×20 mm ($L' = 20$ mm) handsheet with $d = 5$ mm flocs. It is important to emphasize that $B_4(\omega)$ can be generated as an independent realization of the random field. In other words, $B_4(\omega)$ does not have to be necessarily a portion of other partition window. In the finite element model, each mesoscale is made of 1×1 mm, which means that $B_4(\omega)$ and $B_{10}(\omega)$ are modeled through meshes of 20×20 and 50×50 elements, respectively.

Continuing with the setup of the computer model, each finite element is assigned an isotropic elastic constitutive law as in (1.11). In a state of plane stress, this material law can also be expressed as:

$$\sigma_{11} = \frac{E}{(1-\nu^2)}\varepsilon_{11} + \frac{E\nu}{(1-\nu^2)}\varepsilon_{22} \tag{4.3}$$

$$\sigma_{22} = \frac{E\nu}{(1-\nu^2)}\varepsilon_{11} + \frac{E}{(1-\nu^2)}\varepsilon_{22} \tag{4.4}$$

$$\tau_{12} = G\gamma_{12} = 2G\varepsilon_{12} \tag{4.5}$$

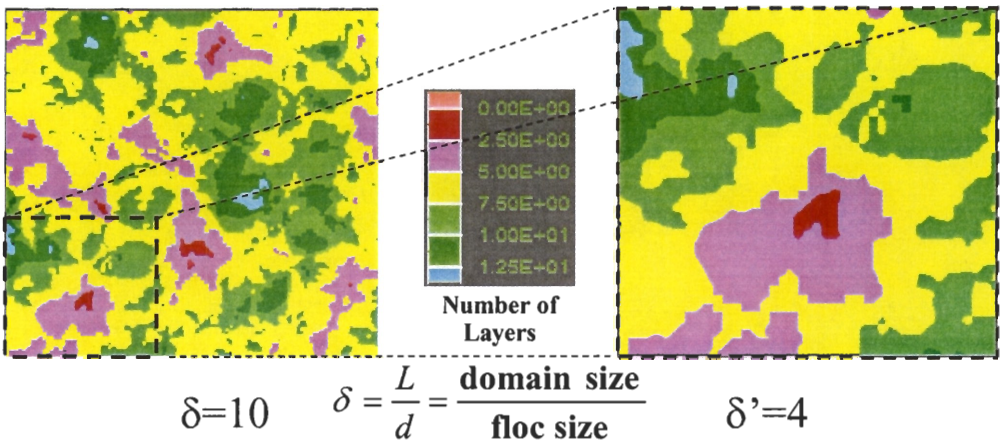


Figure 4.5: Illustration of mesoscale window

where E is the modulus of elasticity or Young's modulus, G is the shear modulus, and ν is the Poisson's ratio.

Each finite element is then assigned a stepwise elastic-plastic constitutive law, such as the shear stress-strain curve of Figure 4.6. The values of G and σ_{yield} in each element were taken in proportion to its basis weight. That is, their values were assigned according to the grammage distribution obtained from each realization of the random field. The tangent of each curve corresponds to G. After the stress yielding point σ_{yield}, the shear modulus G_2 is 10% of the initial slope G_1 of the stress-strain curve. The bulk modulus K is assumed to be constant. This process simulates a piece of paper as a spatially inhomogeneous material made of multiple phases. Each element is a phase having particular mechanical properties ranging from the softest to the hardest phase. G^{soft} and G^{hard} correspond to the lowest and highest grammage elements, respectively.

The objective of this computer model is to find bounds on the global response of the structure and the mesh dependency of these bounds. Particularly, we ask where the effective or apparent response of this composite will be in relation to its phases' distribution. All we can say by now, however, is that the apparent response is expected to be bounded by the responses of ideal materials made completely of the soft or hard phase. This means that:

$$G^{soft} \leq G^{eff} \leq G^{hard}$$

Figure 4.7 shows mesh deformations under uniform kinematic (2.23) and uniform traction boundary (2.24) conditions. In both cases there is a perturbation of the mesh since the material is nonhomogeneous. Should the material be perfectly homogeneous, all the mesh lines would be parallel and deform affinely under both kinematic or traction boundary conditions.

Figure 4.8 presents the shear stress field response under kinematic or traction

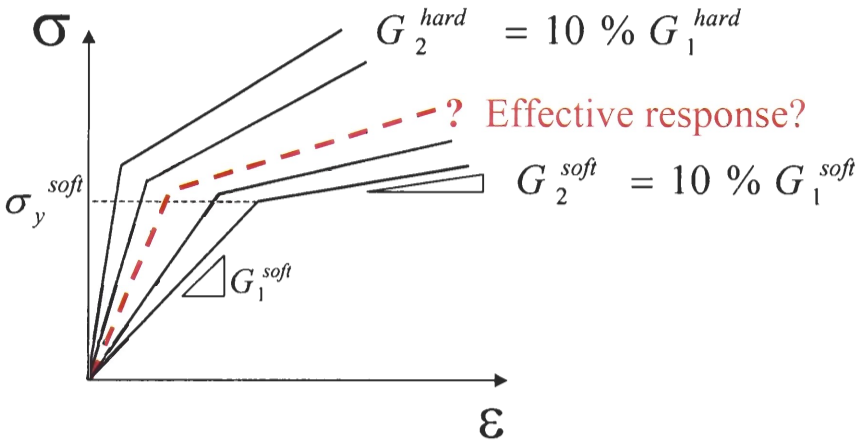


Figure 4.6: Stepwise-elastic-plastic isotropic model in plane stress.

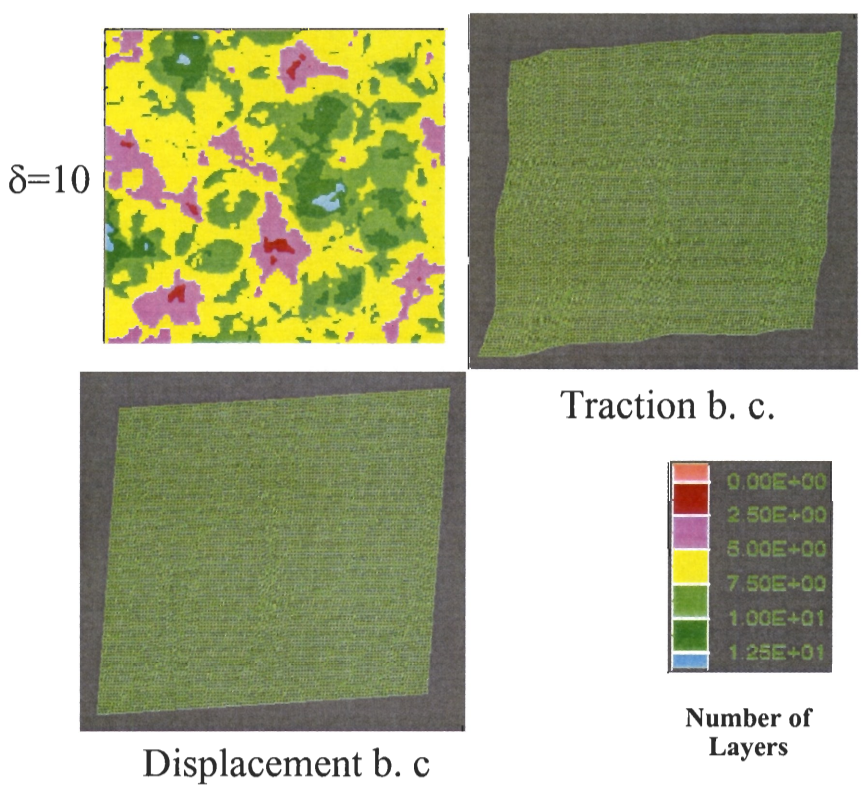


Figure 4.7: Material's response under pure shear loading. Mesoscale $\delta = 10$.

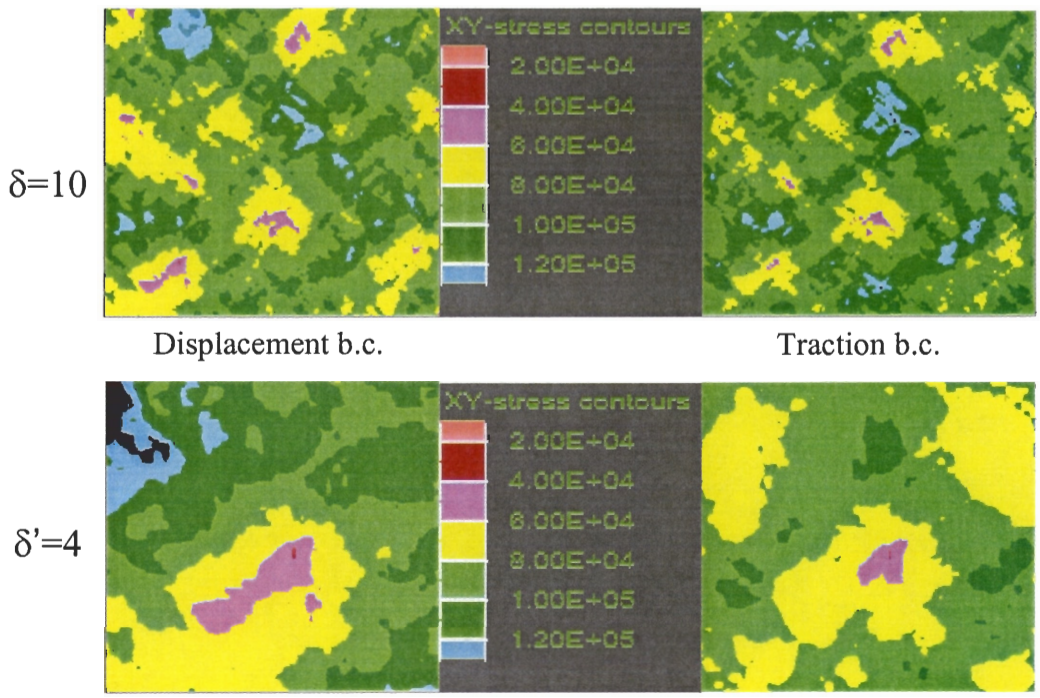


Figure 4.8: Comparison of responses according to boundary conditions and mesoscale.

boundary conditions for both mesoscales being considered in the present example. It can be seen by inspection of the shear stress field that $\delta' = 4$ under displacement b.c. presents the highest values of stress while $\delta' = 4$ under traction b.c. exhibits the lowest values in general. A better way of establishing this difference is through the analysis of the shear stress-strain curves shown in Figure 4.9.

The hierarchies of scale-dependent bounds on stored energy (based on extremum principles of elasticity) can be recalled now from Jiang et al. (2001). With a similar development to this of Section 2.3, it follows that:

$$w^{eff} = w(\varepsilon^0, \infty) \leq \langle w(\varepsilon^0, \delta) \rangle \leq w(\varepsilon^0, \delta') \leq w(\varepsilon^0, 1) \equiv w^V \quad 1 < \delta' < \delta < \infty \tag{4.6}$$

and, in particular,

$$w^{eff} = w(\varepsilon^0, \infty) \leq \langle w(\varepsilon^0, 10) \rangle \leq w(\varepsilon^0, 4) \leq w(\varepsilon^0, 1) \equiv w^V \quad 1 < 4 < 10 < \infty,$$

where w is the energy density, 1 stands for the pure hardest phase, and ε^0 stands for uniform kinematic boundary conditions. In this example, the energy density w can be interpreted as the area under the stress-strain curve with respect to the strain-axis in Figure 4.9. Also,

$$w^{*eff} = w^*(\sigma^0, \infty) \leq \langle w^*(\sigma^0, \delta) \rangle \leq w^*(\sigma^0, \delta') \leq w^*(\sigma^0, 1) \equiv w^{*R} \quad 1 < \delta' < \delta < \infty \tag{4.7}$$

and, in particular,

$$w^{*eff} = w^*(\sigma^0, \infty) \leq \langle w^*(\sigma^0, 10) \rangle \leq w^*(\sigma^0, 4) \leq w^*(\sigma^0, 1) \equiv w^{*R} \quad 1 < 4 < 10 < \infty,$$

where w^* is the complementary energy density and σ^0 stands for uniform traction boundary conditions. The complementary energy density w^* can be interpreted as the area under the stress-strain curve with respect to the stress-axis in Figure 4.9. The larger is the test domain, the smaller is the stored energy, and this gives bounds on effective medium.

Now, recall from Chapter 3 the hierarchies of scale-dependent bounds on tangent moduli (the tangent of a stress-strain curve at any effective strain level in Figure 4.9):

$$C^{Teff} \equiv C^T(\varepsilon^0, \infty) \leq \langle C^T(\varepsilon^0, \delta) \rangle \leq \langle C^T(\varepsilon^0, \delta') \rangle \leq \langle C^T(\varepsilon^0, 1) \rangle \tag{4.8}$$

$$S^{Teff} \equiv S^T(\sigma^0, \infty) \leq \langle S^T(\sigma^0, \delta) \rangle \leq \langle S^T(\sigma^0, \delta') \rangle \leq \langle S^T(\sigma^0, 1) \rangle \tag{4.9}$$

$$\delta' < \delta < \infty,$$

where C^T is the tangent stiffness and S^T is the tangent compliance. The larger is the test domain, the smaller is the tangent stiffness, and this gives bounds on effective medium.

Figure 4.10 shows that the result of the numerical simulation is consistent with the bound hierarchies 4.9.

4.3 Paper as an elastic-plastic orthotropic material

4.3.1 Experimental

Stress-strain curves under uniaxial and biaxial loading were obtained in paper specimens of 145 × 145 mm and elastic modulus values from the initial slope of these curves were calculated as the input for the simulation model. The material selected was commercial-grade paper sheets, *white textured Crayola sketchpaper*, with a nominal thickness of 130 μm and grammage of 70 g/m^2.

Uniaxial MD and CD standard tests (Tappi T-494) were also performed in an Instron tensile tester on paper samples preconditioned at 23°C, 20% relative humidity (RH), then conditioned and tested at 23°C, 20% RH (Tappi Standard T-402). On the other hand, Figure 4.11 shows a picture of the biaxial testing setup used. For the biaxial strain tests, the paper samples were also preconditioned at 23°C, 20% RH but were not tested at the same standard conditions. Figure 4.12 compares the stress-strain curves from uniaxial standard tests in MD and CD carried out in the

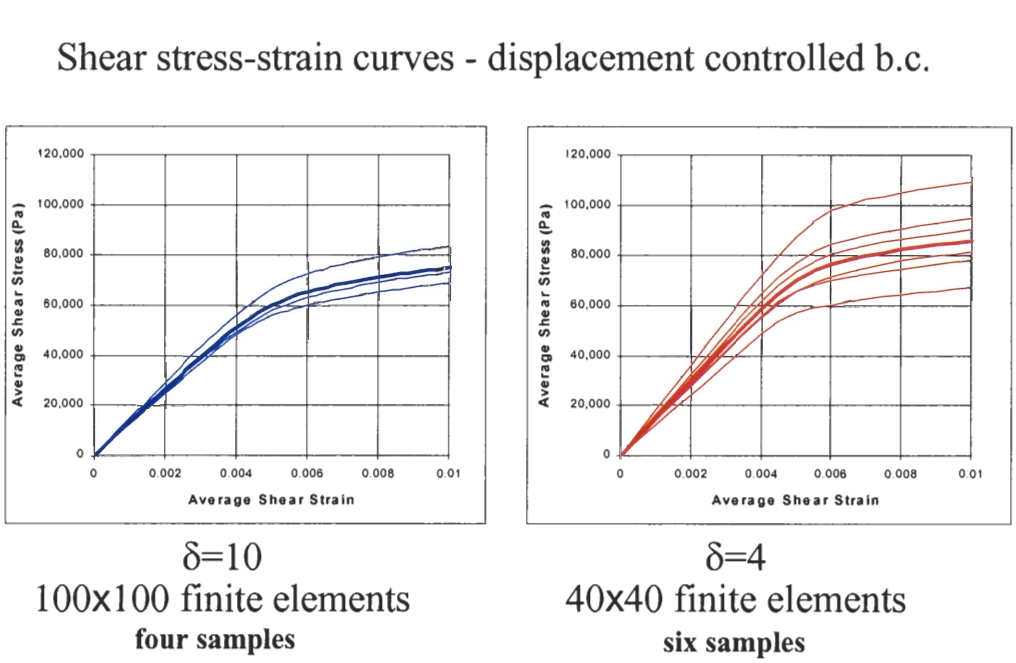


Figure 4.9: Comparison of effective responses according to mesoscale and applied boundary conditions

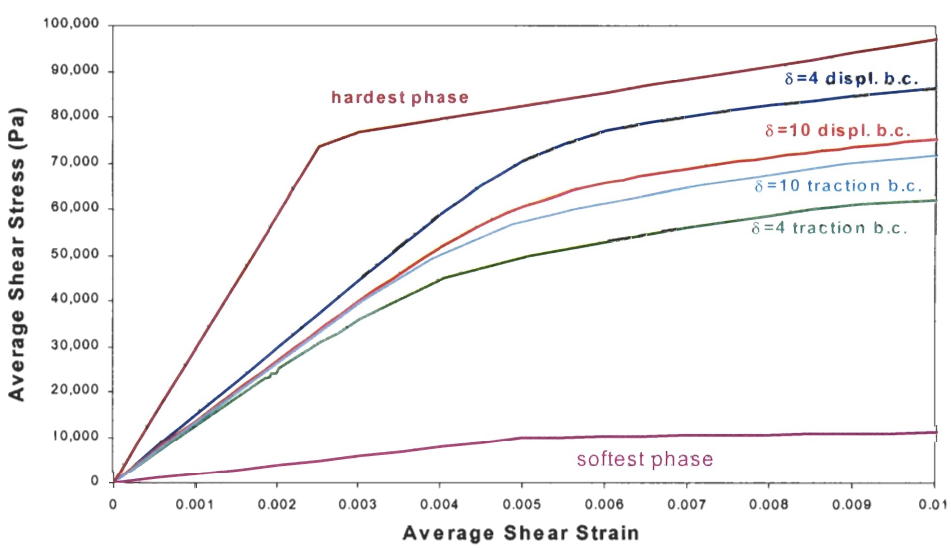


Figure 4.10: Shear stress-strain curves of effective response

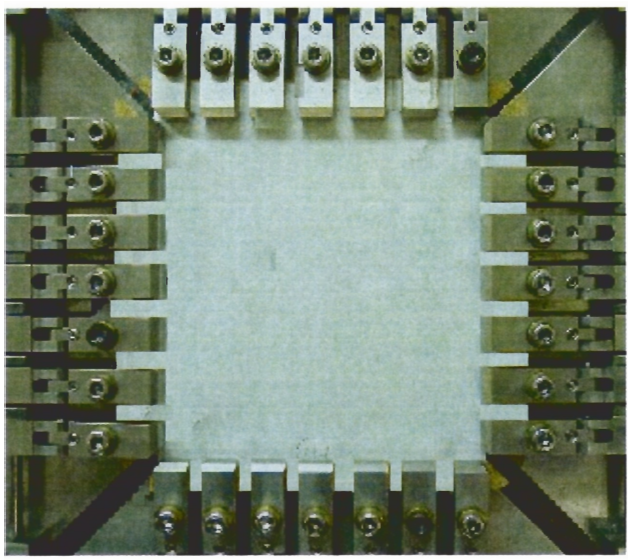


Figure 4.11: Biaxial testing setup with a squared paper specimen clamped at its edges.

Instron and the biaxial tester. The comparison shows that the results are consistent despite the difference in ambient conditions.

Figures 4.15 and 4.16 show stress-strain curves of the 145×145-mm paper coupons under different uniform displacement boundary conditions. All four clamps are semi-rigid along their length. Several combinations of loading strain-rates were applied. Specifically, 11 ratios of MD-CD strain rates were considered as shown in Table 4.1.

Figure 4.13 illustrates the applied boundary conditions of some of these cases on a 10×10 grid. The arrows on the boundary indicate the velocity (strain rate) vectors.

Similar biaxial tests to those of the present work were carried out by Uesaka, Murakami, and Imamura (1979). Figure 4.14 presents three biaxial stress-strain diagrams for kraft paper corresponding to three loading regimes I, II, III (machine direction parallel to y) from their work. To clarify the notation of Table 4.1, loading regime I in Figure 4.14 corresponds to case (1, 1) as in Figure 4.13 and regimes II and III to cases (1, 0) and (0, 1), respectively (note that in the present Thesis the machine direction is parallel to x-axis).

Figure 4.17 shows the equivalent curves for all loading cases but in the stress plane. On the other hand, uniaxial tensile tests were carried out in an Instron device. The average elastic moduli from these tests were rounded to $E_1 = 4400$ MPa in MD and $E_2 = 2200$ MPa in CD. Also, from these curves, the yield stress was approximated to 20 and 10 MPa in MD and CD, respectively. On the other hand, it is possible to estimate Poisson's ratios from the biaxial tests; ν_{12} was determined to be 0.20 from case (1.0, 0.0) and ν_{21} was 0.10 from case (0.0, 1.0) as will be explained ahead in detail (see Figures 4.15 and 4.16). All these values were input to the computer model as the average values of their corresponding mechanical property.

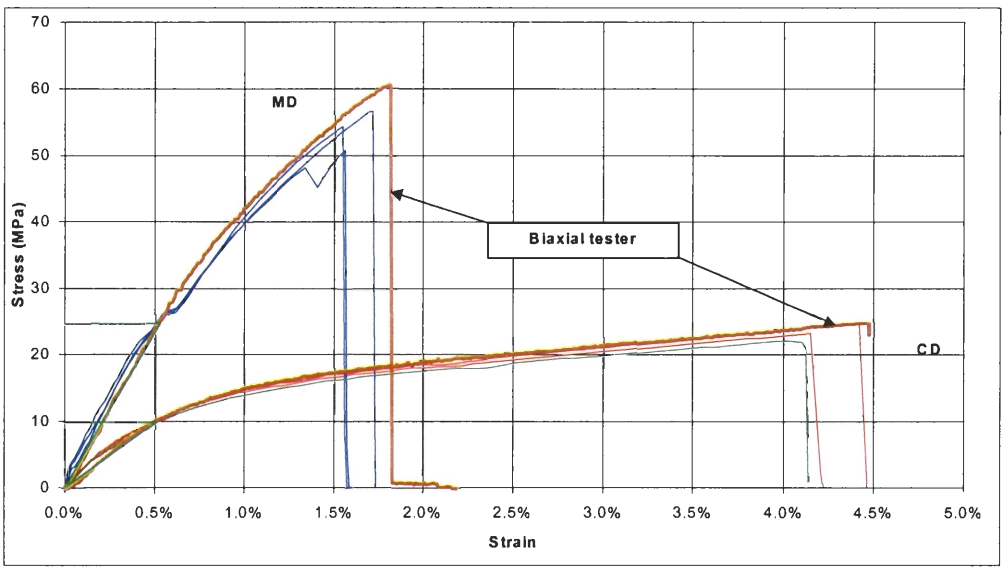


Figure 4.12: Stress-strain curves. Uniaxial loading in MD and CD.

Loading Case	MD (X-axis)	CD (Y-axis)
(1.0, -0.2)	0.5 mm/s	-0.1mm/s
(1.0, 0.0)	0.5 mm/s	0.0 mm/s
(1.0, 0.2)	0.5 mm/s	0.1 mm/s
(1.0, 0.4)	0.5 mm/s	0.2 mm/s
(1.0, 0.6)	0.5 mm/s	0.3 mm/s
(1.0, 1.0)	0.5 mm/s	0.5 mm/s
(0.6, 1.0)	0.3 mm/s	0.5 mm/s
(0.4, 1.0)	0.2 mm/s	0.5 mm/s
(0.2, 1.0)	0.1 mm/s	0.5 mm/s
(0.1, 1.0)	0.05 mm/s	0.5 mm/s
(-0.1, 1.0)	-0.05 mm/s	0.5 mm/s

Table 4.1: Loading cases under uniform displacement b.c.

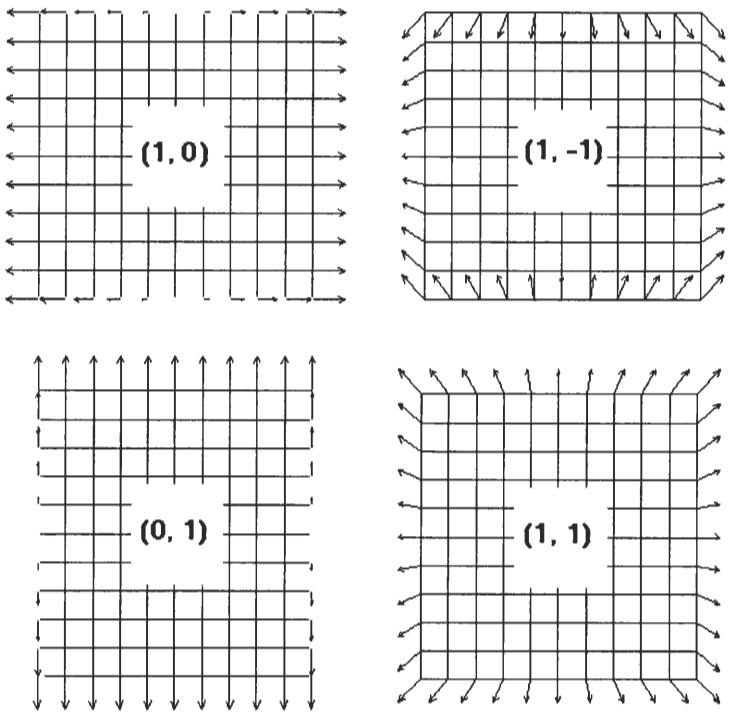


Figure 4.13: Example of applied boundary conditions for cases (1, 0), (0,1), (1,-1) and (1,1).

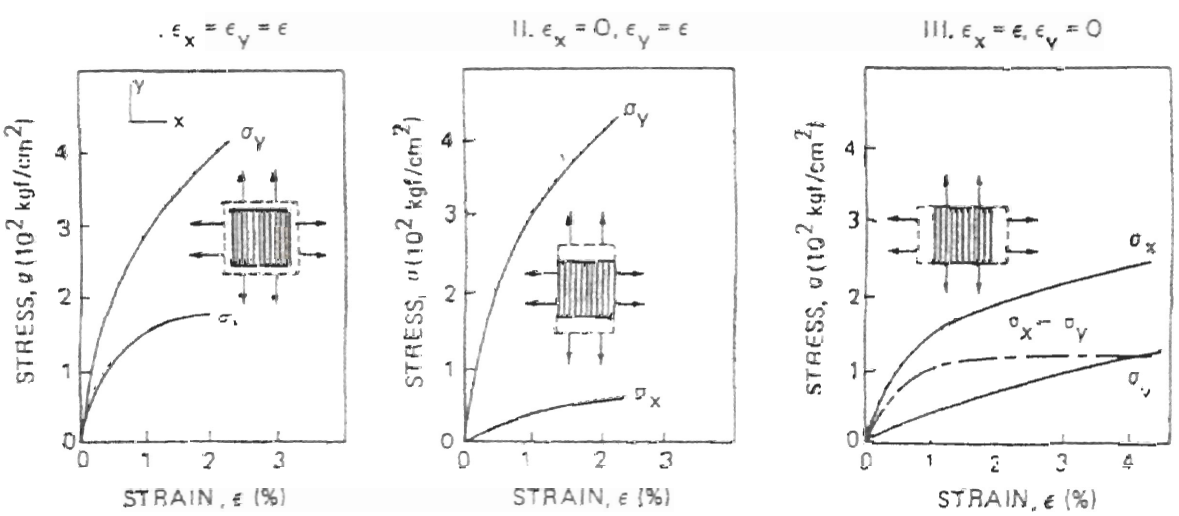


Figure 4.14: Biaxial stress-strain diagrams for kraft paper corresponding to three loading regimes I, II, III (machine direction parallel to y) from Uesaka, Murakami, and Imamura (1979).

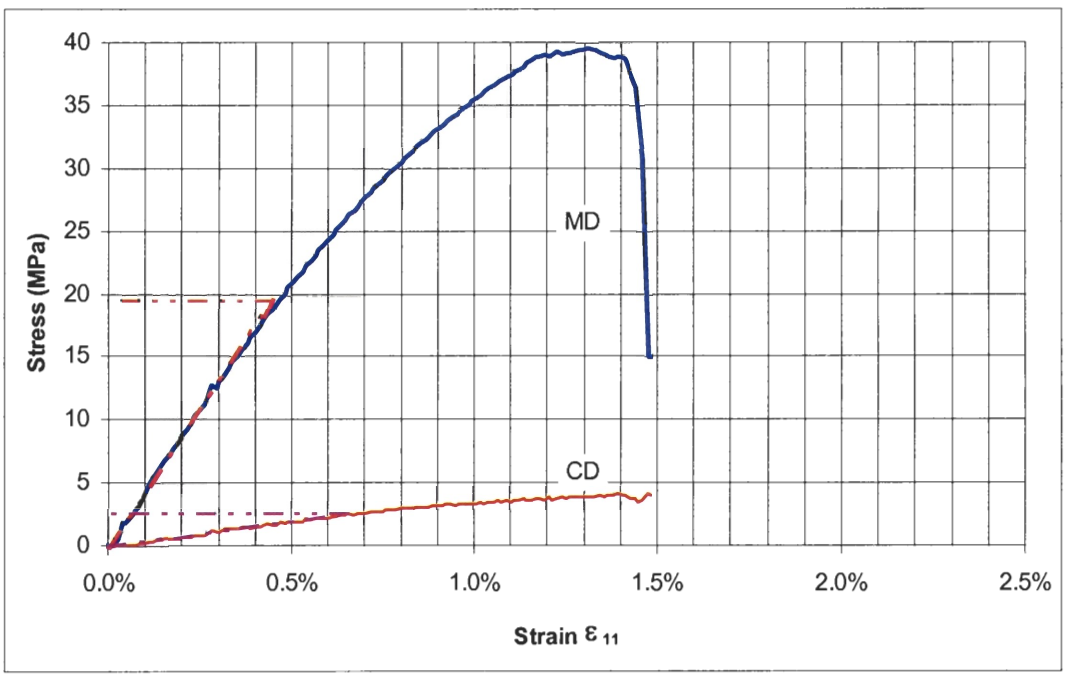


Figure 4.15: Stress-strain curves - Case (1.0, 0.0).

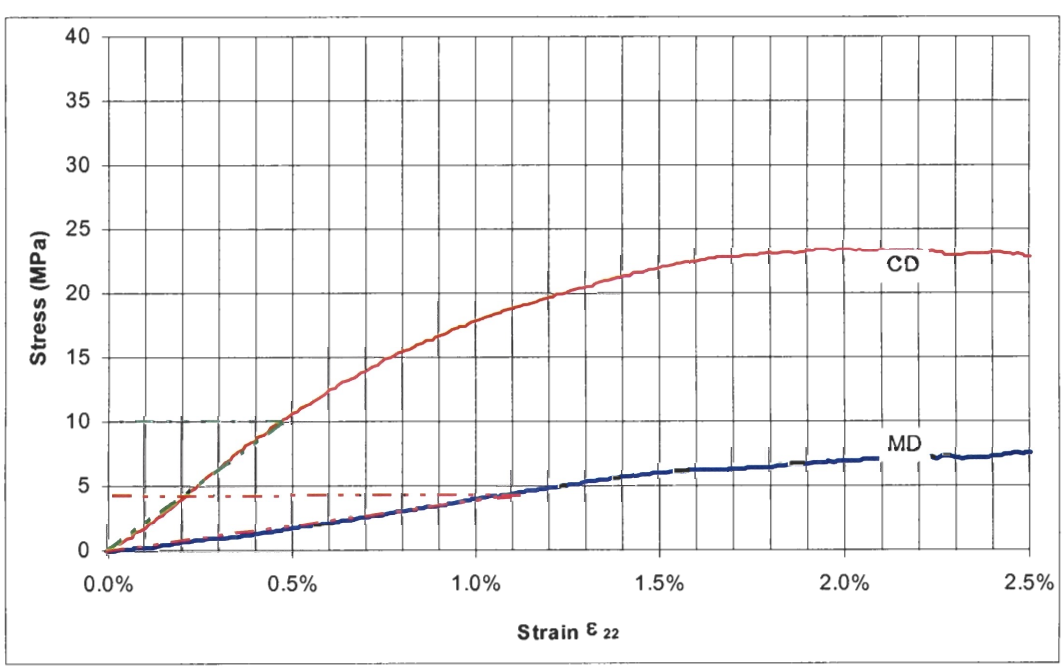


Figure 4.16: Stress-strain curves - Case (0.0, 1.0).

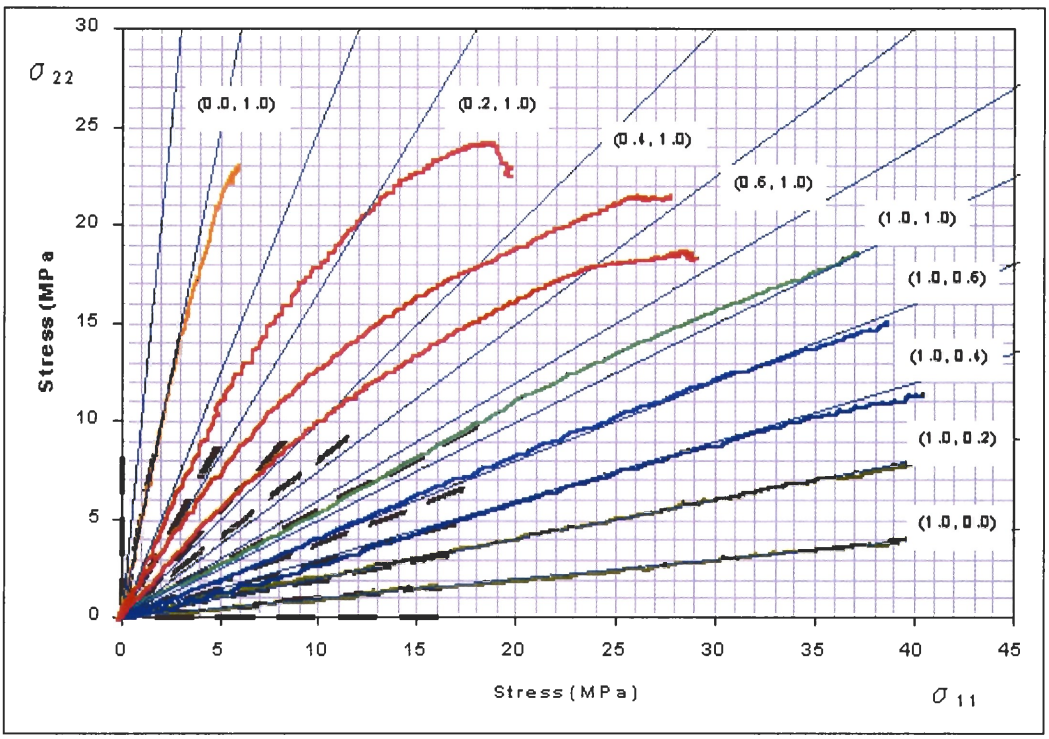


Figure 4.17: CD vs. MD-stress response of several loading cases. Solid lines are experimental curves and dashed lines are the curves predicted by linear-elastic orthotropy up to the yield point.

The biaxial data also provide the means to approximate the yield and failure surfaces. Paper samples seem to yield at 20 and 10 MPa in MD and CD respectively. The failure envelope can be approximated by the tensorial stress analysis theory (Johnson et al., 1985). For the 2-D case, in plane stress, the failure curve can be modeled by an ellipse, such as:

$$F_{11}\sigma_1^2 + 2F_{12}\sigma_1\sigma_2 + F_{22}\sigma_2^2 + F_{66}\tau_{12} = 1 \tag{4.10}$$

Subscripts 1 and 2 denote MD or x-axis and CD or y-axis, respectively. Excepting F_{12}, the coefficients in Equation (4.10) can be approximated by the following expressions:

$$F_{11} = \frac{1}{XX'} \qquad F_{22} = \frac{1}{YY'} \qquad F_{66} = \frac{1}{S^2}$$

where $X, X\prime, Y$, and $Y\prime$ are the tensile and compressive strengths in MD and CD, respectively, and S is the pure shear strength.

Table 4.2 presents a set of strength values in MPa that approximates the elliptical failure surface shown in Figure 4.18 when $F_{12} = 0$.

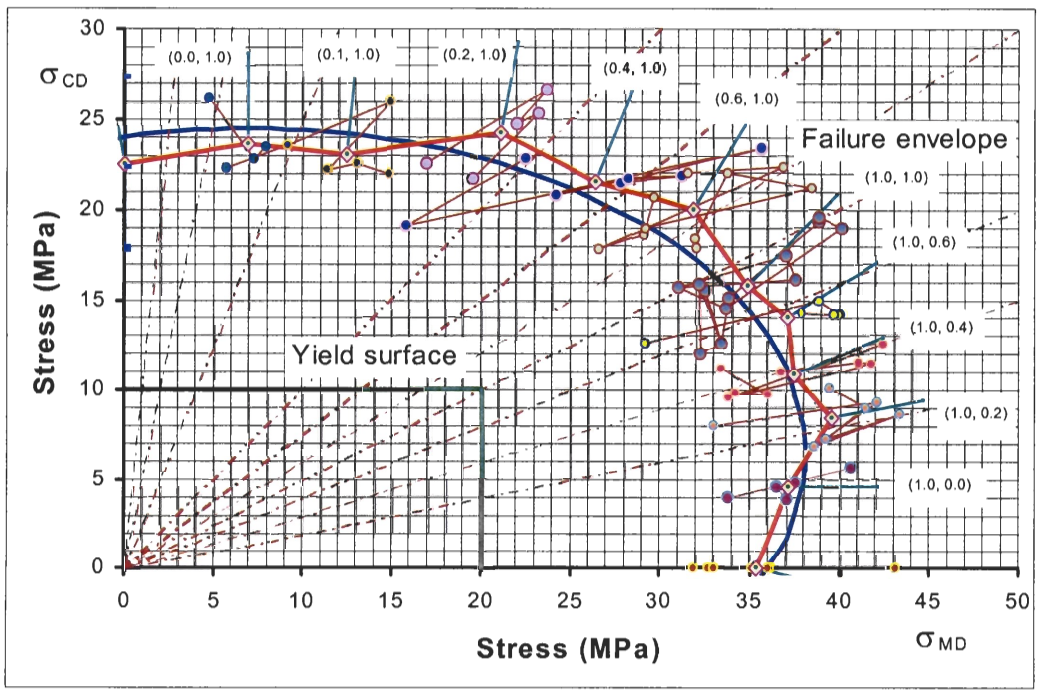


Figure 4.18: Yield and failure surfaces of paper.

Strength	Value
X	36 MPa
X'	22 MPa
Y	24 MPa
Y'	11 MPa
S	15 MPa

Table 4.2: Tensile, compressive, and shear strength values.

4.3.2 Elastic orthotropic model

The linear elastic behavior of paper before yielding can be modeled through the orthotropic model (see Uesaka, Murakami, and Imamura, 1979). Equation (1.1) can also be expressed as:

$$\sigma_{11} = \frac{E_1}{(1-\nu_{12}\nu_{21})}\varepsilon_{11} + \frac{E_2\nu_{12}}{(1-\nu_{12}\nu_{21})}\varepsilon_{22} \tag{4.11}$$

$$\sigma_{22} = \frac{E_1\nu_{21}}{(1-\nu_{12}\nu_{21})}\varepsilon_{11} + \frac{E_2}{(1-\nu_{12}\nu_{21})}\varepsilon_{22} \tag{4.12}$$

$$\tau_{12} = G\gamma_{12} = 2G\varepsilon_{12} \tag{4.13}$$

The engineering constants for an orthotropic material are:

E_1 = Young's modulus 1-direction (MD).

E_2 = Young's modulus in 2-direction (CD).

$\nu_{12} = \dfrac{-\varepsilon_{22}}{\varepsilon_{11}}$ is the Poisson's ratio for strain in 2-direction (CD) when paper is stressed in 1-direction (MD) only.

$\nu_{21} = \dfrac{-\varepsilon_{11}}{\varepsilon_{22}}$ is the Poisson's ratio for strain in 1-direction (MD) when paper is stressed in 2-direction (CD) only.

G = shear modulus in 1-2-Plane.

However, a constant proportionality between elastic moduli E_1 and E_2, and Poisson's ratios ν_{12} and ν_{21} is required to ensure that the stiffness matrix in equation (1.1) is orthotropic. That is:

$$\frac{E_1}{E_2} = \frac{\nu_{12}}{\nu_{21}} \qquad or \qquad E_1\nu_{21} = E_2\nu_{12} \tag{4.14}$$

Subscripts 1 and 2 denote MD or x-axis and CD or y-axis, respectively. The shear modulus G can be approximated using the expression proposed by Campbell (1961) (see also Ostoja-Starzewski and Stahl, 2001):

$$G = \frac{E_1E_2}{E_2 + E_1 + E_1\nu_{21} + E_2\nu_{12}} \tag{4.15}$$

Seo et al. (1992) proposed an alternative way of calculating G involving measurements of Young's modulus E_Θ at an angle Θ from the machine direction:

$$G = \frac{\cos^2\Theta\sin^2\Theta}{\dfrac{1}{E_\Theta} - \left[\dfrac{\cos^4\Theta}{E_1} + \dfrac{\sin^4\Theta}{E_2} - \dfrac{2\nu_{12}}{E_1}\cos^2\Theta\sin^2\Theta\right]} \tag{4.16}$$

From the loading case (1.0, 0.0), the strain rate in CD is zero ($\varepsilon_{22} = 0$). Thus, dividing (4.12) by (4.11) the ratio of stresses in MD and CD becomes:

$$\frac{\sigma_{22}}{\sigma_{11}} = \nu_{21} \tag{4.17}$$

Property	Value
E_1	5.5 GPa
E_2	2.12 GPa
G	1.32 GPa
ν_{12}	0.18
ν_{21}	0.46
Thickness	0.136 mm

Table 4.3: Mechanical properties from ultrasound measurements.

From Figure 4.17, the initial slope of this curve is $\nu_{21} = 0.10$. Its value is fairly constant up to failure. Similarly, from case (0.0, 1.0), the strain rate in MD is zero ($\varepsilon_{11} = 0$). Thus, dividing (4.11) by (4.12):

$$\frac{\sigma_{11}}{\sigma_{22}} = \nu_{21} \tag{4.18}$$

and the initial slope is $\nu_{12} = 0.20$ from Figure 4.17. However, in the former case the slope decreases with loading. In general, the behavior of these curves is linear when the MD strain rate is dominant (cases (1.0, 0.0) to (1.0, 0.6)), while the nonlinearity of the curves is evident when the CD strain rate is dominant (cases (0.0, 0.6) to (0.0, 1.0)).

With the values found for paper's engineering constant, G can be estimated now as:

$$G = \frac{E_1 E_2}{E_2 + E_1 + E_1\nu_{21} + E_2\nu_{12}} = 1294 \text{ MPa}$$

or taking $\Theta = \frac{\pi}{4}$ and $E_\Theta = 3047$ MPa from an uniaxial test of an off-axis specimen at 45°:

$$G = \frac{\cos^2\Theta \sin^2\Theta}{\frac{1}{E_\Theta} - \left(\frac{\cos^4\Theta}{E_1} + \frac{\sin^4\Theta}{E_2} - \frac{2\nu_{12}}{E_1}\cos^2\Theta \sin^2\Theta\right)} = 1313.3 \text{ MPa}$$

The mechanical properties were also measured with the ultrasonic testing devices of IPST. These measurements are summarized in Table 4.3 (paper's basis weight is 69.22 g/m^2 and mass density $\rho = 508$ kg/m^3). As expected (see Baum et al., 1983), the MD-elastic modulus from the ultrasound measurement is larger than that measured mechanically and the CD-elastic modulus is smaller than that determined mechanically.

Using the determined values of Poisson's ratios and the value for G from Equation (4.15), the orthotropic model (Equations 4.11 to 4.13) for a homogeneous material gives the dashed lines shown in Figure 4.17 for each loading case. Again, the agreement with the experimental curves is better in the range where MD-strain rate dominates than in the range where CD-strain rate dominates.

In conclusion, it would be desirable to find an appropriate nonlinear constitutive law as the input for the simulation model.

4.3.3 Nonlinear hyperelastic orthotropic model

With reference to our discussion in Section 3.2.2, there is a need for a nonlinear elastic model of paper, applicable to the loading conditions. Let us begin by assuming that the stress-strain response of paper can be fitted with an equation of the following form:

$$\frac{dw(\varepsilon_{11})}{d\varepsilon_{11}} = \sigma_{11} = A\tanh(b\varepsilon_{11}) \tag{4.19}$$

where A and b are constants to be determined from the experimental data. Conducting a mathematical development similar to that of Johnson and Urbanik (1984) and Suhling et. al. (1989), the empirical equation (4.19) can be integrated to find the stress energy function w (see Section 1.1.4):

$$w(\varepsilon_{11}) = \int A\tanh(b\varepsilon_{11})d\varepsilon_{11} = \frac{A}{b}\log\left[\cosh(b\varepsilon_{11})\right] \tag{4.20}$$

and expressing this equation as a function of the effective strain e, it can be written as:

$$w(e) = \frac{A}{b}\log\left[\cosh\left(b\sqrt{\frac{\nu_{21}e}{1-\nu_{12}\nu_{21}}}\right)\right] \tag{4.21}$$

Deriving now with respect to e:

$$\frac{dw(e)}{de} = \frac{A}{2\sqrt{e}}\sqrt{\frac{\nu_{21}}{(1-\nu_{12}\nu_{21})}}\tanh\left(b\sqrt{\frac{\nu_{21}e}{1-\nu_{12}\nu_{21}}}\right) \tag{4.22}$$

Retaking Equation (1.6), it can also be written as:

$$\sigma_{11} = \frac{2}{\nu_{21}}\frac{dw(e)}{de}\varepsilon_{11} + 2\frac{dw(e)}{de}\varepsilon_{22} \tag{4.23}$$

$$\sigma_{22} = 2\frac{dw(e)}{de}\varepsilon_{11} + \frac{2}{\nu_{12}}\frac{dw(e)}{de}\varepsilon_{22} \tag{4.24}$$

$$\tau_{12} = 2\frac{dw(e)}{de}(1-\nu_{12}\nu_{21})\frac{G}{v_{12}E_1}\gamma_{12} \tag{4.25}$$

where

$$\varepsilon_{11} = \sqrt{\frac{\nu_{21}e}{1-\nu_{12}\nu_{21}}} \tag{4.26}$$

and

$$\varepsilon_{22} = \sqrt{\frac{\nu_{12} e}{1 - \nu_{12}\nu_{21}}} \tag{4.27}$$

Substituting (4.22) into Equations (4.24) through (4.25), we arrive to:

$$\begin{aligned} \sigma_{11} = & \frac{A}{\nu_{21}\sqrt{e}}\sqrt{\frac{\nu_{21}}{(1-\nu_{12}\nu_{21})}}\tanh\left(b\sqrt{\frac{\nu_{21}e}{1-\nu_{12}\nu_{21}}}\right)\varepsilon_{11} + \\ & \frac{A}{\sqrt{e}}\sqrt{\frac{\nu_{21}}{(1-\nu_{12}\nu_{21})}}\tanh\left(b\sqrt{\frac{\nu_{21}e}{1-\nu_{12}\nu_{21}}}\right)\varepsilon_{22} \end{aligned} \tag{4.28}$$

$$\begin{aligned} \sigma_{22} = & \frac{A}{\sqrt{e}}\sqrt{\frac{\nu_{21}}{(1-\nu_{12}\nu_{21})}}\tanh\left(b\sqrt{\frac{\nu_{21}e}{1-\nu_{12}\nu_{21}}}\right)\varepsilon_{11} + \\ & \frac{A}{\nu_{12}\sqrt{e}}\sqrt{\frac{\nu_{21}}{(1-\nu_{12}\nu_{21})}}\tanh\left(b\sqrt{\frac{\nu_{21}e}{1-\nu_{12}\nu_{21}}}\right)\varepsilon_{22} \end{aligned} \tag{4.29}$$

$$\tau_{12} = \frac{A}{\sqrt{e}}\sqrt{\frac{\nu_{21}}{(1-\nu_{12}\nu_{21})}}\tanh\left(b\sqrt{\frac{\nu_{21}e}{1-\nu_{12}\nu_{21}}}\right)(1-\nu_{12}\nu_{21})\frac{G}{v_{12}E_1}\gamma_{12} \tag{4.30}$$

From a biaxial tensile test with $\varepsilon_{22} = 0$ (loading case (1, 0)) and replacing back ε_{11} in (4.28), it follows that:

$$\sigma_{11}^{(1,\,0)} = \frac{A}{(1-\nu_{12}\nu_{21})}\tanh(b\varepsilon_{11}) \tag{4.31}$$

and fitting the corresponding stress-strain curves in Figure 4.15, the value of b can be estimated. On the other hand, differentiating this equation with respect to ε_{11} allows the evaluation of the initial (zero strain) elastic modulus Q_{11} of such a curve (see Figure 4.19) as:

$$Q_{11} = \frac{d\sigma_{11}^{(1,\,0)}(0)}{d\varepsilon_{11}} = \frac{Ab}{(1-\nu_{12}\nu_{21})}\cosh^{-2}(0) = \frac{Ab}{(1-\nu_{12}\nu_{21})} \tag{4.32}$$

and similarly, replacing back ε_{22} in (4.29), Q_{21} can be found:

$$\sigma_{22}^{(1,\,0)} = \frac{A\nu_{21}}{(1-\nu_{12}\nu_{21})}\tanh(b\varepsilon_{11}) \tag{4.33}$$

$$Q_{21} = \frac{d\sigma_{22}^{(1,\,0)}(0)}{d\varepsilon_{11}} = \frac{Ab\nu_{21}}{(1-\nu_{12}\nu_{21})}\cosh^{-2}(0) = \frac{Ab\nu_{21}}{(1-\nu_{12}\nu_{21})} \tag{4.34}$$

Following the same procedure and according to the corresponding stress-strain curves in Figure 4.16, Equations (4.28) and (4.29) allow the evaluation of Q_{12} and Q_{22}, respectively, as:

$$\sigma_{11}^{(0,\,1)} = A\frac{\sqrt{\nu_{12}\nu_{21}}}{1-\nu_{12}\nu_{21}}\tanh\left(b\sqrt{\frac{\nu_{21}}{\nu_{12}}}\varepsilon_{22}\right) \tag{4.35}$$

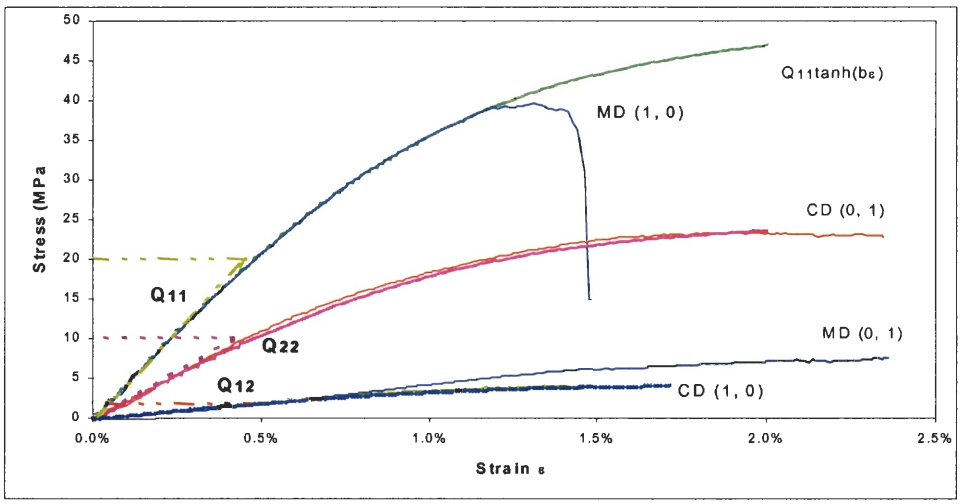


Figure 4.19: Stress-strain curve fitting - Loading cases (1.0, 1.0) and (0.0, 1.0).

$$Q_{12} = \frac{d\sigma_{11}^{(0,\,1)}(0)}{d\varepsilon_{22}} = Ab\frac{\sqrt{\nu_{12}\nu_{21}}}{1-\nu_{12}\nu_{21}}\sqrt{\frac{\nu_{21}}{\nu_{12}}}\cosh^{-2}(0) = \frac{Ab\nu_{21}}{(1-\nu_{12}\nu_{21})} = Q_{21} \tag{4.36}$$

$$\sigma_{22}^{(0,\,1)} = \frac{A}{1-\nu_{12}\nu_{21}}\sqrt{\frac{\nu_{21}}{\nu_{12}}}\tanh\left(b\sqrt{\frac{\nu_{21}}{\nu_{12}}}\varepsilon_{22}\right) \tag{4.37}$$

$$Q_{22} = \frac{d_{22}^{(0,\,1)}(0)}{d\varepsilon_{22}} = \frac{Ab}{1-\nu_{12}\nu_{21}}\frac{\nu_{21}}{\nu_{12}}\cosh^{-2}(0) = \frac{Ab}{(1-\nu_{12}\nu_{21})}\frac{\nu_{21}}{\nu_{12}} \tag{4.38}$$

From an uniaxial stress-strain curve in MD, $\sigma_{22} = \tau_{12} = 0$ and:

$$\sigma_{11}^{(MD)} = \frac{A}{(1-\nu_{12}\nu_{21})}\tanh(b\varepsilon_{11}) + A\frac{\sqrt{\nu_{12}\nu_{21}}}{1-\nu_{12}\nu_{21}}\tanh\left(b\sqrt{\frac{\nu_{21}}{\nu_{12}}}(-\nu_{12}\varepsilon_{11})\right) \tag{4.39}$$

$$E_{MD} = E_1 = \frac{d\sigma_{11}^{(MD)}(0)}{d\varepsilon_{11}} = \frac{Ab}{(1-\nu_{12}\nu_{21})}\cosh^{-2}(0) + \frac{-Ab\nu_{21}\nu_{12}}{(1-\nu_{12}\nu_{21})}\cosh^{-2}(0) \tag{4.40}$$

Therefore, clearly $E_{MD} = E_1 = Ab$. Rearranging Equations (4.24) through (4.25) and recalling that relation $E_2\nu_{12} = E_1\nu_{21}$ must be satisfied, it follows that:

$$\sigma_{11} = \frac{E_1}{b(1-\nu_{12}\nu_{21})}\tanh(b\varepsilon_{11}) + \frac{E_2\nu_{12}}{b(1-\nu_{12}\nu_{21})}\tanh\left(b\sqrt{\frac{\nu_{21}}{\nu_{12}}}\varepsilon_{22}\right) \tag{4.41}$$

$$\sigma_{22} = \frac{E_1\nu_{21}}{b(1-\nu_{12}\nu_{21})}\tanh(b\varepsilon_{11}) + \frac{E_2}{b(1-\nu_{12}\nu_{21})}\tanh\left(b\sqrt{\frac{\nu_{21}}{\nu_{12}}}\varepsilon_{22}\right) \tag{4.42}$$

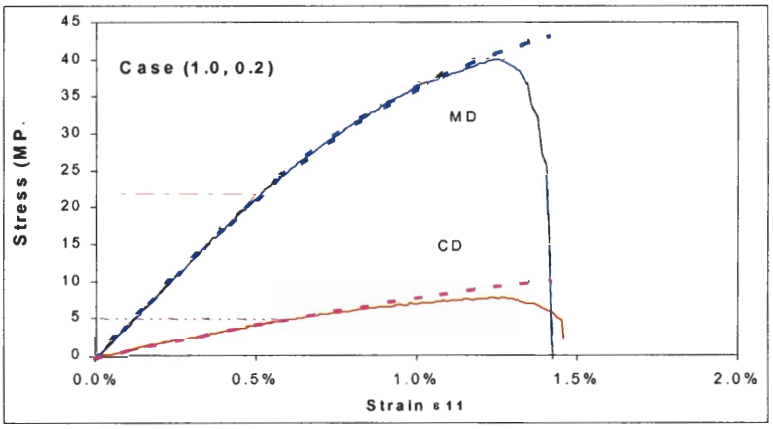


Figure 4.20: Stress-strain curve of loading case (1.0, 0.2). Solid lines are experimental curves and dashed lines are predicted curves.

$$\tau_{12} = \frac{G}{b\varepsilon_{11}} \tanh\left(b\varepsilon_{11}\right) \gamma_{12} \tag{4.43}$$

or in matrix form:

$$\begin{bmatrix} \sigma_{11} \\ \sigma_{22} \\ \tau_{12} \end{bmatrix} = \frac{1}{b} \begin{bmatrix} Q_{11} & Q_{12} & 0 \\ Q_{12} & Q_{22} & 0 \\ 0 & 0 & G \end{bmatrix} \begin{bmatrix} \tanh\left(b\varepsilon_{11}\right) \\ \tanh\left(b\sqrt{\frac{\nu_{21}}{\nu_{12}}}\varepsilon_{22}\right) \\ \dfrac{\tanh\left(b\varepsilon_{11}\right)}{\varepsilon_{11}}\gamma_{12} \end{bmatrix} \tag{4.44}$$

As reviewed in Section 1.1.4, Suhling et al. (1989) obtained different expressions for $dw(e)/de$ depending on whether it was obtained from the uniaxial MD or CD test. However, in the present case, expression (4.22) can be derived and fitted with the experimental data from either (1.0, 0) or (0, 1.0) loading cases. Figures 4.20 to 4.24 show the stress-strain curves predicted by Equation (4.44) and the experimental curves for various intermediate loading cases. There is an accurate agreement between both curves in general. It can be seen that yielding occurs around 0.5% strain and that around 0.75% strain, the experimental curve starts deviating from the predicted (dashed) line. The occurrence of this deviation was observed to coincide with the appearance of the first cracks, i.e., when damage initiates.

Figure 4.25 presents the CD vs. MD-stress response of the previous loading cases (solid lines are experimental curves and dashed lines are predicted curves). As it was the case with the linear elastic orthotropic model, with the hyperelastic orthotropic model the agreement with the experimental curves is better in the range where MD-strain rate dominates than in the range where CD-strain rate dominates.

As is well known (see review of Niskanen 1993, 1998), there is an approximately linear section at small strains in the load-elongation curve of paper. Nevertheless, the yield point has no unique definition because the deviation from the linear portion grows gradually as elongation increases. Another way to find a yield point in paper is

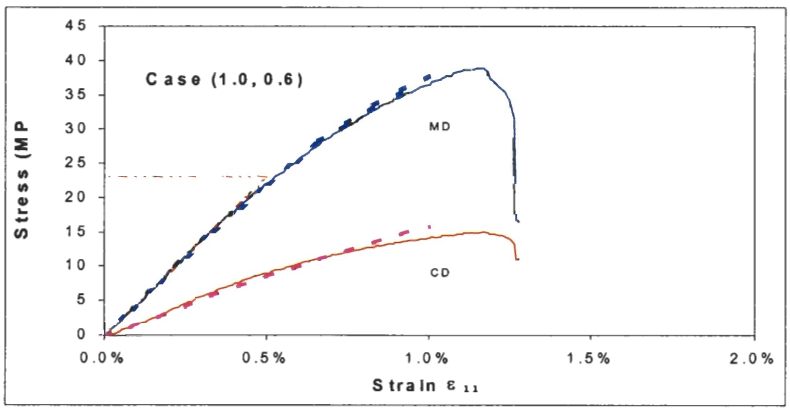


Figure 4.21: Stress-strain curve of loading case (1.0, 0.6). Solid lines are experimental curves and dashed lines are predicted curves.

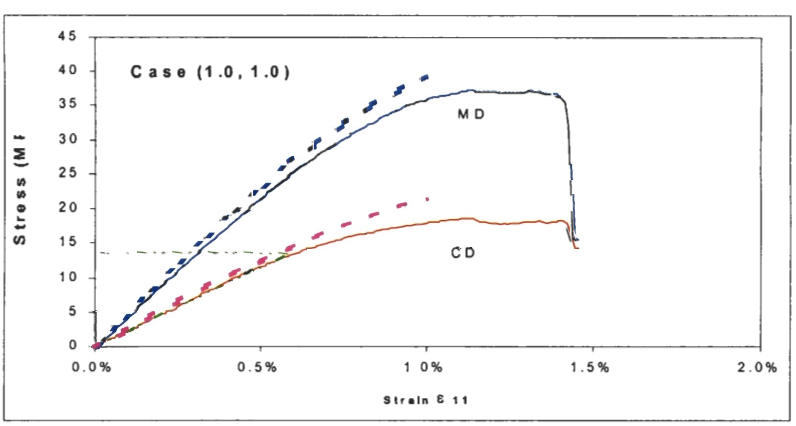


Figure 4.22: Stress-strain curve of loading case (1.0, 1.0). Solid lines are experimental curves and dashed lines are predicted curves.

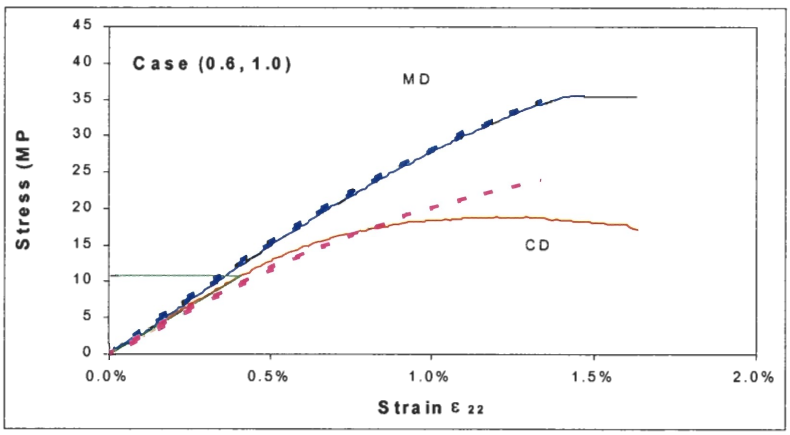


Figure 4.23: Stress-strain curve of loading case (0.6, 1.0). Solid lines are experimental curves and dashed lines are predicted curves.

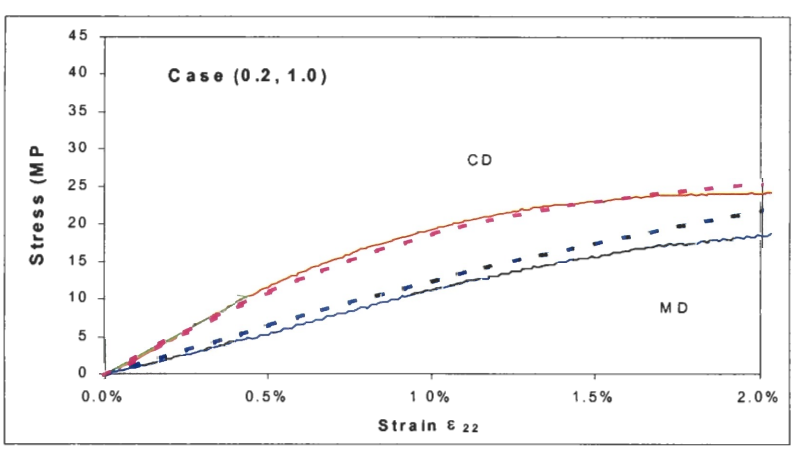


Figure 4.24: Stress-strain curve of loading case (0.2, 1.0). Solid lines are experimental curves and dashed lines are predicted curves.

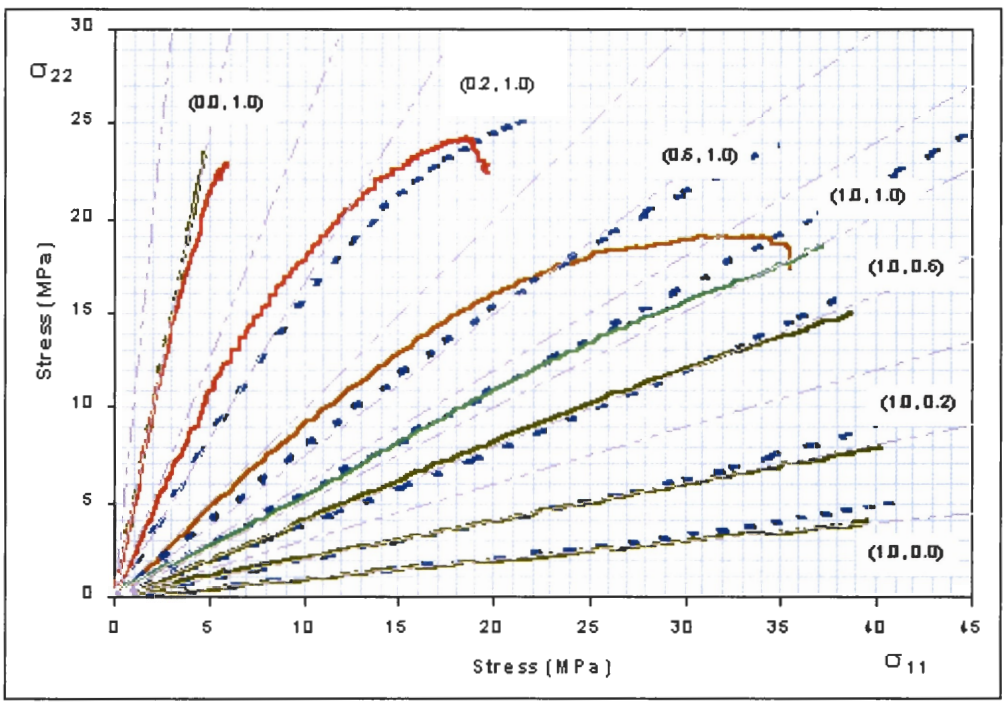


Figure 4.25: CD vs. MD-stress response of several loading cases. Solid lines are experimental curves and dashed lines are predicted curves.

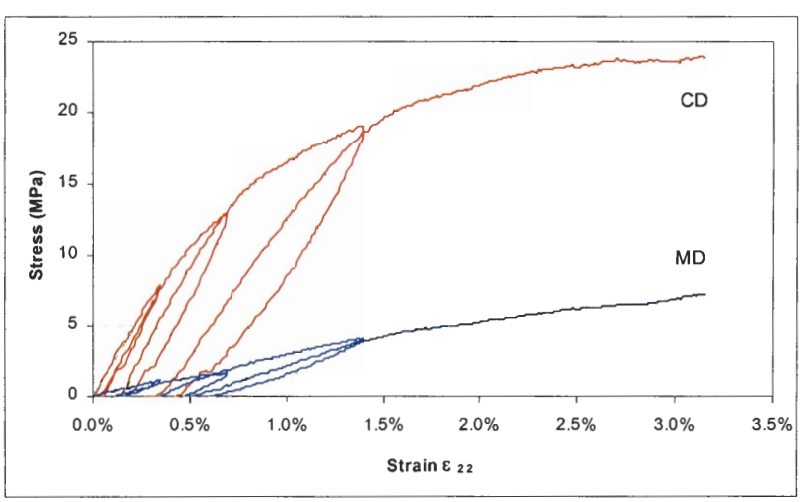


Figure 4.26: Stress-strain curve for case (0.0, 1.0) after biaxial cyclic loading and unloading.

through loading and unloading to determine the deviation point from elastic linearity, but, as seen in Figure 4.26, even for small strains that is not possible. In that sense (no precise yield point), the hyperbolic tangent function of the hyperelastic model (4.44) describes paper behavior well. It also describes its behavior under monotonic loading accurately, but it cannot describe its actual unloading behavior due to the hyperelastic assumption of such a model, i.e., a hyperelastic material returns to its initial state upon load removal. On the other hand, this constitutive model is rate-independent.

While the proposed derivation does not offer a very good fit for the entire range of strains and/or loading conditions, it is important to note that work on nonlinear hyperelastic models for anisotropic materials is beginning only now and is a formidable challenge in contemporary solid mechanics, e.g., Dłużewski (2000).

Chapter 5

Strain and Temperature Fields in Paper

5.1 Cross-correlation between formation and strain patterns

The formation data from Figure 4.4 were taken to perform a simulated uniaxial tensile test with the orthotropic model presented in the previous chapter. The obtained data were used to carry on the statistical analysis suggested by Dodson (1970) to correlate areal strain and paper grammage. Keeping his notation, a theoretical regression equation to predict the relative (normalized) areal dilatation $\langle\delta\rangle$ as a function of areal density $\widetilde{\beta}$ can be written as (in this section, δ is not related to the mesoscale):

$$\langle\delta\rangle = 1 + \frac{\left\{1/(\overline{\overline{\beta}/\widetilde{\beta}}) - 1\right\}}{Var\left(\widetilde{\beta}\right)}\overline{\beta}\left(\widetilde{\beta} - \overline{\beta}\right), \tag{5.1}$$

where $\overline{\beta}$ denotes the mean of $\widetilde{\beta}$. On the other hand, a linear regression is expressed as:

$$\langle\delta\rangle = 1 + \frac{cov\left(\widetilde{\beta}, \delta\right)}{Var\left(\widetilde{\beta}\right)}\left(\widetilde{\beta} - \overline{\beta}\right) \tag{5.2}$$

with a correlation coefficient given by:

$$Corr\left(\widetilde{\beta}, \delta\right) = \frac{cov\left(\widetilde{\beta}, \delta\right)}{\sqrt{Var\left(\widetilde{\beta}\right) Var\left(\delta\right)}}. \tag{5.3}$$

Figure 5.1 shows these two regression lines for the simulated relative areal dilatation and the corresponding correlation coefficient. A very good correlation is

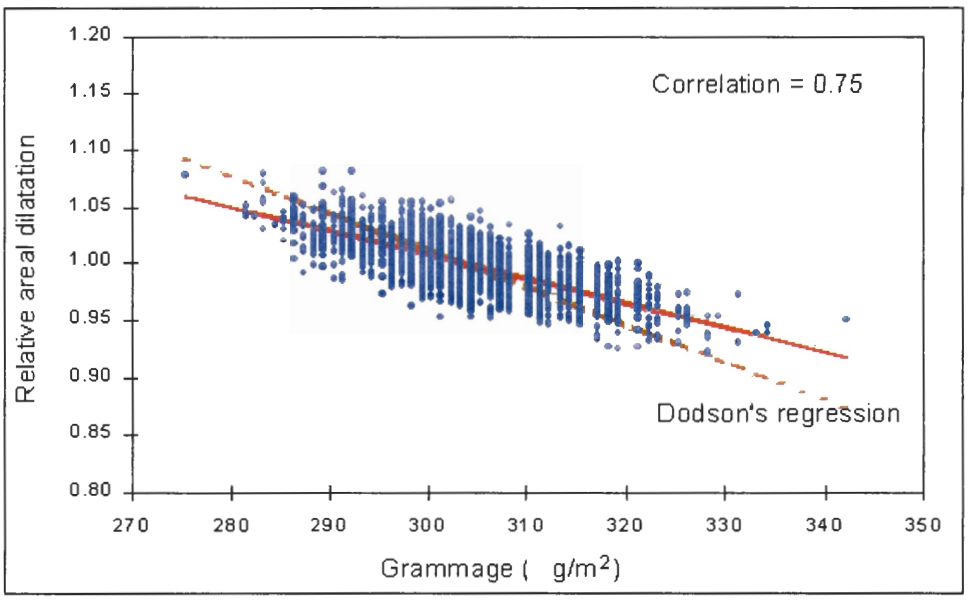


Figure 5.1: Simulated areal dilatation against local grammage of paperboard. Theorethical regression sugested by Dodson (1970) as a dashed line.

observed. However, this relation between $\langle\delta\rangle$ and β is purely statistical and does not involve solid mechanics.

We now consider the relation between paper's formation and effective strain on the basis of solid mechanics. Table 5.1 presents the values of mechanical properties from the previous chapter that were input to the computer model. Moreover, different distributions around the average were assigned to elastic moduli based on a reflective scanning of the samples' area. Specifically, Figure 5.2 shows a scanned image of a 70×80-mm sample of white Crayola sketchpaper, on the left, where features of paper formation like "fiber flocs" can be seen. This image was achieved with a Hewlett Packard scanner by backing the paper sample with a black surface as illustrated in Figure 5.3 and then taking the negative of this image. On the other hand, the image on the right was obtained from β-ray decay measurements with the resolution of one reading per each 1×1 mm of the equipment currently available at IPST. The two images correlate well and provide the same information about grammage. However, the scanned image is very easily attainable and, in this case, provides better resolution than the β-ray image.

Figure 5.4 shows the scanned image of another paper specimen obtained with the same technique explained above. From this gray-scale image, it was assumed that darker parts correspond to high basis weight zones. Therefore, a grammage distribution was found from the gray-scale zone and, in turn, this distribution was applied to paper's mechanical properties, i.e., Young's modulus, tensile strength, and, for the stepwise linear elastic model, yield strength (or its equivalent yield strain). As an example, the transformation from the optical gray scale into the elastic modulus

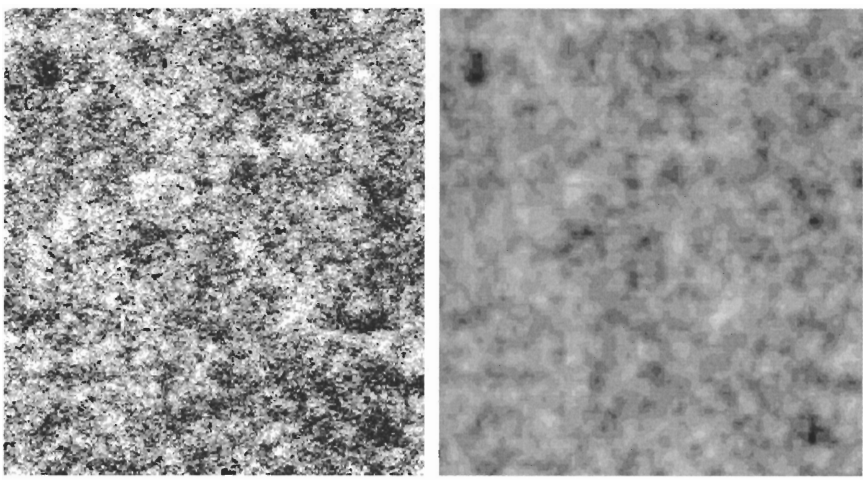


Figure 5.2: Formation of a paper sample of 70×80 mm from reflective scanning (left) and from β-ray radiography (right).

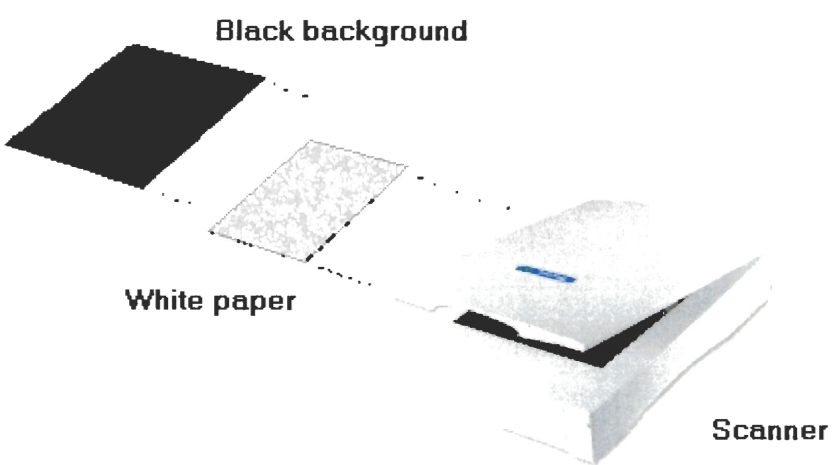


Figure 5.3: Mapping formation of a low basis weight white paper with a scanner.

Property	Value
E_1	4400 MPa
E_2	2200 MPa
ν_{12}	0.20
ν_{21}	0.10
b	90

Table 5.1: Experimentally measured material constants.

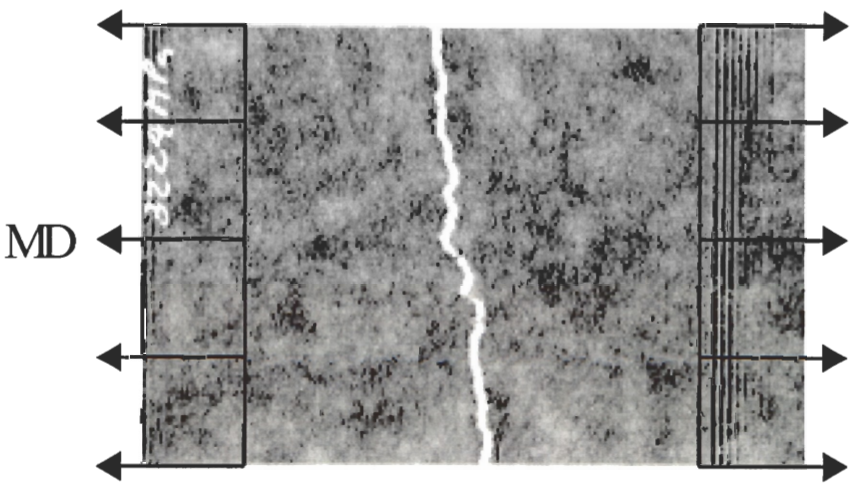


Figure 5.4: Scanned image of paper. The central portion is a square of 48 × 48 mm that was subjected to strain up to fracture.

in MD $E_1^{(i,j)}$ for each element (i, j) of the mesh is as follows:

$$E_1^{(i,j)} = \overline{E_1} \frac{Gray^{(i,j)}}{\overline{Gray}} \tag{5.4}$$

The portion of the sample under strain in Figure 5.4 corresponds to a square of 48×48 mm and it was simulated by using 1 × 1-mm elements.

Once again, a uniaxial test in MD is simulated with FLAC. This allows obtaining the stress or strain fields, which can be compared with the formation mapping to evaluate the influence of local property variability on effective response. Figure 5.5 presents the resulting von Mises strain field of such a simulation (on the bottom). The effective von Mises strain corresponds to the expression:

$$e_{Mises} = \varepsilon_{11}^2 - \varepsilon_{11}\varepsilon_{22} + \varepsilon_{22}^2 + 3\gamma_{12}^2 \tag{5.5}$$

The image on top of Figure 5.5 presents the resulting strain field from a simulation carried out on a homogeneous material. The only features that these two strain fields have in common is the strain concentration (darkest zones) in their corners and low strain (whiter zones) around the center of the grips, which readily gives a qualitative

measurement of the effect of local property variation on mechanical properties.

Figure 5.6 shows a negative of the center of the scanned image of Figure 5.4 on the left and the effective von Mises strain field obtained through FLAC on the right. In this case, the simulation allowed sliding of the grips to avoid the concentration of strain in the corners. In the negative image, now the darker zones are low grammage areas that correlate well with darker zones of the strain field, which indicate high strained areas. The resulting effective strain field seems to be a mix of the formation image with the shear bands. This apparent spatial correlation can be quantified as follows: we have two series: $A(n)$ and $B(n)$, with $n = 48^2$ in this case, both taking values from 0 to 255. Both are of the same length N, which is equal to image size squared, $n \times n$; the *normalized cross-correlation* of $A(n)$ and $B(n)$ can be computed as:

$$\rho_{AB} = \frac{\frac{1}{N}\sum_{n=1}^{N} A(n)B(n) - [\frac{1}{N}\sum_{n=1}^{N} A(n)][\frac{1}{N}\sum_{n=1}^{N} B(n)]}{\sqrt{\{\frac{1}{N}\sum_{n=1}^{N} A^2(n) - [\frac{1}{N}\sum_{n=1}^{N} A(n)]^2\}\{\frac{1}{N}\sum_{n=1}^{N} B^2(n) - [\frac{1}{N}\sum_{n=1}^{N} B(n)]^2\}}} \tag{5.6}$$

A mathematical cross-correlation coefficient ρ_{AB} of 0.77 was obtained with this data as shown in the regression of Figure 5.7. This correlation allows confirming that the effective strain is localized in the regions of low basis weight as it was also observed by Wong et al. (1996) and Korteoja et al. (1998).

Figure 5.8 presents another example of cross-correlation between a negative image of formation and effective von Mises strain. In this case, the simulated paper sample is 180×180 mm. On the other hand, the finite element program allows simulation of fracture by removing grid elements as each one reaches certain failure criteria. Figure 5.9 shows two simulations of fracture using the von Mises strain as a failure criterion on the 180×180 element-paper sample of Figure 5.8. Other possible failure criteria that can be adopted to simulate fracture include von Mises stress, uniaxial stress, uniaxial strain, and energy. Each criterion produces a different fracture pattern, which can be correlated with the actual fracture line of the equivalent paper specimen. This aspect has not been fully studied yet and it is not included in the present Thesis.

5.2 Temperature fields during dynamic fracture of paper

We attempted to measure the heat dissipation in strained paper samples with the aim of establishing a correlation between formation and plastic deformation. The idea was to measure the change in temperature with an infrared (IR) camera on paper samples as they were strained up to fracture (see Yamauchi and Murakami, 1993). Then, from the temperature field the energy dissipation field could be found. In turns, heat dissipation is attributable to plastic deformation. However, it was not possible to measure such a change in temperature despite the use of the best magnification and spatial IR resolution available. As can be seen in Figures 5.10 and 5.11, heat

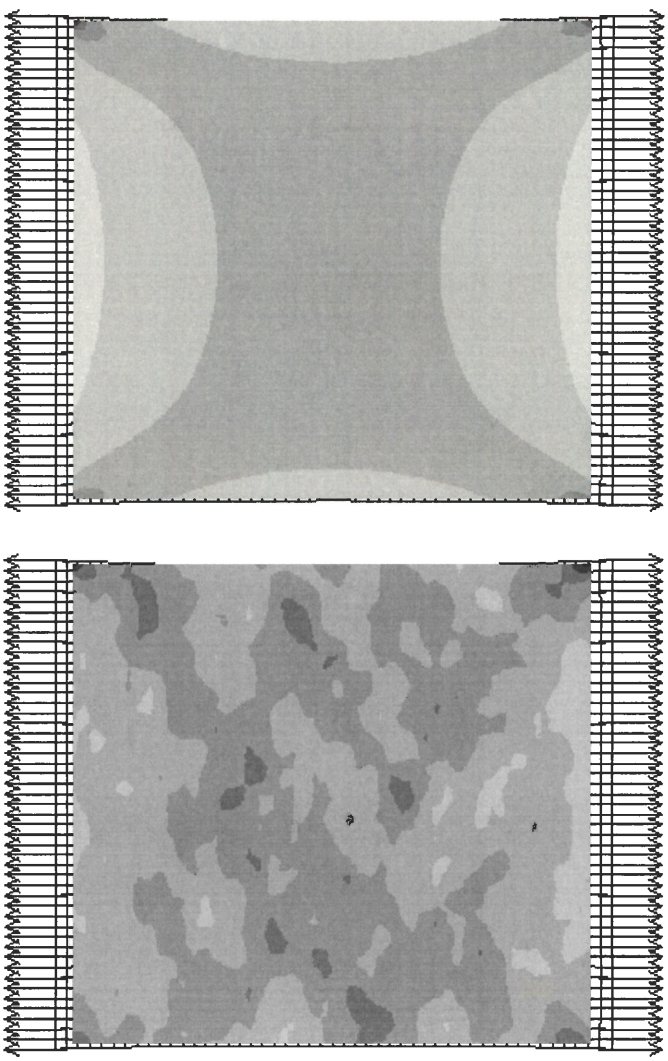
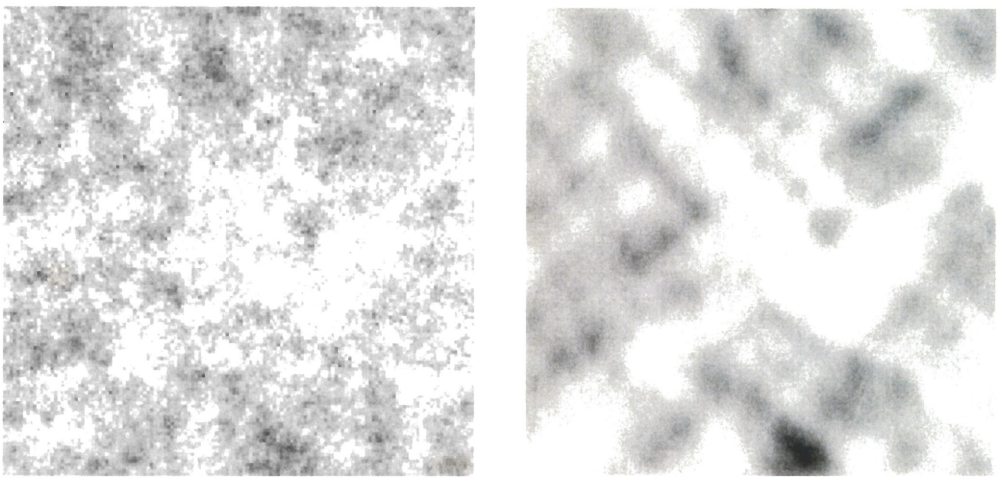


Figure 5.5: Effective von Mises strain in a homogeneous (top) and a nonhomogeneous (bottom) material. In the greyscale, clearest zones correspond to 0.8% and darkest zones to 2.2% strain. Applied strain is 1.05% in x (MD).



Negative image of formation

Effective strain field

Figure 5.6: Cross-correlation between formation and strain patterns (48 × 48 mm). On the right image, clearest zones correspond to 0.8% and darkest zones to 2.2% von Mises strain.

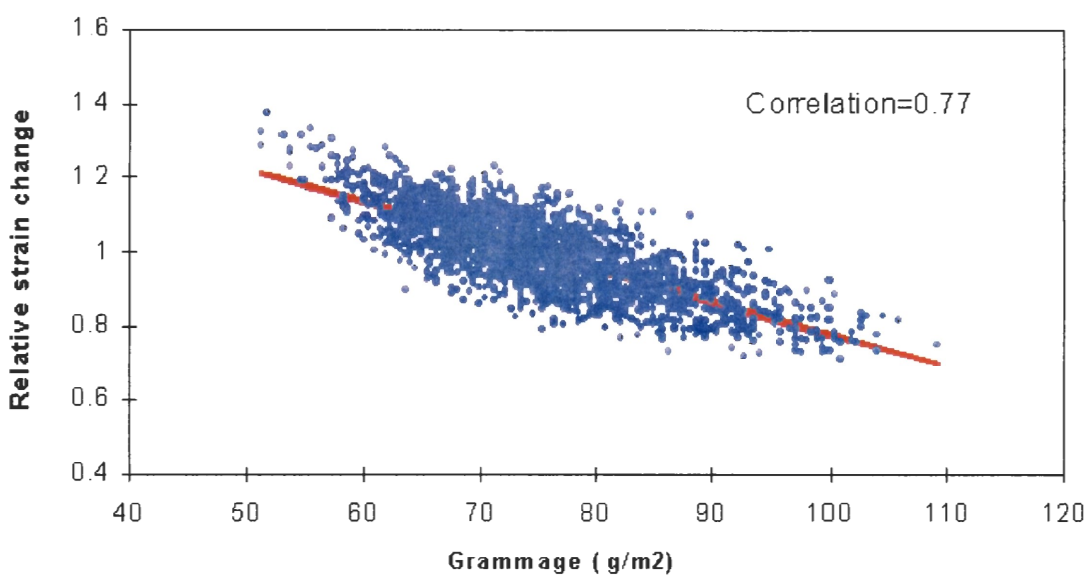


Figure 5.7: Simulated effective strain change against grammage

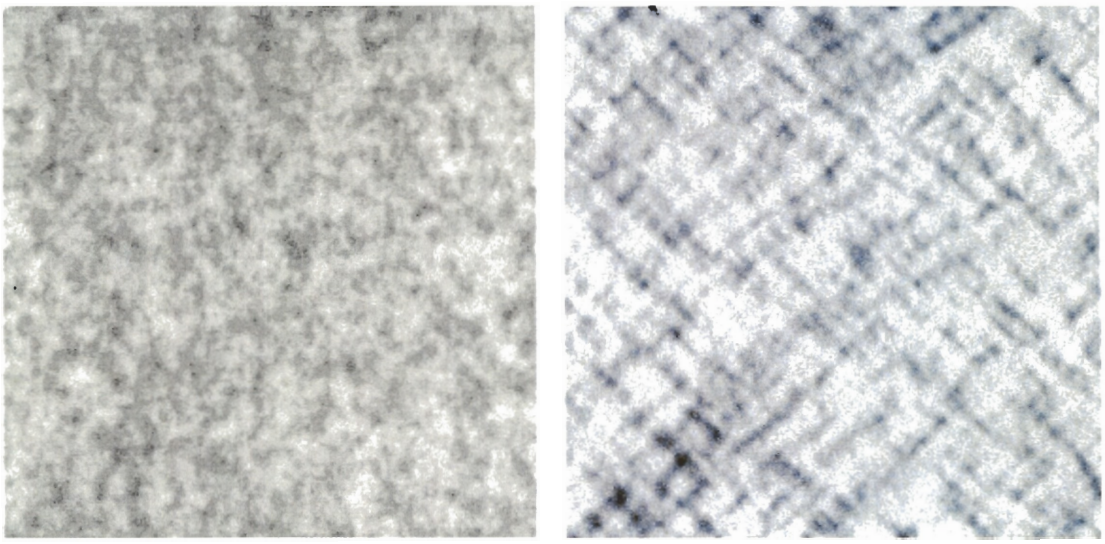


Figure 5.8: Cross-correlation between negative image of formation (left) and strain patterns (right). Sample size is 160 × 160 mm. On the right image, clearest zones correspond to 0.8% and darkest zones to 2.2% von Mises strain.

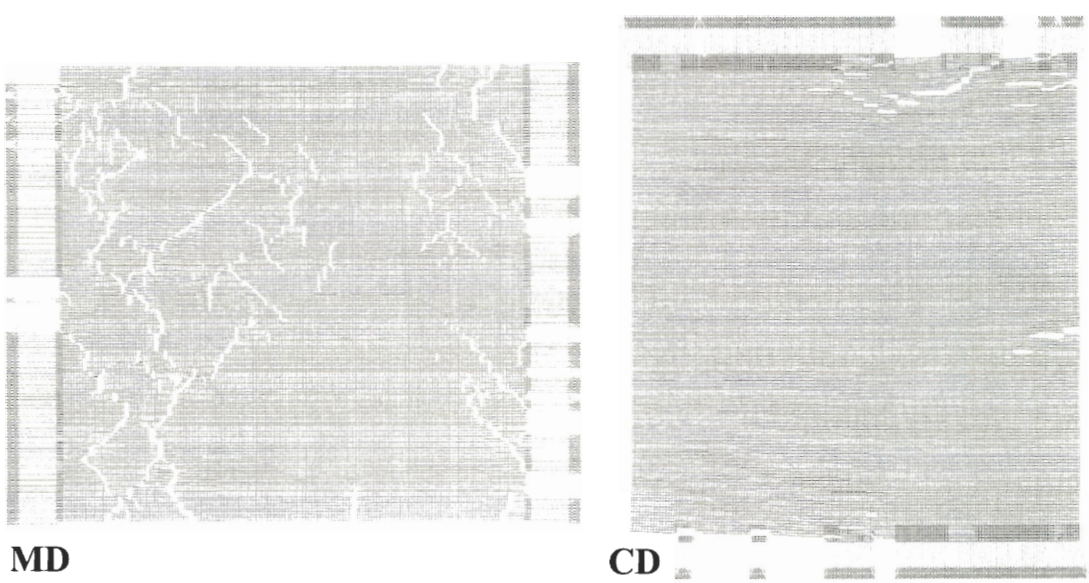


Figure 5.9: Simulated fracture of uniaxial strain tests in MD and CD. Failure criteria is based on von Mises strain.

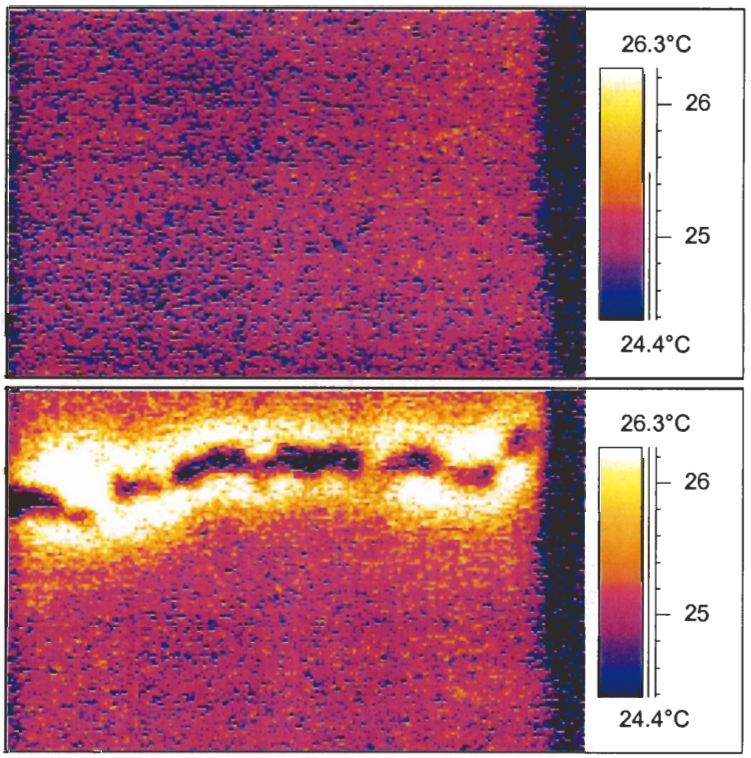


Figure 5.10: Infrared picture of dynamic fracture of paper. Sample is 25 mm wide.

dissipation (or temperature change) was detected only at the moment of fracture as a "flash" of light around a spontaneous crack line (these are 25-mm unnotched specimens). Therefore, there is no data to infer plastic deformation before yielding. Despite this drawback, these images can be used to establish two patterns of fracture, one in which the crack propagates at high speed, as in Figure 5.10, and another in which the crack propagates in steps, as in Figure 5.11.

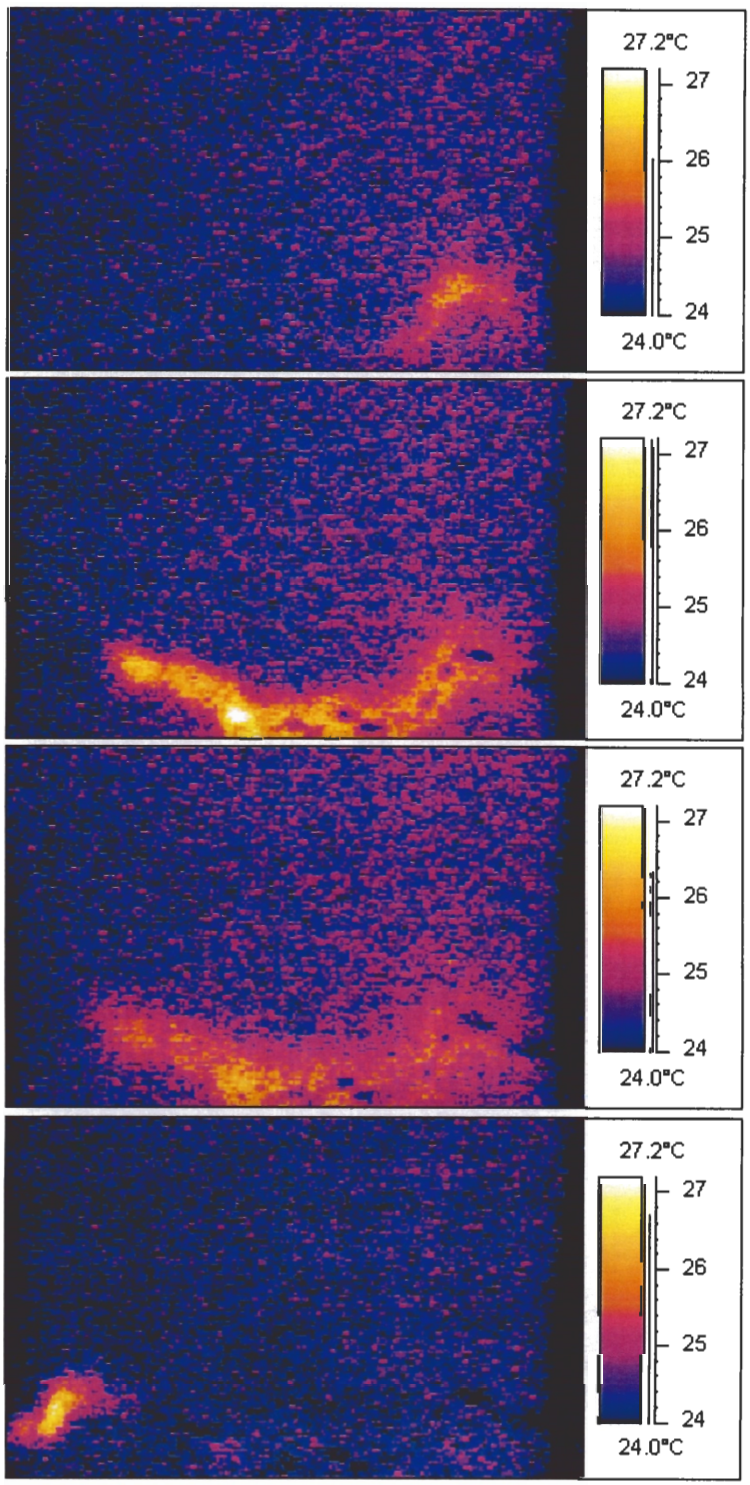


Figure 5.11: Infrared picture of dynamic crack propagation in paper. Sample is 25 mm wide.

Chapter 6

Closure

6.1 Conclusions and Significance

In this thesis we investigated the influence of random formation of paper on its mechanical in-plane response. This issue, however, required us to develop a constitutive model/equation of paper for biaxial tensile loading. Given the fact that paper is an elastic-inelastic material, we thus needed to first formulate an appropriate, thermodynamically consistent constitutive model, and then, on that basis, to study the effects of formation. The principal conclusions are:

1. A constitutive model of paper, for the biaxial tensile loading regime, treated as an elastic-inelastic material has been developed from the principles of continuum mechanics and thermodynamics. The particular framework chosen, thermomechanics with internal variables, allows the introduction of various linear and/or nonlinear, elastic and/or inelastic effects, all consistent with the fundamental laws of continuum physics. Given the complicated character of paper response, the resulting equations are quite complex. The present model was focused on elasto-plastic, rate-independent response, with due focus on the orthotropy of machine-made paper. However, depending on the application, the rate-dependence aspect can also be introduced within the same thermomechanics framework.

2. In order to study effect of formation on elasto-plasticity of paper, we investigated two-phase heterogeneous materials, locally of rigid-perfectly plastic type, having a random chessboard microgeometry. While offering a contribution to other materials (e.g., mild steels), this study was a stepping stone to paper mechanics. Our particular findings here included: The larger the mesoscale, the tighter are the bounds, albeit the kinematic condition displays a much stronger scale-dependence than the traction one; Neither in plane deformation rate nor in plane stress is the flow rule normal for any given realization of the random medium; In the case of plane deformation rate, the flow rule is normal upon ensemble averaging. This property is not recovered in the plane stress case; In the case of plane deformation rate the yield surface, for any given mesoscale and realization of the random medium, consists of two parallel lines. In the plane stress case, the yield surface is ellipse-shaped, albeit, for both boundary conditions (kinematic and traction), of a different aspect ratio than that of the HM

material.

3. By building on the results in the above two points, we studied mechanics of paper with explicit account taken of formation. This involved a randomization, in the material domain, of the elastic-hardening plastic law and computation of scale dependent bounds on effective (in the macroscopic sense) response. We found: The response strongly depends on the boundary conditions and window size (mesoscale); The larger the window size, the tighter are the bounds on the effective response.

4. Biaxial tensile tests were performed to obtain stress-strain curves for *white textured Crayola sketchpaper* up to failure. These curves allowed us to develop explicit function fits within and beyond the elastic regimes. To the best of our knowledge, these are first constitutive equations of paper consistent for both uniaxial and biaxial loading ranges. Failure surface, including its random scatter, was also mapped.

5. Combining the results in points 3 and 4 above, a study was performed of spatial cross-correlation between paper formation and von Mises strain fields in uniaxial loading. Very high values were found, thus confirming that this strain is localized in the regions of low basis weight. The same type of analysis may be conducted for the fracture patterns.

This type of theoretical work is applicable to optimize fiber use with respect to the desired mechanical properties, i.e., it can be used to determine up to what point it is advantageous to enhance formation and increase nominal basis weight.

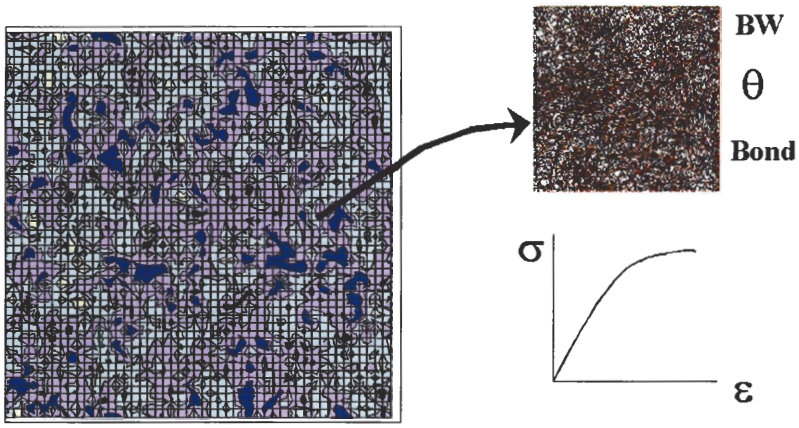


Figure 6.1: Obtaining mechanical properties from a fiber network model.

Future Work

Data from a fiber network model could be used as the input for the model proposed in this thesis. In other words, the response of every element of the continuum model could be computed using a fiber network model involving up to tens of thousands of fibers according to the local microstructure. Each finite element being assigned its properties, a global stiffness matrix could be assembled and global mechanical response studied: e. g., Oden and Zohdi (1997), Zohdi and Wriggers (1999), and Ostoja-Starzewski (1999). In such a multiscale model, not only the effect of formation, but also the effects of fiber orientation and bonding on global mechanical properties could be assessed. This idea is sketched in Figure 6.1.

Regarding thermal imaging, as the resolution of infrared cameras is enhanced in the future, it could be possible to infer plastic deformation fields and correlate them with formation.

List of symbols

α	Internal variable (plastic strain)
β	Internal stress
γ_{12}	Shear strain
γ	Lagrangian multiplier
δ	Mesoscale
ε	Strain
θ	Angle
λ	Constant
ν	Poisson's ratio
τ	Shear stress
ρ	Mass density
ρ_{AB}	Cross-correlation
ω	Subspace of Ω
σ	Stress
ψ,Ψ	Conjugate potential
ϕ, Φ	Conjugate potential
Ψ	Free energy
Φ	Dissipation function
Ω	Space of random variable
A	Constant
$\mathbf{A}$	Viscosity
B	Body
b	Constant
C	Stiffness
d	Floc diameter, grain size
d	Displacement
$\mathbf{d}$	Strain rate vector
E	Elastic modulus
f	General function
F	Force
F_r	Yield function
e	Effective strain
G	Shear modulus
$\mathbf{H}$	Hardening
$\mathbf{k}$	Proportional yield limit
m	Mass
M	Anisotropic tensor
$\mathbf{n}$	Unitary normal vector
P	Yield locus
Q	Orthotropic tensor
S	Compliance
t	Time
$\mathbf{t}$	Traction vector field

u	Velocity in 1-direction
$\mathbf{v}$	Velocity vector field
v	Velocity in 2-direction
V	Volume
w	Energy density function
$\mathbf{x}$	Coordinate vector (x, y, z)

References

Aström J. and Niskanen K. (1991), Simulation of network fracture, *TAPPI International Paper Physics Conference*, Book 1: 31-48 (Sept. 22-26, 1991).

Baum G.A., Habeger C.C., and Fleischman, E.H. (1983), Measurements of the orthotropic elastic constants of paper, *The Role of Fundamental Research in Paper Making. Transactions of the Symposium - Cambridge*, September 1981, Mechanical Engineering Publications Ltd., 453-478.

Baum G.A. (1993), Subfracture mechanical properties, in *Products of Papermaking - Transactions of the Tenth Fundamental Research Symposium - Oxford*, Baker, C. F., ed., Pira International, UK, 1-126.

Bažant Z.P. and Chen E. (1997), Scaling of structural failure, *Appl. Mech. Rev.* **50 (10)**, 593-627.

Bažant Z.P. and Planas J. (1998), *Fracture and Size Effect in Concrete and other Quasi-brittle Materials*, CRC Press.

Bouchitte G. and Suquet P.M. (1991), in *Composite Media and Homogenization Theory* (G. Dal Maso and G.F. Dell'Antonio, eds.), 107-133, Birkhäuser, Boston.

Bronkhorst C.R. and Bennett K.A. (2001), Deformation and failure behavior of paper, in *Handbook of Physical Testing of Paper*, Mark/Habeger, Vol 1, Chapter 7, 313-428.

Brugger K. (1964), Thermodynamic definition of higher order elastic coefficients, *Phys. Rev. A* **133**, 1611-1612.

de Buhan P. (1983), Homogénéisation en calcul à la rupture: le cas du matériaux composite multicouche, *C. R. Acad. Sci. Paris - II* **296**(11), 933-936.

Campbell J.G. (1961), The in-plane elastic constants of paper, *Austral J. Appl. Sci.* **12**, 356-357.

Carpintieri A., Chiaia B., and Ferro G. (1993), Multifractal nature of material microstructure and size effects on nominal tensile strength, *Fracture of Brittle Disordered Materials: Concrete, Rock and Ceramics*, First Edition: 21-34.

Castro J. and Ostoja-Starzewski M. (2000), Particle sieving by percolation through a random fiber network, *Appl. Math. Modelling* **24**, 523-534.

Choi D. and Thorpe J. (1991), Progressive deformation at the crack tip in paper during mode-I fracture - (1) Bond Paper, *TAPPI International Paper Physics Conference*, Book 1: 167-184 (Sept. 22-26, 1991).

Collins I.F. and Houlsby G.T. (1997), Application of thermomechanical principles to the modeling of geotechnical materials, *Proc. Roy. Soc. Lond. A* **453**, 1975-2001.

Cox H.L. (1952), The elasticity and strength of paper and other fibrous materials, *British J. Appl. Phys.* **3,** 72-79.

Cundall P.A. (1976), Explicit finite difference methods in geomechanics, *Numerical Methods in Engineering (Proceedings of the EF Conference on Numerical Methods in Geomechanics, Blacksburg, Virginia, 1976)* **1**, 132-150.

Deng M. and Dodson C.T.J. (1994), *Paper: An Engineered Stochastic Structure*, Tappi Press, Atlanta.

DiMillo M. and Ostoja-Starzewski M. (1998)., Paper strength: statistics and correlation structure, *Int. J. Fracture* **90**, L33-L38.

Dłużewski P. (2000), Anisotropic hyperelasticity based upon general strain measures, *J. Elasticity* **60**, 119-129.

Dodson C.T.J. (1970), The statistical analysis of pattern of deformation in flat bonded fibrous networks, *J. Phys. D: Appl. Phys.* **3**, 269-276.

Donner C.D. (1997), An heuristic model of paper, *The Fundamentals of Paper Making Materials*, Pira International, Vol. 2 (Baker, C. F., ed.), 1215-11247.

Farnood R.R., Yang N., Kortschot M.T., and Dodson C.T.J. (1997), Modelling flocculation: A gallery of simulated flocculated papers, *Nordic Pulp and Paper Research J.* **12** (2), 86-89.

Feldman H., Jayaraman K., and Kortschot M.T. (1996), Monte Carlo simulation of paper deformation and failure, *J. Pulp and Paper Sci.* **22** (10), J386-J392.

FLAC (1998), Theory and Background, Itasca Consulting Group, Inc., Minneapolis, MN 55415, USA.

Gates D.J. and Westcott M. (1996), Stochastic line model for paper stiffness, *Appita J.* **49** (3), 189-192.

Germain P., Nguyen Quoc Son, and Suquet P. (1983), Continuum thermodynamics, *ASME J. Appl. Mech.* **50**, 1010-1020.

Göttsching L. (1979), Influence of formation of paper on various strength properties, *Wochenblatt für Papierfabrikation* **107** (7), 228-235.

Gregersen O.W., Hansen A., and Helle T. (1998), Evaluation of newsprint strength and runnability by using Weibull statistics, *1998 Progress in Paper Physics*,Vancouver, Canada, p. D-1.

Hazanov S. and Huet C. (1994), Order relationships for boundary conditions effect in the heterogeneous bodies smaller than the representative volume, *J. Mech. Phys. Solids* **42**, 1995-2011.

Hazanov S. and Amieur M. (1995), On overall properties of elastic heterogeneous bodies smaller than the representative volume, *Int. J. Engng. Sci.* **23**, 1289-1301.

Hazanov S. (1998), Hill condition and overall properties of composites, *Arch. Appl. Mech.* **68**, 385-394.

Heyden S. and Gustafsson P. (1998), Simulation of fracture in a cellulose fiber network, *J. of Pulp and Paper Sci.* **24** (5), J160-J165.

Hill R. (1963), Elastic properties of reinforced solids: some theoretical principles, *J. Mech. Phys. Solids* **11**, 357-372.

Hill R. (1950), *The Mathematical Theory of Plasticity*, Clarendon Press, Oxford.

Houlsby G.T. and Puzrin A.M. (2000), A thermomechanical framework for constitutive models for rate-independent dissipative materials, *Int. J. Plast.* **16**, 1017-1047.

Huet C. (1982), Universal conditions for assimilation of a heterogeneous material to an effective medium, *Mech. Res. Comm.* **9**(3), 165-170.

Huet C. (1990), Application of variational concepts to size effects in elastic heterogeneous bodies, *J. Mech. Phys. Solids* **38**, 813-841.

Huet C. (1995), Bounds and hierarchies for the overall properties of viscoelastic heterogeneous and composite materials, *Arch. Mech.* **47**(6), 1125-1155.

Huet C. (1999a), Coupled size and boundary-condition effects in viscoelastic heterogeneous and composite bodies, *Mech. Mater.* **31**(12), 787-829.

Huet C. (1999b), Strength scaling law for elastic materials with interacting defects, in *Mechanics of Quasi-brittle Materials and Structures* (G. Pijaudier-Cabot, Z. Bittnar and B. Gérard, eds.), Hermes, Paris, 31-38.

Jayaraman and Kortschot M.T. (1998), Closed-form network models for the tensile strength of paper - a critical discussion, *Nordic Pulp and Paper Research J.* **13** (3), 233-242.

Jiang M., Ostoja-Starzewski M, and Jasiuk I. (2001), Scale-dependent bounds on effective elastoplastic response of random composites, *J. Mech. Phys. Solids* **49**(3), 655-673.

Johnson M.W. and Urbanik T.J. (1984), A nonlinear theory for plastic plates with application to characterizing paper properties, *J. Appl. Mech.* **51 (3)**, 146-152.

Kärenlampi P., Alava M.J., and Niskanen K.J. (1996), Stochastic analysis of paper toughness, *J. of Pulp and Paper Sci.* **22** (10), J392-J397.

Korteoja M.J., Lukkarinen A., and Niskanen K.J. (1995), Computational study of formation effects on paper strength, *International Paper Physics Conference* (CPPA and TAPPI): 137-141 (September 11, 1995).

Korteoja M.J., Lukkarinen A., Kaski K., Gunderson D., Dahlke J., and Niskanen K.J. (1996), Local strain fields in paper, *Tappi J.* **79** (4), 217-223.

Korteoja M.J., Lukkarinen A., Kaski K., and Niskanen K.J. (1997), Computational study of formation effects on paper strength, *J. Pulp and Paper Sci.* **23** (1), J18-J22.

Korteoja M.J., Salminen L., Niskanen K.J., and Alava M. (1998), Statistical variation of paper strength, *J. Pulp and Paper Sci.* **24** (1), J1-J7.

Korteoja M.J., Niskanen K.J., Kortschot M.T., and Kaski K.K. (1998), Progressive damage in paper, *Paperi Ja Puu - Paper and Timber* **80** (5), 364-372.

Lubliner J. (1990), *Plasticity Theory*, Macmillan Publ. Co., New York.

Maugin G.A. (1992), *The Thermomechanics of Plasticity and Fracture*, Cambridge University Press.

Maugin G.A. (1999), *The Thermomechanics of Nonlinear Irreversible Behaviors - an Introduction*, World Scientific, Singapore.

Mellor P.B. (1982), Experimental studies of plastic anisotropy in sheet metal, in *Mechanics of Solids - The Rodney Hill 60th Anniversary Volume* (H.G. Hopkins and M.J. Sewell, eds.), Pergamon Press, 383-415.

Niskanen K.J. (1993), Strength and fracture of paper, *Products of Papermaking*, Pira, Vol. 2 (Baker, C. F., ed.): p. 641-725 .

Niskanen K.J. (1998), *Paper Physics*, Paper Science and Technology, Book 16, PI/*TAPPI*.

Norman R.J. (1966), Dependence of sheet properties on formation and forming variables, in *Consolidation of the Paper Web - Cambridge* F. Bolam ed., London, Vol 1, 269-298.

Norman and Wahren (1976), Mass distribution and sheet properties of paper, The Fundamental Properties of Paper Related to Its Uses - *Transactions of the Fundamental Research Symposium 1973,* Cambridge, F. Bolam, ed., 7-73

Oden J.T. and Zohdi T. (1997), Analysis and adaptive modeling of highly heterogeneous elastic structures, *Comp. Meth. Appl. Mech. Eng.* **148**, 367-391.

Ostlund S. and Kerenlampi P. (1999), Scaling law for the strength of paper structures with a flaw, *Tappi International Paper Physics Conference*, 179-189.

Ostoja-Starzewski M. (1999), Microstructural disorder, mesoscale finite elements, and macroscopic response, *Proc. Roy. Soc. Lond. A* **455**, 3189-3199.

Ostoja-Starzewski M., Quadrelli M.B. and Stahl D.C. (1999), Kinematics and stress transfer in quasi-planar random fiber networks, *C.R. Acad. Sci. Paris IIb*, Vol. 327, 1223-1229.

Ostoja-Starzewski M. and Stahl D.C. (2001), Random fiber networks and special elastic orthotropy of paper, *J. Elasticity* **60**, 131-149.

Ostoja-Starzewski M. (2001), Mechanics of Random Materials: Stochastics, Scale Effects, and Computation, in *Mechanics of Random and Multiscale Microstructures* (D. Jeulin and M. Ostoja-Starzewski, eds.), CISM Courses and Lectures, Springer-Verlag, Wien, in press.

Ostoja-Starzewski M. (2002), Microstructural randomness versus representative volume element in thermomechanics, *ASME J. Appl. Mech.*, in press.

Perkins R.W., Richard M.E., and Thorpe T.L. (1990), Solids mechanics advances in paper related industries, *Proceedings of National Science Foundation Workshop held at the Minnowbrook Conference Center*, Syracuse University, August 13-15, 1986 / National Science Foundation Workshop Syracuse, NY: Syracuse University.

Ponte Castañeda P. and Suquet P.M. (1998), Nonlinear composites, *Adv. Appl. Mech.* **34**, 171-302.

Ponte Castañeda P. (2001), Nonlinearity and microstructure evolution in composite materials, *Proc. ICTAM 2000*, in press.

Räisänen V., Heyden S., Gustafsson P., Alava M. and Niskanen K. (1997), Simulation of the effect of a reinforcement fiber on network mechanics, *Nordic Pulp and Paper Research J.* **12** (3), 162-166.

Ramasusubramanian M.K. and Wang Y.Y. (1999), Constitutive models for paper and other ribbon-like nonwovens - a literature review, *Mechanics of Cellulosic Materials / ASME*, 31-42.

Sachs G. (1928), Zur Ableitung einer Fliessbedingung, *Z. Ver. Deutsch. Ing.* **72**, 734-736.

Seo Y.B., Castagnede B., and Mark R.E. (1992), An optimization approach for the determination of in-plane elastic constants of paper, *Tappi J.* **75** (11), 209-214.

Sewell M.J. (1988), *Maximum and Minimum Principles*, Cambridge University Press, Cambridge.

Suhling J.C., Johnson M.W., Rowlands R.E., and Gunderson D.E. (1989), Nonlinear elastic constitutive relations for cellulosic materials, *Mechanics of cellulosic and polymeric materials*: proceedings joint ASCE/ASME Mechanical conference, ASME, 1-15.

Suhling J.C. (1990), Continuum models for the Mechanical Response of paper and paper composites: past, present, and future, *Material Interactions Relevant to Pulp, Paper, and Wood Ind. Proceedings* **197**, 245-255.

Suquet P.M. (1986), Elements of homogenization for solid mechanics, in *Homogenization Techniques for Composite Media*, Lecture Notes in Physics **272**, (E. Sanchez-Palencia and A. Zaoui, eds.), 193-278, Springer-Verlag.

Suquet P.M. (1993), Overall potentials and extremal surfaces of power law or ideally plastic composites, *J. Mech. Phys. Solids* **41**(6), 981-1002.

Suquet P.M. (1997), Effective properties of nonlinear composites, in *Continuum Micromechanics*, CISM Courses and Lectures **377**, (P.M. Suquet, ed.), 197-264, Springer-Verlag.

Taylor G.I. (1938), Plastic strain in metals, *J. Inst. Met.* **62**, 307-324.

Uesaka T., Murakami K., and Imamura R. (1979), Biaxial tensile behavior of paper, *Tappi J.* **62** (8), 11-114.

Wellmar P., Fellers C., and Delhage L. (1997a), Fracture toughness of paper - development of a test method, *Nordic Pulp and Paper Research Journal* **12** (3), 189-195.

Wellmar P., Fellers C., and Delhage L. (1997b), Crack-tip characterization in paper, *J. Pulp and Paper Sci.* **23 (6)**, J269-J276 .

Wentao L., Carlsson, L.A., and Andersson Y. (1995), Micro-model of paper, Part 1: Bounds on elastic properties, *Tappi J.* **78** (12), 155-164.

Wentao L. and Carlsson, L.A. (1996), Micro-model of paper, Part 2: Statistical analysis of paper structure, *Tappi J.* **79** (1), 203-210.

Wentao L. and Carlsson, L.A., and de Ruvo A. (1996), Micro-model of paper, Part 3: Mosaic model, *Tappi J.* **79** (2), 203-210.

Willis J.R. (1981), Variational and related methods for the overall properties of composites, *Adv. Appl. Mech.* **21**, 1-78.

Wong L., Kortschot M.T., and Dodson C.T.J. (1995), Finite element analysis and experimental measurement of strain fields and failure in paper, *International Paper Physics Conference* (CPPA and TAPPI): 131-135 (September 11, 1995).

Wong L., Kortschot M.T., and Dodson C.T.J. (1996), Effect of formation on local strain fields and fracture of paper, *J. Pulp and Paper Sci.* **22 (6)**, J213-J219.

Yamauchi T. and Murakami K. (1993), Observation of deforming and fracturing processes of paper by use of thermography, in *Products of Papermaking - Transactions of the Tenth Fundamental Research Symposium - Oxford*, Baker, C.F., ed., Pira International, UK, 825-847.

Ziegler H. (1983), *An Introduction to Thermomechanics*, North-Holland.

Ziegler H. and Wehrli C. (1987), The derivation of constitutive relations from the free energy and the dissipation functions, *Adv. Appl. Mech.* **25**, 183-238, Academic Press, New York.

Ziman J.M. (1979), *Models of Disorder*, Cambridge University Press.

Zohdi T. and Wriggers P. (1999), A domain decomposition method for bodies with heterogeneous microstructure based on material regularization, *Int. J. Solids Struct.* **36**, 2507-2525.